Dissertation

submitted to the
Combined Faculties of the Natural Sciences and Mathematics
of the Ruperto-Carola-University of Heidelberg, Germany
for the degree of
Doctor of Natural Sciences

Put forward by
Dipl.-Phys. Kristina Meyer
born in Heppenheim an der Bergstraße

Oral examination: November 12th, 2014

Coherent and statistical phase control and measurements of time-dependent quantum dynamics

Referees: **Dr. Thomas Pfeifer**
Prof. Dr. Andreas Wolf

Kohärente und statistische Phasenkontrolle und Messungen zeitabhängiger Quantendynamik — Diese Arbeit befasst sich mit der Rolle der Phase in der zeitaufgelösten Spektroskopie in zweierlei Hinsicht. Zum einen werden die Auswirkungen der Phase der Dipolantwort eines Systems nach dessen Anregung untersucht. Frühere transiente Absorptionsmessungen an Helium ermöglichten es, die Phase des abstrahlenden Dipols mit Hilfe eines zweiten koppelnden Laserpulses zu messen und zu kontrollieren. Das entwickelte Konzept wird nun auf ein komplexeres System verallgemeinert, nämlich ein Farbstoffmolekül in der Flüssigphase. Dazu wurde ein Versuchsaufbau für die transiente Absorptionsspektroskopie mit Femtosekunden-Infrarot-Laserpulsen entwickelt und aufgebaut und numerische Simulationen helfen bei der Interpretation der experimentellen Ergebnisse. Hierbei konnte gezeigt werden, dass nur bestimmte angeregte Zustände stark an das Laserfeld koppeln. Während die vorangegangenen Experimente auf der vollständigen Kohärenz der Laserpulse basieren, werden hier im zweiten Teil der Arbeit die Auswirkungen von nur teilweise kohärenten Phasen der Laserpulse betrachtet. Pump–Probe-Messungen an Deuteriummolekülen in der Gasphase, die statistisch variierende Pulse einer Freie-Elektronen-Laserquelle verwendeten, zeigten, dass eine erhöhte zeitliche Auflösung erreicht werden kann, die kürzer als die mittlere Pulsdauer ist. Zur Beschreibung und Erklärung der Beobachtungen wird ein neuer Ansatz entwickelt, der auf der Korrelation von zeitlichen zufälligen Substrukturen der Pulse basiert. Um solch verrauschte Laserpulse auch im Labor zu generieren, wird ein Pulsformer aufgebaut, mit Hilfe dessen die spektrale Phase der Pulse moduliert werden kann. Diese entwickelte allgemeine Methode wird damit auf transiente Absorptionsmessungen in der Flüssigphase übertragen und ihre allgemeine Anwendbarkeit gezeigt.

Coherent and statistical phase control and measurements of time-dependent quantum dynamics — In this work the importance of phases in time-resolved spectroscopy is investigated in two respects. At first, the influence of the phase of a system's dipole response after excitation is studied. Previous transient-absorption experiments in helium allowed the measurement and control of this phase of an emitting dipole by a second, coupling laser pulse. The derived concept is now generalized to a more complex system, i.e. a dye molecule in the liquid phase. For this purpose, a setup for transient-absorption measurements with femtosecond infrared laser pulses is developed and assembled and numerical simulations support the interpretation of the experimental results. It was found that only specific excited states couple strongly to the laser field. While the foregoing experiments rely on the full coherence of laser pulses, the second part of this work addresses the impact of partially coherent phases of laser pulses. Pump–probe experiments in gaseous deuterium molecules applied statistically fluctuating pulses delivered by a Free-Electron Laser source. These measurements revealed an enhanced temporal resolution on time scales shorter than the average pulse duration. For the description and explanation of the observations a novel approach is developed which is based on the correlation of temporally random substructures of the pulses. In order to realize noisy pulses in the laboratory, a pulse shaper is designed and built up which is capable to modify the spectral phase of the laser pulses. Thereby, this developed general method is transferred to transient-absorption measurements in the liquid phase and its universal applicability is demonstrated.

List of Publications

Parts of this work have been published or prepared in the following references:

K. Meyer, C. Ott, P. Raith, A. Kaldun, Y. Jiang, A. Senftleben, M. Kurka, R. Moshammer, J. Ullrich, and T. Pfeifer.
Noisy Optical Pulses Enhance the Temporal Resolution of Pump–Probe Spectroscopy.
Phys. Rev. Lett. **108**, 098302 (2012).
(for additional information see [1])

Y. Zhang, K. Meyer, C. Ott, and T. Pfeifer.
Passively phase-stable, monolithic, all-reflective two-dimensional electronic spectroscopy based on a four-quadrant mirror.
Opt. Lett. **38**, 356–358 (2013).
(for additional information see [2])

C. Ott, A. Kaldun, P. Raith, K. Meyer, M. Laux, J. Evers, C. H. Keitel, C. H. Greene, and T. Pfeifer.
Lorentz Meets Fano in Spectral Line Shapes: A Universal Phase and Its Laser Control.
Science **340**, 716–720 (2013).
(for additional information see [3])

C. Ott, A. Kaldun, L. Argenti, P. Raith, K. Meyer, M. Laux, Y. Zhang, A. Blättermann, S. Hagstotz, T. Ding, R. Heck, J. Madrõnero, F. Martin and T. Pfeifer.
Time-dependent two-electron wave-packet observation and control.
submitted (2014).
(for additional information see earlier version [4])

Further publications with own contributions:

K. Schnorr, A. Senftleben, G. Schmid, A. Rudenko, M. Kurka, K. Meyer, L. Foucar, M. Kübel, M. F. Kling, Y. H. Jiang, S. Düsterer, R. Treusch, C. D. Schröter, J. Ullrich, T. Pfeifer, and R. Moshammer.
Multiple ionization and fragmentation dynamics of molecular Iodine studied in IR-XUV pump-probe experiments.
submitted to Farad. Discuss. (2014).
(for additional information see [5])

K. Schnorr, A. Senftleben, M. Kurka, A. Rudenko, G. Schmid, T. Pfeifer, K. Meyer, M. Kübel, M. F. Kling, Y. H. Jiang, R. Treusch, S. Düsterer, B. Siemer, M. Wöstmann, H. Zacharias, R. Mitzner, T. J. M. Zouros, J. Ullrich, C. D. Schröter, and R. Moshammer.
Electron Rearrangement Dynamics in Dissociating I_2^{n+} Molecules Accessed by Extreme Ultraviolet Pump-Probe Experiments.
Phys. Rev. Lett. **113**, 073001 (2014).
(for additional information see [6])

A. Kaldun, C. Ott, A. Blättermann, M. Laux, K. Meyer, T. Ding, A. Fischer, and T. Pfeifer.
Extracting Phase and Amplitude Modifications of Laser-Coupled Fano Resonances.
Phys. Rev. Lett. **112**, 103001 (2014).
(for additional information see [7])

Y. Mi, A. Kaldun, K. Meyer, and T. Pfeifer.
Time-domain pulse compression by interfering time-delay operations.
Phys. Rev. A **88**, 053824 (2013).
(for additional information see [8])

P. Raith, C. Ott, K. Meyer, A. Kaldun, M. Laux, M. Ceci, C. P. Anderson, and T. Pfeifer.
Carrier-envelope phase-and spectral control of fractional high-harmonic combs.
J. Appl. Phys. **114**, 173102 (2013).
(for additional information see [9])

K. Schnorr, A. Senftleben, M. Kurka, A. Rudenko, L. Foucar, G. Schmid, A. Broska, T. Pfeifer, K. Meyer, D. Anielski, R. Boll, D. Rolles, M. Kuebel, M. F. Kling, Y. H. Jiang, S. Mondal, T. Tachibana, K Ueda, T. Marchenko, M. Simon, G. Brenner, R. Treusch, S. Scheit, V. Averbukh, J. Ullrich, C. D. Schröter, and R. Moshammer.
Time-Resolved Measurement of Interatomic Coulombic Decay in Ne_2.
Phys. Rev. Lett. **111**, 093402 (2013).
(for additional information see [10])

C. Ott, M. Schönwald, P. Raith, A. Kaldun, G. Sansone, M. Krüger, P. Hommelhoff, Y. Patil, Y. Zhang, K. Meyer, M. Laux, and T. Pfeifer.
Strong-field spectral interferometry using the carrier-envelope phase.
New J. Phys. **15**, 073031 (2013).
(for additional information see [11])

P. Raith, C. Ott, C. P. Anderson, A. Kaldun, K. Meyer, M. Laux, Y. Zhang, and T. Pfeifer.
Fractional high-order harmonic combs and energy tuning by attosecond-precision split-spectrum pulse control.
Appl. Phys. Lett. **100**, 121104 (2012).
(for additional information see [12])

Contents

Chapter 1

Introduction

What is a 'phase'? Asking this question to first-year physics students the answer will most likely be (provided that we do not ask about states of matter): "No idea." Phases are part of everyday life, but somehow we do not have an intuitive picture or idea of what it is. It is not an obvious phenomenon, it is not directly tangible. But the phase is an important ingredient in electronics and optics for example.

The phase is a characteristic quantity for the description of an oscillation or wave. Following the definition the phase ϕ specifies the position of the periodic evolution or, in other words, in which section of one period the wave is. From mathematics, the sine function is known. At zero, the sine function equals to zero. It reaches its maximum for a phase value of $\pi/2$, becomes zero again at π and passes its minimum at $3\pi/2$ before it reaches the initial value of zero at 2π. If the sine function is shifted by a phase of $\pi/2$, the cosine function is obtained, i.e. $\sin(x + \pi/2) = \cos(x)$. One can also say that sine and cosine are out of phase by $\pi/2$ or 90°, respectively. In general, there is a complex representation of oscillations or waves given by an amplitude A and the phase ϕ which both might be time- and/or space-dependent: $A \cdot \exp(i\phi)$. The real and imaginary part are then given by the cosine and sine, respectively.
An illustrative example for different phases of oscillations are two identical coupled pendulums. There are two eigenmodes which differ in the phases of the oscillations of each single pendulum. In the first eigenmode, the two pendulums swing parallel. Thus, the phase between the oscillations of pendulum 1 and pendulum 2 is $\phi = 0$. In the second eigenmode, the two pendulums swing against each other corresponding to a relative phase of π. For any other phase, energy is transferred from one pendulum to the other and back so that a complex overall oscillation occurs.
Another well-known example pointing out the role played by the phase is the interference of waves, e.g. water waves or sound waves. If two waves of the same amplitude and frequency are in phase, i.e. $\phi = 0$ (or a multiple of 2π), they interfere constructively. This means that the water wave is twice as high or that the volume is increased in case of sound waves. Destructive interference occurs for $\phi = \pi$ (or an odd multiple of it) and the two waves annihilate. For the considered examples, this corresponds to a smooth water surface or that no sound is audible.

The type of waves we are dealing with in the experiments described in this thesis work are

light waves – to be more specifically: coherent light waves as they are provided by lasers. In contrast to the light emitted by electric bulbs or similar where each phase train has a random phase, i.e. the light is incoherent, the crucial property characterizing laser light is its coherence. The light waves exhibit fixed phase relations, for example in space, time, momentum and/or frequency. In case of pulsed sources, for instance, the light waves of different frequencies, but with a defined relative spectral phase interfere leading to the formation of laser pulses.
The coherence of laser light enabled the development and achievement of various techniques in atomic and molecular physics in the last decades which can be regarded as milestones. For instance, the way was paved for the field of ultracold atoms and molecules by the realization of laser cooling [13] and trapping [14] atoms, finally enabling the production of Bose-Einstein condensates [15, 16]. Coherent laser pulses also allowed the implementation of high-resolution spectroscopy [17] or the probing of quantum dynamics on ultrashort time scales reaching the attosecond regime [18]. Ultrashort coherent laser pulses even stimulated the investigation of quantum effects in photosynthesis, for example by two-dimensional spectroscopy [19] revealing an energy transfer based on quantum coherence [20]. However, a controversial discussion was sparked in consideration of the fact that in natural environment the sunlight is incoherent.

This thesis addresses the question about the role of the phase in time-resolved quantum dynamics in two different aspects. First of all, fully coherent laser pulses serve as a tool to investigate and control the phase of a system's response in time-resolved pump–probe experiments. There, a close look is taken at the absorption process by investigating the formation of absorption lines and their modifications. However, the attention is also turned to the phase of the laser pulses itself. The full coherence is destroyed on purpose by imprinting noise on the spectral phase and the implications for time-resolved spectroscopy are studied.

Pump–probe experiments in gaseous helium recently performed by our group apply attosecond pulse trains and visible/infrared laser pulses to study the dynamical process of absorption. Thereby, modifications of the asymmetric Fano absorption line shapes of the doubly excited states in helium could be observed. Fano line shapes occur if discrete excited states couple to a continuum [21, 22]. These asymmetric line profiles are known not only in atomic physics [23–25], but also in solid-state [26–29] and nuclear physics [30] and even in molecular spectroscopy in chemistry [31]. In our transient-absorption experiments, we found out that the Fano line shapes could be modified and even changed into symmetric Lorentzian profiles by varying the intensity of the coupling visible/infrared femtosecond laser pulse [3, 4]. An analogous scenario was observed in case of the singly excited states where originally symmetric Lorentzian absorption profiles could be converted into Fano lines. For understanding the observations a model in the time domain was developed which relates the line shape changes to a laser-induced phase shift of the atoms' dipole response. Moreover, the new formalism allows the mapping of the induced phase to the asymmetry of the absorption lines and vice versa.
In this thesis, the discovered control of the system's dipole response via the intensity of the coupling pulse and the derived Fano-phase formalism are transferred to a more complex system in the liquid phase in order to test its universality. Transient-absorption measurements with femtosecond pulses are carried out in analogy to the helium experiment. As

target system the large dye molecule IR144 in a solution of methanol is chosen. In the measurements, the absorption spectrum is dominated by a broad absorption profile, but also there, changes in the shape of the absorption peak with increasing coupling-pulse intensity appear. With the help of a toy model based on the previously developed Fano concept, these changes can be directly explained by freely decaying dipole oscillations that experience a phase shift induced by the coupling pulse, thus, leading to a variation of the absorption line shape.

Having investigated the control of a system's inherent phase with fully coherent pulses, the second part of this thesis directly focuses on the spectral phase of laser pulses, its control and the arising implications. However, we do not consider specifically designed spectral phases like sinusoidal, quadratic or higher order phase functions, but our interest is focused on noise. Intuitively, noise seems to destroy any coherence and no benefit can be derived. However, there are several strong hints pointing out positive effects of noise. A clear sign for the benefits of noise is stochastic resonance [32] which could be observed in electronics or biology for example. An enhanced ionization of atoms in noisy laser fields was predicted by Singh et al. [33] and the effect on nonresonant autocorrelation measurements was observed [34]. Furthermore, it was reported that the spectral resolution could be increased in two-photon absorption [35] and linear [36] and nonlinear [37–39] coherent Raman scattering.
Partially coherent pulses in the X-ray wavelength range with statistically fluctuating shapes are provided by Free-Electron Laser sources. Pump–probe measurements investigating the wave-packet dynamics in deuterium molecules [40] revealed positive effects of such noisy pulses on the temporal resolution. We take a closer look at these measurements and derive a physical mechanism to explain the observed temporal resolution on a time scale shorter than the average pulse duration. As it is desirable to exploit the advantages of noisy pulses not only in the X-ray, but also in other wavelength ranges and to generate these pulses in the own laboratory, we demonstrate the realization of partially coherent pulses in table-top experiments using an optical femtosecond pulse shaper. The application of these pulses to different pump–probe scenarios in more complex systems – in our case transient-absorption measurements in the liquid phase are chosen again – shall prove the generality of the discovered formalism.

The transfer of the found concepts to complex systems is thereby motivated by possible future applications like studying the processes in photosynthesis with noisy pulses to mimic better the natural conditions or developing a new kind of precision spectroscopy based on line-shape analysis.

This thesis is structured as follows: In chapter 2, the theoretical concepts are introduced on which the content of this thesis is based. The fundamental principles of laser pulses and their temporal and spectral phases are discussed and the autocorrelation method, the second-harmonic generation process and the basics of absorption are explained. At the end, a short description of wave-packet dynamics is given. Chapter 3 provides details about the experimental setup. In the beginning, the laser sources and detection methods relevant for the experiments discussed in this thesis are described. Then, the experimental setups for the transient-absorption measurements and the pulse shaper that were designed and built up from scratch are presented in detail. In chapter 4, the absorption process in small and complex systems is discussed. The time-resolved transient-absorption measure-

ments in gaseous helium are explained and the Fano-phase model is introduced assigning the observed line-shape modifications to an additionally laser-induced phase that is imprinted on the system's dipole response. The discovered phase-control concept is transferred to a more complex system in the liquid phase, i.e. a solution of the dye molecule IR144 in methanol, and its general applicability is proven. In chapter 5, emphasis is placed on the properties of partially coherent laser pulses. Firstly, the beneficial effects concerning the temporal resolution in gas-phase pump–probe experiments are discussed. Secondly, the generation of statistically fluctuating laser pulses in our laboratory is shown for the example of autocorrelation measurements. Thirdly, the noisy pulses are applied to transient-absorption experiments in the liquid phase demonstrating the universality of the beneficial properties. Finally, the experimental results are summarized in chapter 6 and an outlook is given.

Chapter 2

Theoretical background

In this chapter some fundamental concepts of lasers, optics and quantum dynamics necessary for the comprehension of this thesis are introduced and summarized. First of all, the mathematical description of laser pulses and their characterization is presented. Then, some basics of nonlinear optics are explained. At the end, the principles of absorption and quantum wave packets are discussed. The following sections refer to standard textbooks [41–46] and more details can be found therein.

2.1 The basics of laser pulses

The tools for studying the electron dynamics in atoms and molecules are ultrashort laser pulses. In the experiments presented in this thesis the pulse durations are on the order of femtoseconds (10^{-15} s). The durations of laser pulses usually used by the different spectroscopy techniques can cover the range from nanoseconds (10^{-9} s) down to attoseconds (10^{-18} s). Furthermore, the spectral region of laser pulses can vary from the infrared to the X-ray. The laser pulses are electromagnetic wave packets and fully described by the time- (and space-) dependent electric field.

In general, the electric field of a (linearly polarized) laser pulse in the time domain is given by

$$\widetilde{E}_{\text{laser}}(t) = \widetilde{E}_0(t) \cdot e^{i\phi(t)} \tag{2.1}$$

with the temporal phase $\phi(t)$ and the complex envelope $\widetilde{E}_0(t)$. The measurable electric field is the real part of equation (2.1) given by

$$E(t) = \text{Re}\left\{\widetilde{E}_{\text{laser}}(t)\right\} = E_0(t) \cdot \cos(\phi(t)). \tag{2.2}$$

The envelope function contains the information about the temporal shape of the pulse. The quantity measured in experiments (provided that the detector has a sufficient electronic bandwidth) is the intensity $I(t) = \left|\widetilde{E}_{\text{laser}}(t)\right|^2$, usually given in units of W/cm^2.

In many experiments the temporal duration and the spectrum of the laser pulses are the characteristics that can be determined. Knowing the spectral distribution, laser pulses can

also be defined in the frequency domain by

$$E_{\mathrm{s}}(\omega) = A(\omega) \cdot e^{i\varphi(\omega)}, \tag{2.3}$$

where $A(\omega)$ is the spectral amplitude and $\varphi(\omega)$ the spectral phase. Experimentally accessible (e.g. by means of a spectrometer) is the spectral intensity $\widetilde{I}(\omega) \propto \left|\widetilde{E}(\omega)\right|^2 = |A(\omega)|^2$.

The representations of laser pulses in the time and frequency domain are connected through Fourier transforms. If the spectral field is given, the Fourier transform yields the temporal electric field and vice versa:

$$E_{\mathrm{s}}(\omega) = \mathscr{F}\left\{\widetilde{E}_{\mathrm{laser}}(t)\right\} = \frac{1}{\sqrt{2\pi}} \int_{-\infty}^{\infty} dt\, \widetilde{E}_{\mathrm{laser}}(t)\, e^{-i\omega t} \tag{2.4}$$

$$\widetilde{E}_{\mathrm{laser}}(t) = \mathscr{F}^{-1}\left\{E_{\mathrm{s}}(\omega)\right\} = \frac{1}{\sqrt{2\pi}} \int_{-\infty}^{\infty} d\omega\, E_{\mathrm{s}}(\omega)\, e^{i\omega t} \tag{2.5}$$

In the temporal and spectral domain the laser pulses are typically characterized by their widths, namely the pulse duration $t_{\mathrm{pulse}} = \Delta t_{\mathrm{FWHM}}$ and the bandwidth $\Delta\omega_{\mathrm{pulse}} = \Delta\omega_{\mathrm{FWHM}}$. These two parameters are the full width at half maximum (FWHM) of the intensity $I(t)$ and spectral intensity $\widetilde{I}(\omega)$, respectively, as indicated by the subscript "FWHM". As the temporal and spectral features are linked via the Fourier transform, t_{pulse} and $\Delta\omega_{\mathrm{pulse}}$ have to fulfill the relation

$$t_{\mathrm{pulse}} \cdot \Delta\omega_{\mathrm{pulse}} \geq 2\pi\, c_{\mathrm{B}}, \tag{2.6}$$

corresponding to the uncertainty principle. The constant c_{B} depends on the pulse shape [42].

For the mathematical description of ultrashort laser pulses, the choice of a Gaussian temporal profile is standard:

$$E_{\mathrm{G}}(t) = E_0(t) \cdot e^{-t^2/t_{\mathrm{G}}^2}. \tag{2.7}$$

Other envelopes that approximate experimental pulses very well are a hyperbolic secant or a cosine squared function. For the Gaussian profile the FWHM pulse duration t_{pulse} is related to the parameter t_{G} by

$$t_{\mathrm{pulse}} = \sqrt{2\ln 2} \cdot t_{\mathrm{G}} \approx 1.177 \cdot t_{\mathrm{G}}. \tag{2.8}$$

The Fourier transform (cf. equation (2.4)) of a Gaussian function is again a Gaussian so that for the spectral distribution

$$\widetilde{E}_{\mathrm{G}}(\omega) \propto e^{-(t_{\mathrm{G}}\omega)^2/2} \tag{2.9}$$

is obtained. In analogy to the time domain, the FWHM spectral width is given by

$$\Delta\omega_{\mathrm{pulse}} = 2\sqrt{2\ln 2}/t_{\mathrm{G}} \approx 2.355/t_{\mathrm{G}}. \tag{2.10}$$

Recalling the relation defined in equation (2.6), the constant amounts to $c_{\mathrm{B}} = 2\ln 2/\pi \approx 0.411$ for this case of a Gaussian pulse.

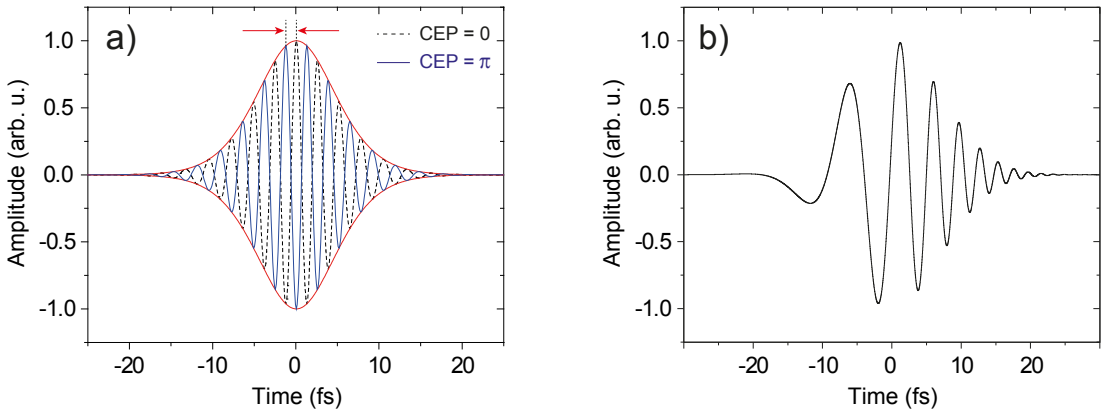

Figure 2.1: Carrier-envelope phase offset and temporal chirp. (a) The pulse envelope (red solid line) and the electric field for a phase $\phi_0 = 0$ (black dashed line) and $\phi_0 = \pi$ (blue solid line). The shift of the carrier field versus the envelope is marked by red arrows. (b) Electric field of an up-chirped pulse, i.e. the instantaneous frequency increases with time.

Equation (2.6) also states that there is a minimum limit of the pulse duration t_{pulse} for a given bandwidth $\Delta\omega_{\text{pulse}}$. This limit is called "Fourier limit" or "bandwidth limit", which means the shortest possible pulse for a given bandwidth is obtained.

Laser pulses are bandwidth-limited if their time- and frequency-dependent phase, $\phi(t)$ and $\varphi(\omega)$, are zero or flat, respectively. However, due to the generation process of the laser pulses and/or the propagation through and reflection off dispersive optics the pulse durations can be much larger than the possible bandwidth limit. In order to unravel the impact on the pulses, a look is taken separately at the two different phases.
The time-dependent phase can be Taylor expanded into

$$\phi(t) = \phi_0 + \frac{\partial\phi}{\partial t}\,t + \widetilde{\varphi}(t), \tag{2.11}$$

where $\widetilde{\varphi}(t)$ contains higher orders $\mathcal{O}(t^n)$. A constant phase $\phi(t) = \phi_0$ is the so-called carrier envelope phase (CEP) which describes the offset between the envelope $E_0(t)$ and the oscillating electric field. The impact of the CEP is depicted in Fig. 2.1(a). The derivative of the temporal phase is known as the instantaneous frequency

$$\omega(t) = \frac{d\phi(t)}{dt} = \frac{\partial\phi}{\partial t} + \frac{d\widetilde{\varphi}(t)}{dt} = \omega_0 + \frac{d\widetilde{\varphi}(t)}{dt} \tag{2.12}$$

with the constant ω_0 as the central frequency which is the mean value of the laser pulse spectrum. For $d\widetilde{\varphi}(t)/dt \neq 0$ the instantaneous frequency changes with time. If $\omega(t)$ increases with time, the pulses are called up-chirped and if it decreases, they are termed down-chirped. The case of an up-chirped pulse is shown in Fig. 2.1(b).

When light passes through a medium, its frequency components propagate with different velocities. Hence, different spectral phases are picked up. This phenomenon is called dispersion and has a significant impact on the pulse properties. To have a closer look at the different contributions of the spectral phase, $\varphi(\omega)$ is also expanded into a Taylor series [41]:

$$\varphi(\omega) = \sum_{n=0}^{\infty} \frac{1}{n!}\,\frac{\partial^n\varphi}{\partial\omega^n}\bigg|_{\omega_0} (\omega-\omega_0)^n \tag{2.13}$$

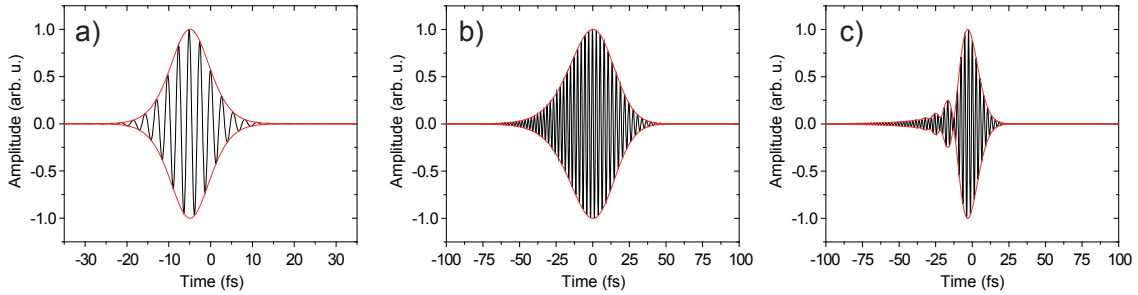

Figure 2.2: Impact of the different spectral phase components on the shape of a ~ 7.6 fs short pulse, centered at a wavelength of 780 nm. (a) A group delay of $\tau_g = 5$ fs shifts the pulse by 5 fs in time. (b) Pulse shape for a group-delay dispersion of GDD $= 35$ fs^2 (linear chirp). The pulse duration is significantly increased. (c) A third-order dispersion TOD $= 40$ fs^3 deforms the pulse shape. The pulse is split up into several subpulses.

$$= \varphi(\omega_0) + \left.\frac{\partial\varphi}{\partial\omega}\right|_{\omega_0}(\omega-\omega_0) + \frac{1}{2}\left.\frac{\partial^2\varphi}{\partial\omega^2}\right|_{\omega_0}(\omega-\omega_0)^2 + \frac{1}{6}\left.\frac{\partial^3\varphi}{\partial\omega^3}\right|_{\omega_0}(\omega-\omega_0)^3 + \mathcal{O}(\omega^4).$$

The constant $\varphi(\omega_0)$ is again the carrier-envelope offset phase. The first derivative is defined as the group delay

$$\tau_g = \left.\frac{\partial\varphi}{\partial\omega}\right|_{\omega_0}. \tag{2.14}$$

It has units of time, usually fs. The shift theorem of Fourier transforms implies that this linear contribution to the spectral phase causes a shift τ_g of the pulse in time. The group delay can be interpreted as the time that the pulse spends in the dispersive material. The inverse of the group delay per unit length yields the group velocity

$$v_g = \left(\left.\frac{\partial k}{\partial\omega}\right|_{\omega_0}\right)^{-1}, \tag{2.15}$$

where the wave vector k is related to the frequency via the refractive index n of the dispersive medium $k(\omega) = \omega/c \cdot n(\omega)$. When the pulse passes through a dispersive material of thickness l, the induced group delay is l/v_g.

The second-order (quadratic) phase variation in equation (2.13) is the group-delay dispersion GDD $= \left.\frac{\partial^2\varphi}{\partial\omega^2}\right|_{\omega_0} = \frac{\partial\tau_g}{\partial\omega}$. It is also consistent with the derivative of the group delay (see equation (2.14)). It is typically given in units of fs^2. In analogy to before, the GDD per unit length is the group-velocity dispersion (GVD).

The third order (cubic) contribution is regarded as the third-order dispersion TOD $= \left.\frac{\partial^3\varphi}{\partial\omega^3}\right|_{\omega_0}$ and is usually specified in fs^3.

The GDD leads to a linear change of the group delay with frequency (also termed linear chirp). The lower and higher frequency components are shifted differently in time. The case of positive GDD is called normal dispersion. Anomalous dispersion is characterized by a negative GDD. Positive (negative) GDD means that the instantaneous frequency increases (decreases) linearly in time. The TOD (called quadratic chirp) shifts the frequencies in such way that the pulse can be broken up into several subpulses. The influence of the different chirp components is illustrated in Fig. 2.2.

As demonstrated, the temporal and spectral phases determine the actual structure of the laser pulses. Thus, controlling the phase of laser pulses, especially the spectral phase, represents a very efficient tool to shape the pulses in the desired manner. Further information on how this can be done experimentally and how special phase variations influence the pulse shape is provided in chapter 3.3.2.

2.2 Autocorrelation

Usually, the pulse shapes and exact temporal durations of the pulses delivered by the laser systems are not known. One method to characterize ultrashort laser pulses is the correlation technique. The details of this method presented in this section are primarily derived from [44].
If a reference pulse $E_{\mathrm{ref}}(t)$ is available, the actual laser pulse $E_{\mathrm{laser}}(t)$ can be derived by applying the first-order correlation function

$$F_{\mathrm{c}}(\tau) = \int_{-\infty}^{\infty} dt\, E_{\mathrm{laser}}(t)\, E_{\mathrm{ref}}(t-\tau). \tag{2.16}$$

However, in most cases it is very difficult (if possible at all) to generate a reference pulse shorter than the laser pulse under investigation. Furthermore, the shape of the reference signal is most likely also not known and would have to be determined too. Therefore, as general approach the laser pulse itself acts as its own reference. This leads to the so-called autocorrelation $A_{\mathrm{c}}(\tau)$

$$A_{\mathrm{c}}(\tau) = \int_{-\infty}^{\infty} dt\, E(t)\, E(t-\tau). \tag{2.17}$$

Such an autocorrelation is obtained experimentally by an interferometric setup (e.g. Mach-Zehnder or Michelson interferometer). An identical copy of the laser pulse is produced and the two replicas are time-delayed against each other. The signal detected when scanning the time delay τ is given by

$$S^{(1)}(\tau) = \int_{-\infty}^{\infty} dt\, |E(t)+E(t-\tau)|^2 \tag{2.18}$$

which can be written in terms of the first-order autocorrelation function $A_{\mathrm{c}}^{(1)}(\tau)$ as $S^{(1)}(\tau) \propto 2\int dt\, I(t) + 2A_{\mathrm{c}}^{(1)}(\tau)$. As described in [44], for the full reconstruction of the electric field $E(t)$ all higher-order functions have to be measured.

The second-order correlation reads as

$$S^{(2)}(\tau) = \int_{-\infty}^{\infty} dt\, \left|[E(t)+E(t-\tau)]^2\right|^2 \tag{2.19}$$

and can be realized by two-photon processes like second-harmonic generation (cf. section 2.3) or sequential two-photon double ionization as it is described for deuterium

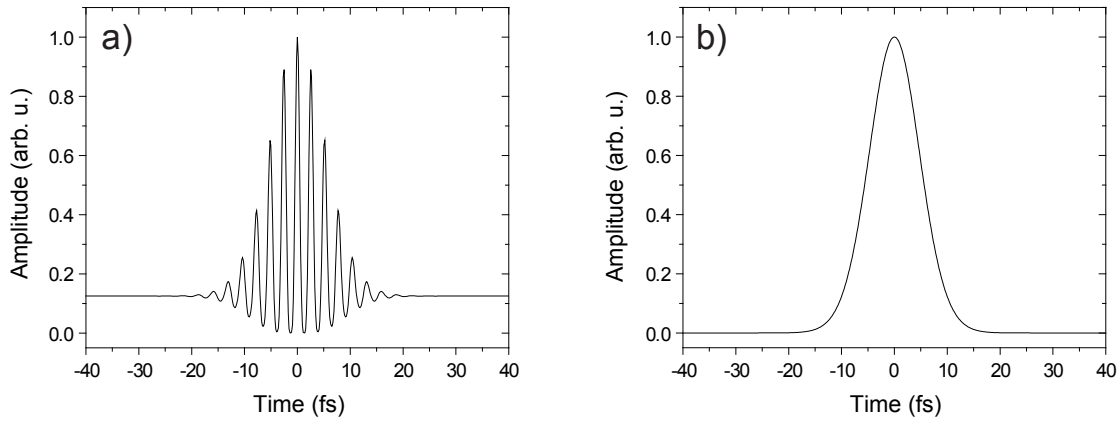

Figure 2.3: Second-order autocorrelation signals. (a) Interferometric autocorrelation signal $S^{(2)}(\tau)$ and (b) intensity autocorrelation signal $S_{\mathrm{I}}^{(2)}(\tau)$ of a bandwidth-limited ~ 7.6 fs pulse with a center frequency of 2.44 fs^{-1}. In (b) the "background" term $2\int dt\, I^2(t)$ is subtracted so that only the intensity correlation $\int dt\, I(t)\cdot I(t-\tau)$ is plotted. Corresponding to equation (2.24) the FWHM of the intensity autocorrelation amounts to $\sigma_{\mathrm{FWHM}} = \sqrt{2}\cdot 7.6\,\mathrm{fs} \approx 10.74\,\mathrm{fs}$.

molecules in chapter 5.1. Similarly the *n*th-order correlation can be determined in an *n*-photon process.

In the experiment, the second-order correlation function is detected by an autocorrelator which is a commercially available device. Such an autocorrelator is based on an interferometer setup with the subsequent second-harmonic generation in a nonlinear crystal. Depending on the time delay τ, the second-harmonic light is measured. Two measurement types can be distinguished: (i) interferometric autocorrelations and (ii) intensity autocorrelations.

An example of a second-order interferometric autocorrelation signal is displayed in Fig. 2.3(a). The signal is characterized by the contrast ratio of 8:1 between the amplitudes at $\tau = 0$ and $\tau \to \infty$. The amplitudes are

$$S^{(2)}(\tau = 0) = 16 \int dt\, E^4(t) \quad \text{and} \quad S^{(2)}(\tau \to \infty) = 2 \int dt\, E^4(t). \tag{2.20}$$

If the interferometric autocorrelation is averaged over the delay, the intensity autocorrelation is obtained with a signal yielding

$$S_{\mathrm{I}}^{(2)}(\tau) = 2 \int dt\, I^2(t) + 4 \int dt\, I(t)\, I(t-\tau) \tag{2.21}$$

which contains the second-order autocorrelation function

$$A_{\mathrm{c}}^{(2)}(\tau) = \frac{\int dt\, I(t)\, I(t-\tau)}{\int dt\, I^2}. \tag{2.22}$$

The equations (2.20) and (2.21) can be derived from equation (2.19) by inserting the electric fields $E(t) = E(t)\exp[i(\omega t + \phi(t))]$ and $E(t-\tau) = E(t-\tau)\exp[i(\omega(t-\tau) + \phi(t-\tau))]$, respectively, expanding it into all terms and taking the corresponding limits. For details refer to [44].

Obviously the expression "intensity autocorrelation" originates from the fact that the intensity correlation $\int dt\, I(t)\cdot I(t-\tau)$ appears in equation (2.21) which is in contrast to the

electric-field correlation in equation (2.16). Figure 2.3(b) illustrates a typical intensity autocorrelation signal. The technique of intensity autocorrelation is widely used to determine the pulse duration. For instance, if a Gaussian envelope $I(t) \propto \exp(-2t^2/t_G^2)$ is given, the resulting intensity autocorrelation is

$$A_c^{(2)}(\tau) \propto \int_{-\infty}^{\infty} dt\, e^{-\frac{2t^2}{t_G^2}}\, e^{-\frac{2(t-\tau)^2}{t_G^2}} \propto e^{-\frac{\tau^2}{t_G^2}}. \tag{2.23}$$

Recalling equation (2.8), the actual pulse duration t_{pulse} is related to the FWHM of the intensity autocorrelation σ_{FWHM} by

$$\sigma_{\text{FWHM}} = \sqrt{2} \cdot t_{\text{pulse}}. \tag{2.24}$$

However, the autocorrelation signals are strongly dependent on the spectral phase and hence the signal shapes are complicated to interpret. Only some information about the temporal duration can be derived. Since the phase of the electric field cannot be determined by the autocorrelation (or crosscorrelation) technique, other more sophisticated pulse characterization methods (like frequency-resolved optical gating or spectral-phase interferometry for direct electric field reconstruction) are necessary for the full pulse characterization. Further information on these techniques can be found in [47–49] or in the standard textbooks already listed at the beginning of this chapter. Another technique for pulse characterization, called multiphoton intrapulse interference phase scan (MIIPS), was designed and set up as part of this thesis and more details can be found in chapter 3.3.2.

2.3 Nonlinear optics: second-harmonic generation

In section 2.2 it is described that not only first-order, but also higher-order processes play an important role in the characterization of laser pulses using cross- or autocorrelations. Explicitly, the second-harmonic generation (SHG) in nonlinear crystals is mentioned. This section deals with nonlinear optical effects, especially discussing the second-order process, and mainly refers to [45, 46].

From conventional linear optics it is known that an oscillating electric field $\widetilde{E}(t)$ propagating through some macroscopic material induces a polarization $\widetilde{P}(t)$ which linearly depends on the electric field strength:

$$\widetilde{P}(t) = \varepsilon_0\, \chi\, \widetilde{E}(t) \tag{2.25}$$

with the permittivity in empty space ε_0 and the susceptibility χ. In general, the susceptibility is a tensor taking into account the anisotropy of the dielectric material. However, for an isotropic medium χ becomes a scalar and the polarization is parallel to the electric field. This isotropic case is considered in the following for simplicity.
The linear relation between $\widetilde{P}(t)$ and $\widetilde{E}(t)$ holds only for low electric field strengths, i.e. low pulse intensities. If the electric field strengths become comparable to the interatomic fields, the polarization response of the medium becomes a nonlinear function

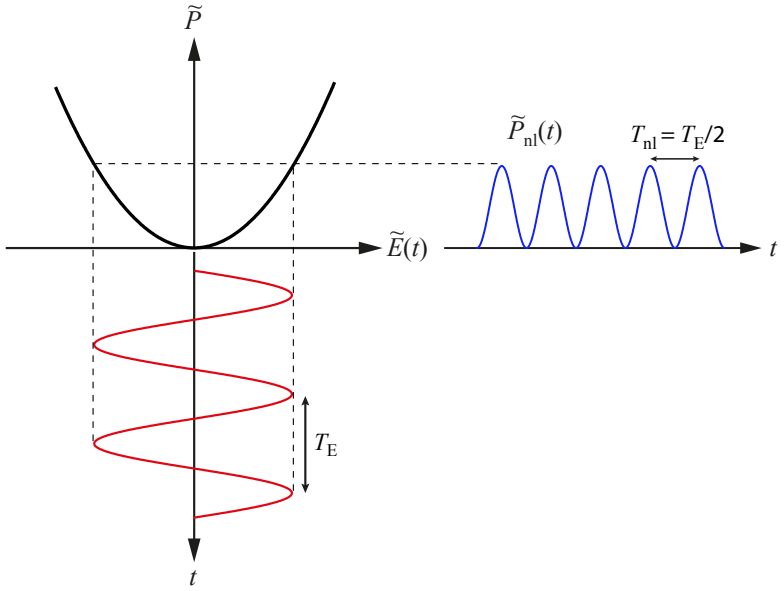

Figure 2.4: Second-order nonlinear polarization. In a second-order nonlinear material a periodic electric field $\widetilde{E}(t)$ with frequency ω generates a polarization $\widetilde{P}_{\mathrm{nl}}(t)$ which includes a component at frequency 2ω giving rise to the emission of second-harmonic light. Figure based on [46].

of the electric field. Typical interatomic electric field strengths are on the order of about $10^5 - 10^8$ V/m. Thus, the polarization needs to be written as

$$\widetilde{P}(t) = \varepsilon_0 \left(\chi^{(1)} \widetilde{E}(t) + \chi^{(2)} \widetilde{E}(t)^2 + \chi^{(3)} \widetilde{E}(t)^3 + ... \right) = \varepsilon_0 \chi^{(1)} \widetilde{E}(t) + \widetilde{P}_{\mathrm{nl}}(t) \tag{2.26}$$

for higher intensities, where $\chi^{(2)}$ describes the strength of the second-order and $\chi^{(3)}$ of the third-order nonlinear effects and so on.

From the Maxwell equations the driven nonlinear wave equation (for homogenous and isotropic materials) can be derived (cf. [45,46]) and reads as

$$\nabla^2 \widetilde{E} - \frac{1}{c_0^2} \frac{\partial^2 \widetilde{E}}{\partial t^2} = \mu_0 \frac{\partial^2 \widetilde{P}_{\mathrm{nl}}}{\partial t^2} = -S(t), \tag{2.27}$$

where $S(t)$ corresponds to an emitting source.

The second-harmonic generation is an example for a second-order nonlinear interaction between a laser pulse and a crystal with $\chi^{(2)} \neq 0$. When the laser electric field is given by

$$\widetilde{E}(t) = \frac{1}{2} \left(E_0 \, e^{i\omega t} + E_0^* \, e^{-i\omega t} \right), \tag{2.28}$$

the nonlinear polarization can be expressed as

$$\widetilde{P}_{\mathrm{nl}}^{(2)}(t) \propto \chi^{(2)} \widetilde{E}(t)^2 = \frac{1}{2} \chi^{(2)} E_0 E_0^* + \frac{1}{4} \chi^{(2)} E_0^2 \, e^{i2\omega t} + \frac{1}{4} \chi^{(2)} E_0^{*2} \, e^{-i2\omega t}. \tag{2.29}$$

Two contributions can be identified, namely at zero frequency and at the double frequency 2ω. Taking the wave equation (2.27) into account, the zero frequency component does not

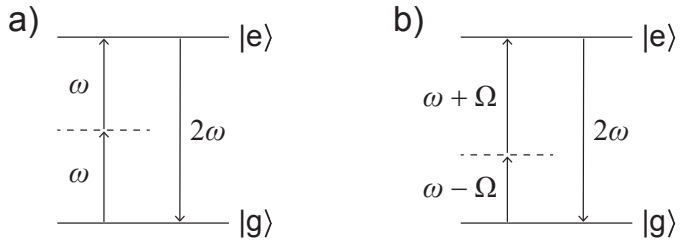

Figure 2.5: Schematical representation of the second-harmonic generation process. (a) Two photons of the original frequency ω are converted into one photon of frequency 2ω. (b) Not only contributions with equal omega in both photons are possible, but also from the combination of a photon with frequency $\omega - \Omega$ and a photon with frequency $\omega + \Omega$.

contribute to the source $S(t)$. However, the second time derivative of the 2ω-component does not vanish and electromagnetic radiation at the double frequency is emitted. The process is schematically shown in Fig. 2.4.
The nonlinear crystals typically used for the second-harmonic generation are potassium dihydrogen phosphate (KDP), KH_2PO_4, or beta barium borate (BBO), β-BaB_2O_4.

In the time domain, the second-harmonic electric field is given by the squared carrier field $\widetilde{E}(t)^2 \propto \exp(i2\omega t)$. The representation in the frequency domain is obtained by the Fourier transform

$$E_s(2\omega) = \mathscr{F}\left\{\widetilde{E}(t)^2\right\} = \mathscr{F}\left\{\widetilde{E}(t)\cdot\widetilde{E}(t)\right\} \tag{2.30}$$

with the fundamental frequency ω. Applying the convolution theorem for Fourier transforms

$$\mathscr{F}\left\{\widetilde{E}(t)\cdot\widetilde{E}(t)\right\} \propto \mathscr{F}\left\{\widetilde{E}(t)\right\} * \mathscr{F}\left\{\widetilde{E}(t)\right\} \tag{2.31}$$

and inserting the known result of the Fourier transform $\mathscr{F}\left\{\widetilde{E}(t)\right\} = E_s(\omega)$ yields

$$E_s(2\omega) \propto \int d\eta\, E_s(\eta)\, E_s(2\omega - \eta). \tag{2.32}$$

The equation can be further modified by substituting the integration variable for $\eta = \omega + \Omega$ and the result reads as

$$E_s(2\omega) \propto \int d\Omega\, E_s(\omega + \Omega)\, E_s(\omega - \Omega). \tag{2.33}$$

The intensity of the SHG spectrum is finally derived by taking the absolute square of $E_s(2\omega)$:

$$I(2\omega) \propto \left| \int d\Omega \left|\widetilde{E}(\omega+\Omega)\right| \left|\widetilde{E}(\omega-\Omega)\right| e^{i[\varphi(\omega+\Omega)+\varphi(\omega-\Omega)]} \right|^2. \tag{2.34}$$

In the photon picture, the second-harmonic generation process can be understood as the conversion of two photons of frequency ω into one photon of frequency 2ω. Moreover, equations (2.33) and (2.34) reveal that the combination of a photon with frequency $\omega + \Omega$ and a photon with frequency $\omega - \Omega$ contributes to the spectral distribution at 2ω as well. This interpretation is depicted in Fig. 2.5. However, the SHG intensity depends on the spectral phase $\varphi(\omega)$. This behaviour plays an important role for the pulse characterization method presented in chapter 3.3.2.

2.4 Fundamentals of absorption

As described in the previous section, an electric field passing through an isotropic medium causes a polarization P. The following discussion is mainly based on [43, 45, 46] and further details can be found therein.
Taking only the linear relation into account, the polarization is defined as

$$P(\omega) = \varepsilon_0 \chi^{(1)}(\omega) E_s(\omega), \tag{2.35}$$

where the linear susceptibility $\chi^{(1)}(\omega)$ is a complex quantity in general. This is the macroscopic description of the polarization. However, there is a microscopic derivation as well. On the atomic or molecular level, the electric field shifts the electrons relative to the nuclei and a dipole moment d is induced which is given by the product of the charge q and the displacement x:

$$d = q\,x. \tag{2.36}$$

The induced dipole d can also be expressed by the polarizability $\widetilde{\alpha}(\omega)$ (of an atom or molecule) via

$$d = \widetilde{\alpha}(\omega) E_s. \tag{2.37}$$

The polarization is the sum over all induced dipole moments, yielding

$$P = n\,d = n\,q\,x = n\,\widetilde{\alpha}(\omega) E_s \tag{2.38}$$

with the number density n of the induced dipoles.

The oscillation of the electrons around the atoms caused by the driving electric field $E_s = E_0 \cdot \exp(i\omega t)$ is classically modeled by a damped harmonic oscillator (also known as the Lorentz oscillator model):

$$\ddot{x} + \gamma \dot{x} + \omega_0^2 x = \frac{q}{m} E_0 \cdot e^{i\omega t} \tag{2.39}$$

with the mass m, the damping constant γ and the resonance frequency ω_0. Choosing $x = x_0 \cdot \exp(i\omega t)$ as ansatz, the solution is given by

$$x_0 = \frac{q\,E_0}{m\,(\omega_0^2 - \omega^2 + i\,\gamma\,\omega)}. \tag{2.40}$$

Combining equations (2.38) and (2.35) and inserting the solution for $x(t)$, the following relation for the linear susceptibility is found:

$$\chi^{(1)}(\omega) = \frac{n\,q\,x}{\varepsilon_0 E_s} = \frac{n\,q^2}{\varepsilon_0\,m} \frac{1}{(\omega_0^2 - \omega^2 + i\,\gamma\,\omega)}. \tag{2.41}$$

The complex susceptibility can be expressed by its real and imaginary part

$$\chi^{(1)}(\omega) = \chi'(\omega) + i\,\chi''(\omega) \tag{2.42}$$

$$= \frac{n\,q^2}{\varepsilon_0\,m} \frac{\omega_0^2 - \omega^2}{(\omega_0^2 - \omega^2)^2 + \gamma^2\,\omega^2} + i\,\frac{n\,q^2}{\varepsilon_0\,m} \frac{\gamma\,\omega}{(\omega_0^2 - \omega^2)^2 + \gamma^2\,\omega^2}.$$

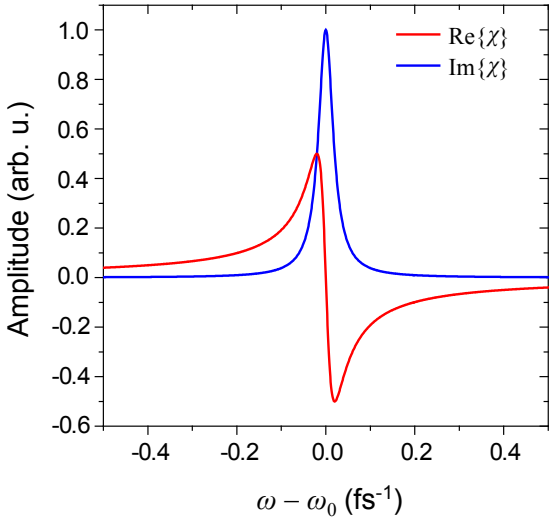

Figure 2.6: Dispersion and absorption. The real part (red line) and the imaginary part (blue line) of the complex susceptibility $\chi^{(1)}(\omega)$ as given by equation (2.43) for $\omega_0 = 2.44$ fs^{-1} ($\cong$ 780 nm) and $\gamma = 0.04$ fs^{-1}. The typical Lorentzian shape of the absorption line is obvious.

Close to the resonance frequency $\omega \approx \omega_0$ holds and the approximation $(\omega_0^2 - \omega^2) \approx 2\,\omega_0\,(\omega_0 - \omega)$ is valid so that equation (2.42) can be simplified to

$$\chi^{(1)}(\omega) = \frac{n\,q^2}{2\,\varepsilon_0\,m\,\omega_0}\,\frac{\omega_0 - \omega}{(\omega_0 - \omega)^2 + (\gamma/2)^2} + i\,\frac{n\,q^2}{4\,\varepsilon_0\,m\,\omega_0}\,\frac{\gamma}{(\omega_0 - \omega)^2 + (\gamma/2)^2}. \tag{2.43}$$

The shape of the imaginary part χ'' follows the well-known Lorentzian function describing absorption lines. The real and imaginary part of the susceptibility are displayed in Fig. 2.6. For an atom or a molecule, ω_0 corresponds to the resonance frequency of a transition from the ground to an excited state. The quantity γ is the FWHM of the Lorentzian function and corresponds to the natural absorption line width.

The characteristics dispersion and absorption of a medium are combined in the complex refractive index $n(\omega) = n' + i\,n'' = \sqrt{1 + \chi^{(1)}(\omega)}$. In case the medium is dilute and the susceptibility is small, both effects can be disentangled and it is possible to write

$$n(\omega) \approx 1 + \frac{1}{2}\,\chi^{(1)}(\omega) = 1 + \frac{1}{2}\,\chi'(\omega) + i\,\frac{1}{2}\,\chi''(\omega). \tag{2.44}$$

The absorption can be identified as the imaginary part and the dispersion as the real part of $n(\omega)$ and hence of the susceptibility. The absorption coefficient α is related to the imaginary part of the refractive index via

$$\alpha(\omega) = 2\,\frac{\omega}{c}\,n'' = \frac{\omega}{c}\,\chi''(\omega). \tag{2.45}$$

The absorption coefficient determines the fraction of the incident light intensity that is transmitted through a material of thickness l. This behaviour is described by the Lambert-Beer law

$$I(\omega, l) = I_0(\omega) \cdot e^{-\alpha(\omega)\,l} = I_0(\omega) \cdot e^{-n\,\sigma(\omega)\,l}. \tag{2.46}$$

Here, the absorption coefficient is substituted by the absorption cross section $\sigma(\omega)$ and the number density of absorbers n in the second step. Recalling now equations (2.35), (2.38) and (2.45), the absorption cross section can be directly expressed in terms of the induced dipole $d(\omega)$:

$$\sigma(\omega) = \frac{\alpha(\omega)}{n} = \frac{\omega}{n\,c}\,\mathrm{Im}\{\chi(\omega)\} = \frac{\omega}{\varepsilon_0\,c}\,\mathrm{Im}\left\{\frac{d(\omega)}{E_\mathrm{s}(\omega)}\right\}. \tag{2.47}$$

The ratio between the transmitted light and the incident light is usually specified as "optical density" (OD) which is defined as

$$OD = -\log_{10}\left(\frac{I}{I_0}\right) = \frac{n\,\sigma\,l}{\ln 10}. \tag{2.48}$$

An optical density of $OD = 1$ means that 10 % of the incident light are transmitted, $OD = 2$ corresponds to 1 %, $OD = 3$ to 0.1 % and so forth.

2.5 Wave-packet dynamics

When studying the dynamics of electrons in atoms and molecules, usually the motion of wave packets is observed. A wave packet is the coherent superposition of at least two quantum states. Such a coherent two-state superposition can be expressed as

$$\Psi(t) = a_1(t)\,\psi_1 + a_2(t)\,\psi_2. \tag{2.49}$$

The temporal evolution of a quantum state is described by the time-dependent Schrödinger equation

$$i\hbar\,\frac{\partial}{\partial t}\,|\Psi(t)\rangle = \hat{H}\,|\Psi(t)\rangle \tag{2.50}$$

with the wave function $|\Psi(t)\rangle$ and the Hamilton operator $\hat{H}$. In general, the Hamilton operator includes the kinetic term and the occurring interactions, e.g. atomic or molecular Coulomb potentials and interactions with laser fields. If there are no external interactions, i.e. in the unperturbed case, $\hat{H} = \hat{H}_0$ becomes time independent and the Schrödinger equation stationary. Then, the solutions are given by the eigenfunctions $|\psi_n\rangle$ with the eigenvalues E_n. In order to solve the time-dependent equation, the wave function is expanded into the eigenfunctions

$$|\Psi(t)\rangle = \sum_n c_n(t)\,|\psi_n\rangle\,, \tag{2.51}$$

where the coefficients $c_n(t)$ are complex-valued and given by

$$c_n(t) = c_{0,n}\cdot e^{-i\omega_n t} = c_{0,n}\cdot e^{-i\frac{E_n}{\hbar}t}. \tag{2.52}$$

Equation (2.51) corresponds to the coherent superposition of n quantum states.

Experimentally, the development of femtosecond lasers opened the way towards exploring wave-packet dynamics. The vibrations in molecules occur on a time scale of a few

to tens of femtoseconds. The availability of such ultrashort pulses enabled the generation of wave packets in molecules and also the probing of their evolution in time. The wave-packet dynamics is usually studied using pump–probe spectroscopy techniques: A first laser pulse acts as pump pulse and transfers the atoms or molecules into a coherent superposition of excited states. A second pulse probes the induced dynamics as a function of the time delay τ between the pump and probe pulse. In case of molecules for instance, the broadband laser pulses are capable to cover the energy range of a number of vibrational states. Vibrational states are simultaneously populated by the pump pulse giving rise to molecular wave packets. The molecular vibration results in a change of the internuclear distance R. The observable measured in the experiment is the expectation value $\langle \Psi | R | \Psi \rangle$ and describes the molecular vibration. Inserting equations (2.51) and (2.52), the expectation value for the internuclear distance reads as

$$\begin{aligned} \langle \Psi | R | \Psi \rangle &= \sum_n \sum_m c_{0,n}^* \, c_{0,m} \, e^{-i(\omega_m - \omega_n)t} \, \langle \psi_n | R | \psi_m \rangle \\ &= \sum_n \sum_m c_{0,n}^* \, c_{0,m} \, e^{-i\frac{E_m - E_n}{\hbar}t} \, \langle \psi_n | R | \psi_m \rangle \, . \end{aligned} \tag{2.53}$$

It directly becomes clear that a wave-packet dynamics is only present if at least two eigenstates are superposed, otherwise $\langle \Psi | R | \Psi \rangle$ will be constant in time. The period of the wave-packet oscillation $T = 2\pi/\omega = 2\pi\hbar/(E_m - E_n)$ is determined by the energy difference of the states.
In an experiment, the probe pulse typically promotes the molecules into dissociating states and the resulting fragments (ions) and their energy or momentum distributions are detected. As the measured distributions depend on the pump–probe time delay and hence on the internuclear distance R at which the molecular wave packet is transferred into the dissociating states, the wave-packet motion can be revealed. Further information about experimental techniques is provided in the following chapter 3 and an experiment on the measurement of molecular wave-packet dynamics is discussed in section 5.1.

A simple model for a wave packet is displayed in Fig. 2.7. The first three eigenfunctions of the quantum harmonic oscillator ($n = 0, 1, 2$) are chosen

$$\psi_n(x) = \frac{1}{\sqrt{\sqrt{\pi}\, 2^n \, n!}} \, H_n(x) \, e^{-\frac{x^2}{2}} \tag{2.54}$$

with the Hermite polynomials $H_n(x)$. The total wave function $\Psi(x,t)$ is determined as the superposition of the three eigenfunctions using equation (2.51). The square of its absolute value, representing the probability density, is plotted for times $t = 0, 0.1, 0.2, 0.3, 0.4$ and $0.5 \cdot T$. The motion of the wave packet from the right to the left which corresponds to half of one period is clearly visible.

The theoretical basics of quantum mechanics used in this section can be found in any standard textbook like [50,51]. An overview of the theoretical description of wave packets and their experimental investigation, especially considering femtosecond chemistry, is given in [52–54] for example.

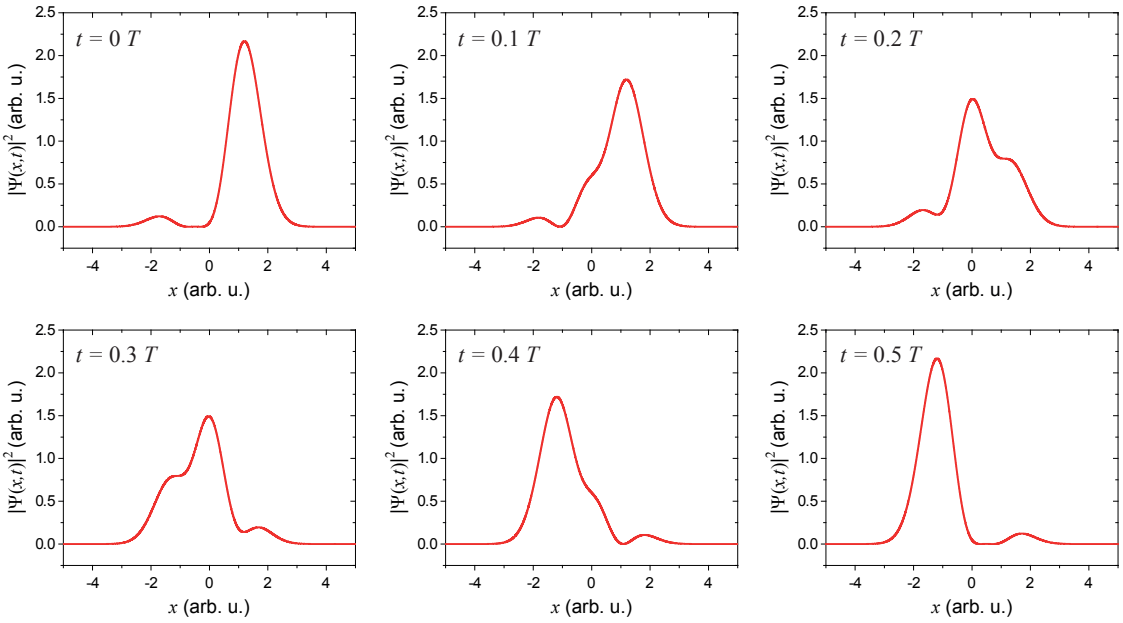

Figure 2.7: Illustration of a wave packet. The superposition of the lowest three eigenfunctions of the quantum harmonic oscillator yields the wave function $\Psi(x,t)$ of a wave packet. The oscillation of the wave packet $|\Psi(x,t)|^2$ is depicted for times $t = 0, 0.1, 0.2, 0.3, 0.4$ and $0.5 \cdot T$ corresponding to half of one period. The full oscillation is obtained when reading the panels in reversed order.

Chapter 3

Experimental methods and setup

The aim of this chapter is to introduce the experimental tools and techniques that are required in the framework of this thesis. In the first section different types of (coherent) light sources are described. Then, some information about the detection methods is provided. The last section presents the experimental setup that was designed and assembled to perform the experiments discussed in the following chapters 4 and 5.

3.1 Light sources

The workhorses in atomic, molecular and condensed matter physics, but also in material sciences and even everyday life are lasers (acronym for Light Amplification by Stimulated Emission of Radiation). Be it in science (e.g. spectroscopy and cooling atoms to ultracold temperatures), in optical communications, in medicine (e.g. ophthalmology), in industry (e.g. cutting materials) or consumer electronics (e.g. laser pointers, Blu-ray discs) – there is a vast field of applications for lasers.
There are also a lot of different types of lasers. They can be classified into dye, gas or solid state lasers depending on the active laser medium that is used. For instance, rhodamines, coumarins or stilbenes are applied as typical dyes. The first gas laser, the Helium-Neon laser, was developed 1960 by A. Javan, W. R. Bennett and D. R. Herriott [55]. Laser diodes are widely used semiconductor lasers, e.g. in laser pointers, CD/DVD-reading and fiber optics communications. The spectral range covered by the various laser types ranges from the ultraviolet (e.g. excimer lasers) over the visible to the mid-infrared (e.g. the CO_2-laser which emits at 10.6 µm) and even far-infrared. The power can vary from a few nanowatts (nW) to several kilowatts (kW). In a further classification the laser can be divided into continuous wave (cw) and pulsed lasers.
However, there are also light sources providing radiation from the microwave to the X-ray regime, so-called Free-Electron Lasers (FELs). In the 70s of the last century, a high interest in FELs was triggered by the publication of John M. J. Madey [56] introducing a theory for the FEL. The first operation of such an FEL, i.e. amplification and lasing, was reported in the mid 1970s [57, 58]. Further information about the working principle of FELs is provided in section 3.1.2.

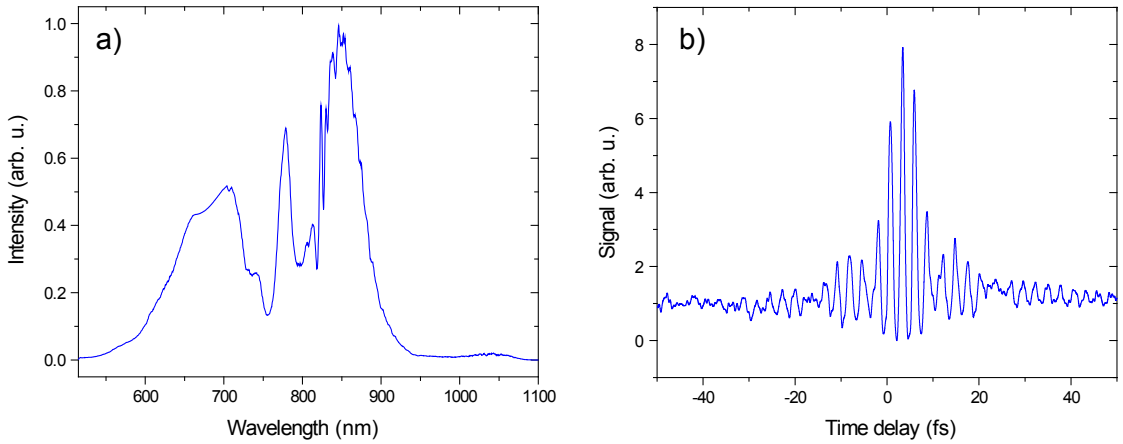

Figure 3.1: Short-pulse generation. The measured spectrum (a) and measured autocorrelation (b) of the produced pulses after focusing the 30 fs pulses from the Ti:sapphire laser into the hollow-core fiber. The power of the incident laser beam amounted to ~ 2.1 W and the fiber was filled with Neon gas at an absolute pressure of 2.2 bar. The achieved pulse duration is approximately 4.9 fs.

3.1.1 Laser system

The atomic and molecular dynamics occurs on extremely short time scales. Molecular vibrations take place on time scales in the femtosecond range (1 fs $= 10^{-15}$ s) for example. The electron dynamics in atoms happens on even shorter times, i.e. in the attosecond regime (1 as $= 10^{-18}$ s). In order to probe such dynamics, ultrashort laser pulses are required.
The laser system used for the various experiments in our laboratory is the commercially available "Femtopower compact Pro CEP" by Femtolasers [59]. It delivers sub-30 fs short pulses centered around a wavelength of 800 nm at a repetition rate of 4 kHz and pulse energies of approximately 0.8 mJ. The carrier envelope phase (CEP) can be stabilized as well. The laser system consists of three sections: oscillator, amplifier and compressor.
The oscillator, "Femtosource Rainbow" [60], is a titanium-doped sapphire (Ti:Sa) laser pumped at a wavelength of 532 nm by a frequency-doubled continuous-wave Nd:YAG laser (Verdi, Coherent) at a power of 3.2 W. The oscillator provides pulses with a duration of ~ 10 fs at a center wavelength of typically 800 nm. The pulse energies reach a few nanojoules at a repetition rate of 80 MHz. The technique applied to amplify the pulses to energies of a few millijoules is called "chirped pulse amplification" [61]. By introducing a large temporal chirp, the pulses are stretched to picoseconds or even nanoseconds before they enter the amplifier section of the laser system. Thereby, the peak power (which could easily reach tens of gigawatts, even for such small-scale systems) is significantly reduced and any damage of the optical components is avoided.
The amplifier is based on a Ti:Sa crystal in the same way as the oscillator, but it is pumped by a high power (~ 30 W), Q-switched laser (DM-30, Photonics Industries) at a repetition rate of 4 kHz. After the amplified pulses passed through the amplifier crystal nine times, they reach the compression section. It is a two-prism compressor compensating the chirp imprinted on the pulses and thus yielding finally about 30 fs short laser pulses.

Even shorter pulses can be produced by a compression technique [62] which is based

on the effect of self-phase modulation (SPM) that leads to a broadening of the spectrum [42, 63]. The laser pulses are focused into a hollow-core fiber (Kaleidoscope, Femtolasers [64]). The fiber has a length of approximately 70 cm and is filled with Neon gas (up to an absolute pressure of about 2.5 bar). Due to the process of SPM, the spectrum is significantly broadened to the shorter and longer wavelength regime. The subsequent propagation through a chirped mirror compressor (consisting of dispersive multilayer mirrors) compresses the pulses to a duration of about 7 fs and even below, (nearly) reaching their Fourier limit. A typical spectrum of a generated ~ 4.9 fs short pulse and the corresponding autocorrelation recorded with an autocorrelator (Femtometer, Femtolasers [65]) after the hollow-core fiber for a Neon gas pressure of 2.2 bar and a power of 2.1 W of the incident laser beam is shown in Fig. 3.1. More details about the laser system are provided in [66, 67].

3.1.2 Free-Electron Lasers

A different class of light sources are the Free-Electron Lasers (FELs). In contrast to the commercially available table-top laser systems, Free-Electron Laser sources can be found at research centers like the DESY (Deutsches Elektronen-Synchrotron) at Hamburg, Germany, or the Stanford Linear Accelerator Center (SLAC), USA. Such sources provide coherent radiation not only in the infrared or visible range, but also in the X-ray regime down to wavelengths in the sub-angstrom regime.
The key ingredient of an FEL are bunched relativistic electrons. The electrons are typically generated in a laser-driven photoninjector section and then accelerated to relativistic energies (several hundred MeV and up to a few GeV). The electron bunches are injected into the so-called undulator. It consists of periodically arranged magnets with alternating polarity (cf. Fig. 3.2). In the undulator magnetic field, the electrons follow a wavelike (sinusoidal) trajectory. As a consequence, the relativistic high-energy electrons emit spontaneously synchrotron radiation. This spontaneous undulator radiation acts as a seed during the further propagation of the electrons through the undulator. The light wave present in the undulator induces a modulation of the longitudinal electron velocity: some electrons gain energy, whereas some electrons lose energy. As a result, a modulation of the electron density appears in each bunch. This process is termed microbunching. The electrons in such a microbunch emit coherent radiation like one macroscopic single charge. The modulation period is given by the wavelength λ of the emitted radiation which is described by the fundamental undulator equation

$$\lambda = \frac{\lambda_u}{2\gamma^2} \cdot \left(1 + \frac{K^2}{2}\right). \tag{3.1}$$

γ is the Lorentz factor, λ_u the period of the undulator (cf. Fig. 3.2) and K the undulator parameter. The undulator parameter depends on the undulator magnetic field B and is defined by

$$K = \frac{e\lambda_u B}{2\pi m_e c}. \tag{3.2}$$

Hence, by controlling the electron energy the wavelength of the emitted light pulses can be tuned.

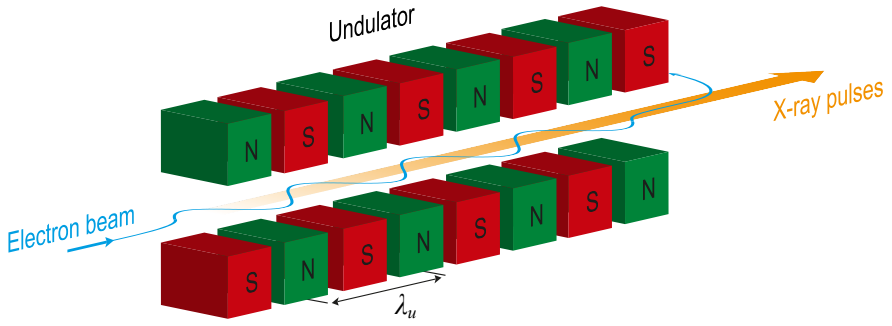

Figure 3.2: Sketch of the undulator section (based on [68, 69]). The relativistic high-energy electrons enter the undulator which consists of periodically arranged magnets with alternating polarity. The electron bunches are guided on a wavelike trajectory by the magnetic field. Self-amplified spontaneous emission leads to the generation of intense X-ray pulses.

Starting from spontaneous emission, i.e. incoherent radiation, the microbunching leads to the emission of coherent radiation, amplified in the undulator. This working principle of FELs is called self-amplified spontaneous emission (SASE). While in the beginning the power of the (incoherent) spontaneous radiation is rather low, it increases exponentially with the length of the undulator. Typically, when all electrons are grouped into the microbunches the power levels off and the saturation regime is reached. This behaviour is displayed in Fig. 3.3.
As the SASE is a stochastic process, initiated by spontaneous emission, fluctuations of the pulse energy and the wavelength occur. These fluctuations are the highest in the exponential regime. The pulses provided by Free-Electron Lasers exhibit statistically varying pulse shapes from shot to shot. Moreover, the phase of the FEL pulses cannot be regarded as continuous, but it has to be noted that it is only partially coherent. Examples of FEL pulse shapes, their mathematical description and the benefits coming along with the pulse properties are provided in chapter 5.
For the generation of light pulses with wavelengths $\lambda < 100$ nm, typically only a single pass of the electron bunches through the undulator is possible, due to the absence of suitable reflecting optics, and a high gain must be ensured to obtain sufficient pulse powers. After the undulator the electrons are deflected by dipole magnets and guided into dumps. FEL sources operating in the visible- or infrared-wavelength regime are equipped with an optical resonator. The electrons circulate in a storage ring, for instance. The starting of the FEL can be induced by external seed lasers or by spontaneous undulator radiation. Although the gain is only a few percent per each turn, an output power in the range of gigawatts is possible provided that the number of turns is sufficiently large. The usage of an optical cavity is not feasible for short wavelengths, since the reflectivity of the metal coated mirrors reaches zero under normal incidence. Therefore, the generation of X-ray pulses relies on the SASE process as discussed above.
The given description follows mainly the explanations provided by [68, 69]. More details about Free-Electron Lasers can be found in [70–72] and references therein.

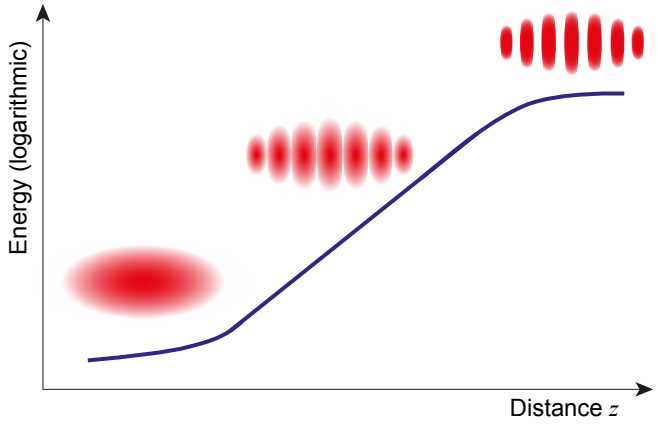

Figure 3.3: Schematic of the energy of the light pulses as a function of the distance z that the electron bunch traveled in the undulator (based on [68, 69]). In the beginning, spontaneous (incoherent) undulator radiation takes place. When the microbunching process sets in, the electrons start to emit coherently and the energy increases exponentially. When the mircobunching is finished, i.e. all electrons are grouped into the microbunches, saturation is reached.

3.2 Detection methods

The light sources discussed in the previous section 3.1 are widely-used tools to investigate the structure and dynamics of a large field of systems ranging from atoms and diatomic molecules up to complex systems like biomolecules. When the laser pulses are focused onto the target, one, two or several photons are absorbed by the atoms or molecules which leads to excitation into higher lying energy levels or to single or multiple ionization. To study the processes, two options are possible: (i) detecting the produced fragments, i.e. ions and electrons that Coulomb explode and dissociate due to the ionization, or (ii) looking at the light that is absorbed and/or emitted, i.e. measuring the absorption, fluorescence or stimulated emission.

As our working department comes with an excellent expertise in the field of ion and electron detection, the principle of a reaction microscope (ReMi) [73, 74] shall be explained here in short. However, there are various other detection methods available, e.g. velocity-map imaging [75].
The ReMi enables coincidence detection of electrons and ions. The ions and electrons are created in the interaction region where the laser beam is focused onto the target. The target is a cold, supersonic gas jet which contains the atoms or molecules to be studied. The produced ions are accelerated to the ion detector (typically a multichannel plate) via electric fields. A combination of electric and magnetic fields guides the electrons to the electron detector that is located opposite to the ion detection section. Both, ion and electron detectors, are position sensitive. As the time-of-flight of the fragments is measured as well, the momenta of the fragments can be reconstructed with high precision in three dimensions. If the target is sufficiently dilute, all generated electrons and ions can be measured in coincidence and the induced dynamics can be revealed entirely. It is not necessary that a laser beam serves as projectile, but the dynamics can be induced by ion or electron beams as well. The details of the ReMi technique and the momentum

reconstruction can also be found in [76, 77], for example, besides the already mentioned reviews.

A fully optical method for the investigation of structure and dynamics of systems is the detection of light, be it the fluorescence, stimulated emission or absorption. The fluorescence is characterized by its angular distribution of 4π, i.e. it is emitted into all directions. Stimulated emission and absorption can be observed in a certain direction only which is the propagation direction of the incident light. However, by simply measuring the (static) absorption no dynamics can be uncovered. In time-resolved spectroscopy, two time-delayed pulses are required as they are provided in pump–probe measurements. The first pulse excites the system (pump pulse), whereas the second pulse measures the absorbance (probe pulse). The probe pulse is weak in intensity so that it does not lead to any perturbations of the system, but serves to sample variations in the absorption induced by the pump pulse. By scanning the time delay between pump and probe pulse, changes in the detected absorption spectra can be related to the ongoing dynamics. This method is termed transient-absorption spectroscopy. The case of reversed temporal order, i.e. the probe precedes the pump pulse, is termed perturbed free polarization decay [78]. The transient-absorption measurements in the liquid phase carried out in the course of this thesis are discussed in chapters 4.2 and 5.3.
The optical detection is realized in these measurements by spectrometers where the laser light is split up into its frequency components by a grating. The spectrum is imaged onto a photosensitive detector, e.g. a CCD (charge-coupled device) camera. In the experiments, commercially available spectrometers by Ocean Optics are used. For the different applications, the following three spectrometers, which have a resolution of about 1 nm, are applied:

- USB2000+ spectrometer [79]: Wavelength range ∼506.7 - 1169.2 nm, 2048 pixels,
- USB4000 spectrometer [80]: Wavelength range ∼505.2 - 1178.3 nm, 3648 pixels,
- USB4000 spectrometer [80]: Wavelength range ∼177.1 - 898.5 nm, 3648 pixels.

In the measurements, the probe pulse is focused into an optical fiber (QP-200-2-UV-VIS, Ocean Optics [81]) and guided to the selected spectrometer.

3.3 Experimental setup

In this section the experimental setup for transient-absorption or 2D-spectroscopy measurements is introduced. It is the main tool to perform the experiments presented in chapters 4 and 5. Moreover, the technique of pulse shaping, including the setup and an implemented pulse characterization method, is explained in detail.

3.3.1 Transient-absorption or 2D-spectroscopy setup

The experimental setup for the transient-absorption measurements is designed in a compact, very stable and robust manner. Moreover, it can be used in 2D-spectroscopy ex-

periments without any further changes of the setup. A schematic drawing of the setup is depicted in Fig. 3.4. In transient-absorption measurements, two laser pulses (pump and probe) are necessary, whereas in 2D-spectroscopy experiments four beams are required.

The option for an easy switch between the two spectroscopy methods is provided by one central optical device: the four-split mirror. It is a home-built mirror assembly [2] and consists of four silver mirrors (size: 12.5 mm x 12.5 mm) that are arranged in a square. A picture of the mirror assembly with the numbering of the mirrors as used in the following is shown in Fig. 3.5. Each mirror is mounted to an 1/2"-kinematic mirror holder so that an independent alignment of the four mirrors is possible. The position of mirror 1 is fixed. The positions of mirrors 2, 3 and 4 can be individually varied by manual translation stages (9065-X-M, New Focus/Newport) so that the pulses are accordingly delayed in time. The travel range of 14 mm corresponds to a temporal regime of about 90 ps where time and distance are related via the speed of light: $\Delta t = 2\,\Delta x/c$. The factor of 2 accounts for the fact that the laser beams hit the mirrors under normal incidence and therefore a position change of a mirror yields a change of the optical path twice as large.

In addition, mirrors 3 and 4 are each mounted on piezo stages (PIHera Piezo Linear stage P-622.1CD, Physik Instrumente). Thus, these two mirrors can be moved over a range of 260 µm with high resolution ($<$1 nm), providing a temporal range of approximately 1.7 ps. Thus, various combinations of time-delays between the four beams can be selected and scanned.

The two or four beams, respectively, are obtained from the main laser beam by two masks. Such a mask consists of four mini-irises (ID5MS/M, Thorlabs). A photography is displayed in Fig. 3.6. The four holes of the mask are located at the corners of a square. When the incident laser beam hits the mask, four beams are cut out. These beams pass the second mask before each single beam hits one mirror of the four-split mirror. The square arrangement of the beams is also called box geometry. The application of two such masks enables the independent adjustment of the intensity (by mask 1) and the size of one single beam (mask 2). In experiments using the 30 fs laser pulses, the distance between the two masks amounts to $\sim$2.3 m. When the 7 fs short pulses are utilized, the distance is about 2.1 m. The distances are chosen such that the four beams can still pass the second mask (if the distance was too large, the divergence of the laser beam would make the spatial separation too large and thus cause a blocking of the beams at the second mask), but the diffraction caused by the first mask must be strong enough to illuminate the second set of holes as completely as possible. By blocking one or more beams directly after the second mask, the desired number of laser pulses can be chosen. In the transient-absorption measurements, only the two beams hitting mirrors 3 and 4 are used. They serve as pump and probe beam. Neutral-density filters of variable optical density can be inserted to finely adjust the intensities of the different beams.

The beams are then focused by a spherical mirror (R = 1000 mm, f = 500 mm). The sample that shall be studied is inserted in the focus. The transmitted beams are then collimated, the probe beam is selected and detected by a spectrometer (USB2000+, Ocean Optics). In order to collect all intensity, the probe beam is focused into a fiber (QP-200-2-UV-VIS, Ocean Optics). Since it is a multimode fiber, the light is coupled into it in various modes interfering at the detector so that the measured spectrum is modulated. Therefore, a self-built diffusor (in principle a rotating paper disk) is added directly in front of the fiber input to scatter the light and to average out the interferences.

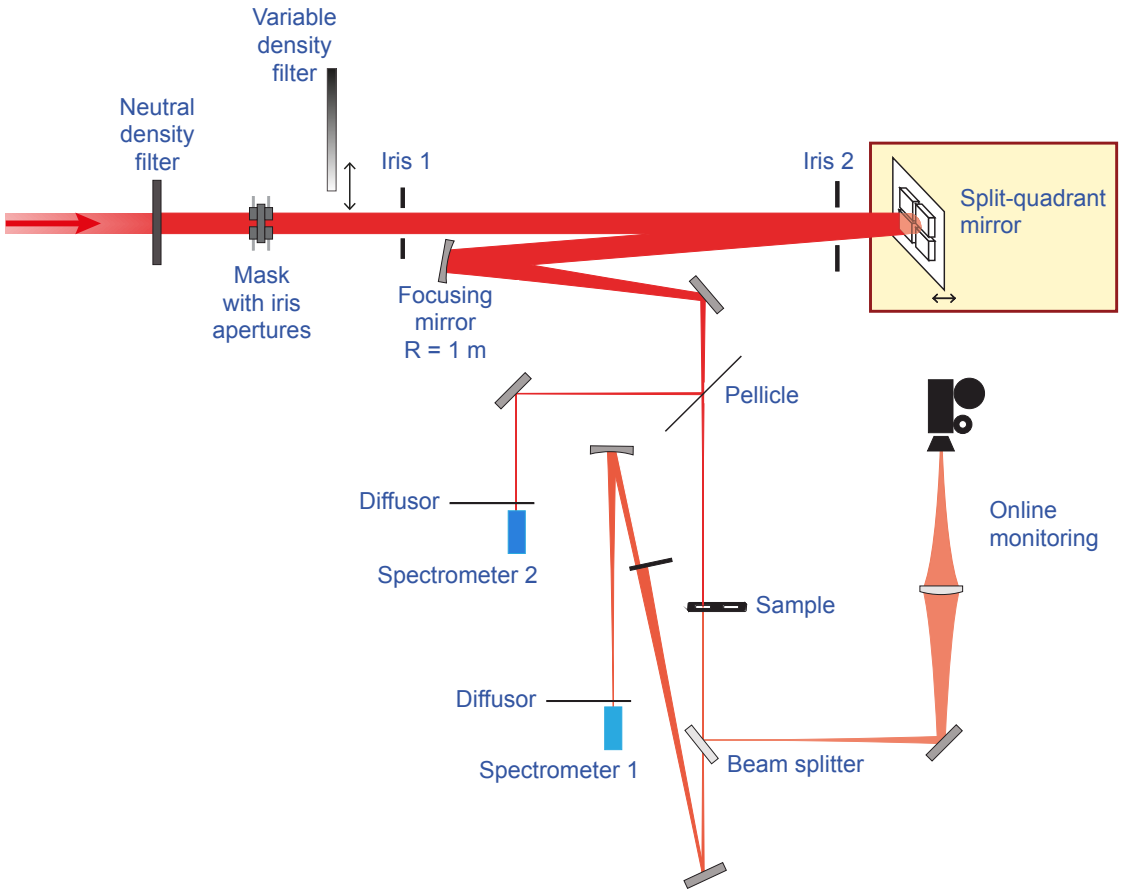

Figure 3.4: Schematic drawing of the transient-absorption/2D-spectroscopy setup. Two masks (only one is depicted) cut out up to four beams of the incident laser beam. Each beam hits one of the segments of the four-split mirror and can be independently delayed in time. The beams are focused by a spherical mirror ($f = 500$ mm) onto the sample and the transmitted probe pulse is detected. The online monitoring section allows to check the temporal and spatial overlap of the pulses at the focus. In order to record the laser spectrum, a small portion of the beams is reflected by a pellicle and measured by a second spectrometer. The neutral and variable density filters enable the fine adjustment of the beams' intensities. Irises 1 and 2 serve as marks for the beam position so that an easy change between the 30 fs (directly out of the laser) and 7 fs (after hollow-fiber compression) short pulses is possible.

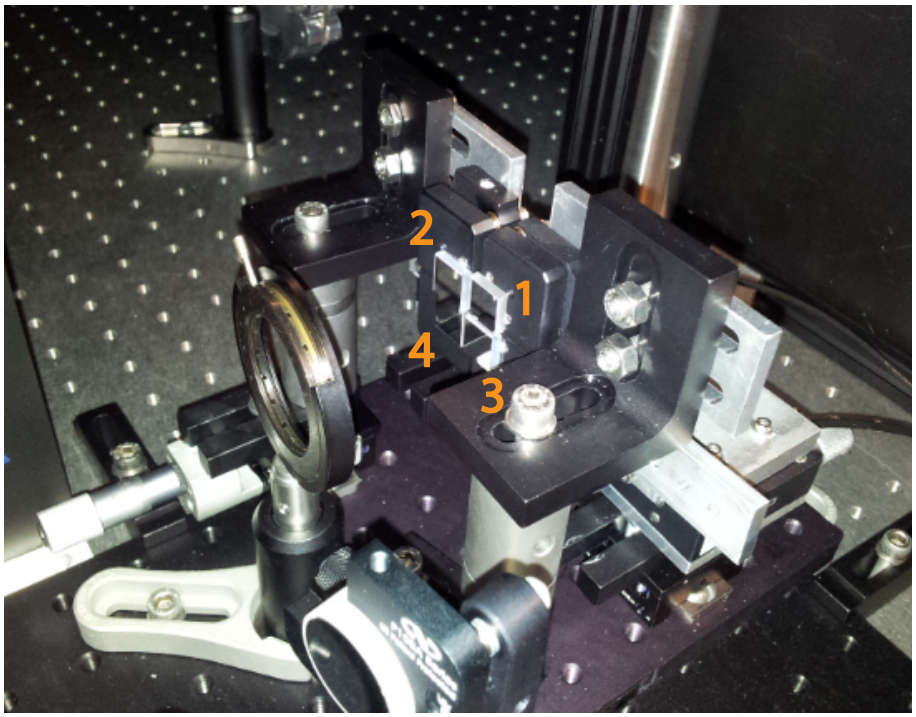

Figure 3.5: Four-split mirror. Four square silver mirrors, each attached to a kinematic mirror mount, allow the individual alignment and delay in time of each laser beam. The four segments of the mirror assembly are numbered as used in the text.

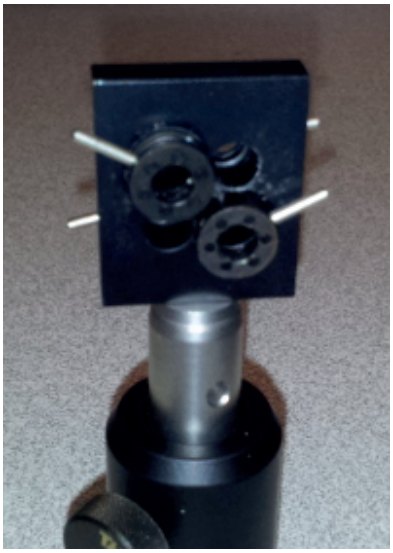

Figure 3.6: Four-hole mask. Four mini-irises are glued to a mask that is used to cut out the four sub-beams from the incident laser beam.

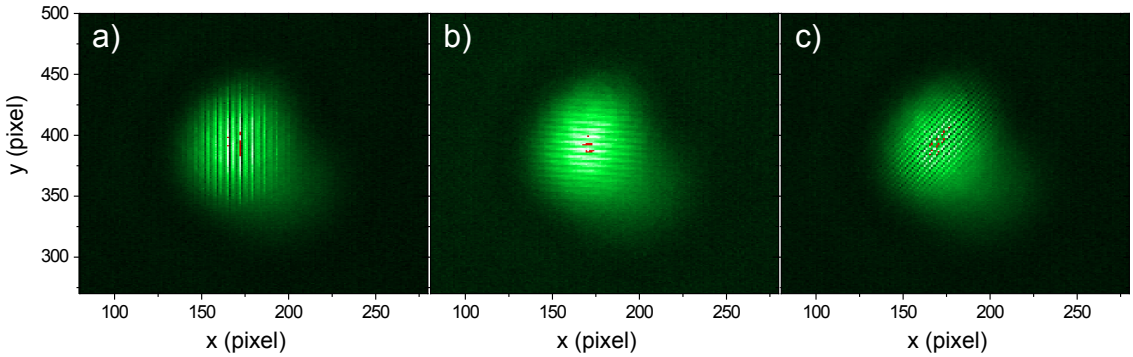

Figure 3.7: Temporal overlap at the focus. These interference patterns are the indication for the overlap of a pair of beams in time. Depending on the geometric arrangement of the two beams, the orientation of the interference fringes is different: (a) two horizontally (e.g. from mirrors 3 and 4), (b) vertically (e.g. from mirrors 1 and 3) or (c) diagonally interfering (e.g. from mirrors 1 and 4) beams.

In the focus where the sample is located, the four beams have to overlap spatially and temporally. The spatial and temporal overlap can be checked by placing a CMOS (complementary metal-oxide-semiconductor) camera (by Conrad Electronic) into the focus. For fine tuning, the spatial overlap can be optimized with each mirror mount of the four-split mirror separately. The temporal overlap can be achieved by moving the piezo stage of one mirror until interference fringes appear. The exact assignment of the time zero overlap can be carried out directly in the experiment by looking at characteristic features like the coherent artefact or by recording the second-harmonic light produced by a BBO crystal and determining its intensity maximum.
In order to monitor the spatial and temporal overlap during the measurements as well, a beam splitter reflects off a portion of the beams after the sample. These reflected beams are again focused onto a CMOS camera. Thereby, any changes in the alignment could be noticed in the course of an experiment. Some interference patterns appearing when the pulses overlap in time are exemplarily depicted in Fig. 3.7.
When scanning the time delay between the pulses, we want to monitor the laser spectrum for each piezo step. For this purpose a 2" large and extremely thin pellicle made of nitrocellulose (by National Photocolor) is inserted before the laser beams pass the sample. A small part of the beams is reflected off the pellicle and the laser spectrum is detected by a second spetrometer (USB4000, Ocean Optics). Due to the pellicle thickness of only 2 µm, no noteworthy dispersion is induced, neither for the 30 fs nor the 7 fs short pulses. As target a solution of the dye IR144 in methanol is inserted for the transient-absorption experiments discussed in chapters 4.2 and 5.3. The liquid is filled into a cuvette (SpecVette CSV-500, Ocean Optics) with 500 µm path length. For exact positioning of the sample in the beam focus, the position can be adjusted precisely by a translation stage (9064-X-M, New Focus/Newport).

This setup provides excellent stability, which has already been demonstrated in a proof-of-principle 2D-spectroscopy measurement [2]. The entire setup is based on reflective optics. No diffractive optics, pulse-shaping devices or feedback loops are required for the creation of a set of up to four beams and introducing the time delays. The all-reflective

configuration exhibits a high phase stability [2], but is offering an easy alignment at the same time. Furthermore, the setup is very flexible as it allows the use of ultra-broadband light in various wavelength regimes. It is not only suitable for the visible or infrared range, but can be adapted to the UV or even X-ray range if multilayer mirrors or a grazing incidence geometry, for instance, are chosen. Hence, such a setup could also be implemented for the realization of 2D-spectroscopy experiments at XUV/X-ray Free-Electron Laser sources.

3.3.2 Pulse shaper

In this section the pulse shaper which was designed and set up in the course of this thesis is introduced. At first, the setup is described and the working principle is explained giving examples how specific phases imprinted on the spectral components shape the laser pulses. The experimental control is also discussed. The last section deals with the pulse characterization method "multiphoton intrapulse interference phase scan" which is based on a pulse shaper.

Pulse shaper setup

The key optical component of the pulse shaper is the spatial light modulator (SLM-S320) by Jenoptik. It consists of a liquid-crystal display (LCD). Such a modulator can vary the phase and/or the amplitude of the different spectral components of a light pulse and hence the shape of the laser pulse can be modified in the desired way. The principle of shaping pulses is explained in the subsequent section. In order to get access to the spectral components of a laser pulse, an optical Fourier transform needs to be performed. This is simply realized by diffractive optics like prisms or gratings. In a typical pulse shaper setup the laser pulse is dispersed by a grating. A focusing lens or mirror focuses each spectral component to a spot in the Fourier plane where the modulator is placed. After the Fourier plane the setup has a mirror symmetry: the spectral components are collimated again before they hit a second grating where they are recombined to the (now shaped) laser pulse. The distance from grating to focusing element and from focusing element to the LCD is the focal length f. Therefore, such a geomtery is called $4f$-configuration. A schematic illustration is shown in Fig. 3.8.

The design of our pulse shaper setup follows the geometry described by Präkelt et al. [83]. Figure 3.9 presents a sketch and Fig. 3.10 a picture of the setup. Grating, cylindric mirror and folding mirror are aligned in one row at each side of the modulator so that the cylindric mirrors are not tilted in the sagittal plane compared to the incident laser beam in order to avoid aberrations. All mirrors are set up at the same height to keep the laser light at a constant level before and after the modulator. Only the gratings are vertically shifted upwards. Periscopes are inserted to guide the laser beam to the higher level of the grating and back down to the original beam height, respectively. However, the vertical angle at the gratings is kept at a minimum. The cylindric and planar (folding) mirrors are manufactured by Laser Components and are silver coated. The focal length of the cylindric mirrors is $f = 200$ mm. Blazed holographic plane gratings (by Horiba Jobin Yvon

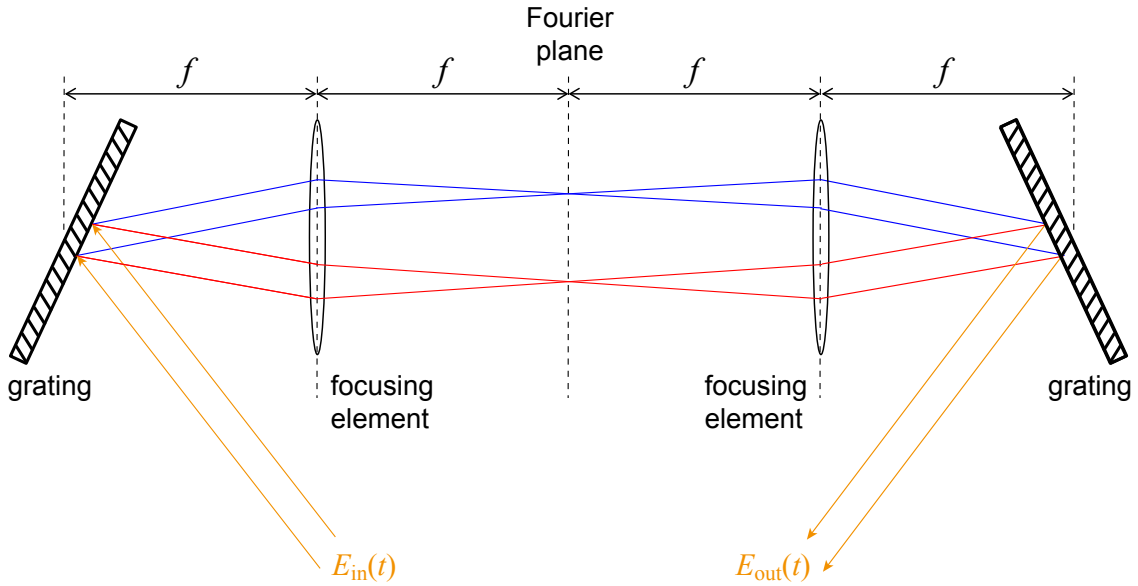

Figure 3.8: Schematic representation of a pulse shaper in $4f$-configuration (based on [82]). The distance in between the necessary optical components (two gratings and two focusing elements like lenses or mirrors) and the Fourier plane is the focal length f. The pulse shaper setup has a mirror symmetry at the Fourier plane onto which the spectral components of the incident laser pulses are focused.

GmbH) with a size of 44 mm x 44 mm are used. The gratings are aluminum coated, a groove density of 1200 l/mm was chosen and the blaze wavelength is 630 nm.

The alignment of all optical components is crucial. The orientation of each element and the distances in between (which has to be the focal length f of the cylindric mirrors) need to be adjusted carefully. Any improper alignment can lead to astigmatism, i.e. the foci in the horizontal and vertical plane do not coincide, and other aberration effects and spatial chirp, i.e. different colors propagating differently in space, which must be avoided. Therefore, both gratings and both cylindric mirrors are mounted on high-stability translation stages (M-462-X-M and M-462-X-SD, Newport) which allow to shift each optical component by 25 mm in the horizontal plane. Furthermore, gratings and cylindric mirrors can be rotated around the axis perpendicular to their surface, i.e. in the mirror or grating plane, respectively. When setting up the optical components, the laser beam is focused after the pulse shaper setup and the focus is checked using a CMOS camera. At first, the cylindric mirrors are inserted, with the gratings set to zeroth order. Their rotation is adjusted so that the focusing plane is horizontal and the astigmatism of the focus is removed. In the same way the distance between the two cylindric mirrors is tuned.
The rotation of the gratings is optimized by checking that the spectral components lie on a horizontal line in the Fourier plane. If the distance between grating and cylindric mirror is not correct, the different spectral components are not focused onto the same spot on the CMOS camera. Therefore, the position of the gratings must be finetuned in order to minimize the spatial chirp.
The distance between the gratings and the cylindric mirrors has an influence on the group delay imprinted on the laser pulses as well (cf. [84]). If the distance is larger (smaller) than

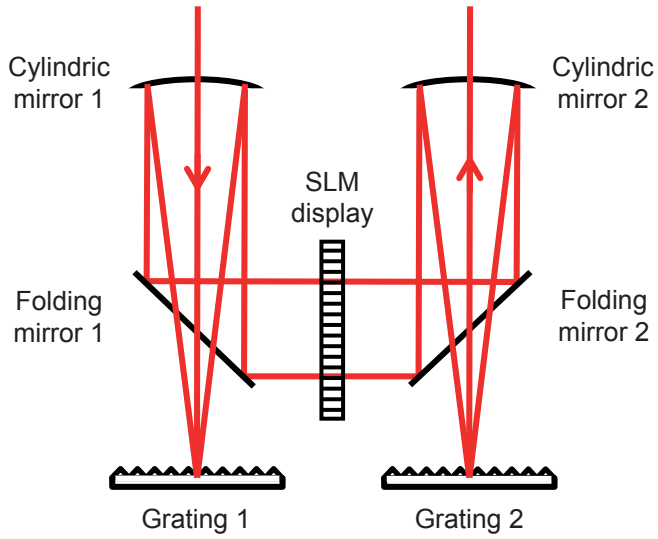

Figure 3.9: Sketch of the pulse shaper setup. The geometry is chosen according to the setup described in [83]. It is a compact setup avoiding aberrations that would be caused in a non-linear arrangement of the optical elements due to a horizontal tilt of the cylindric mirrors.

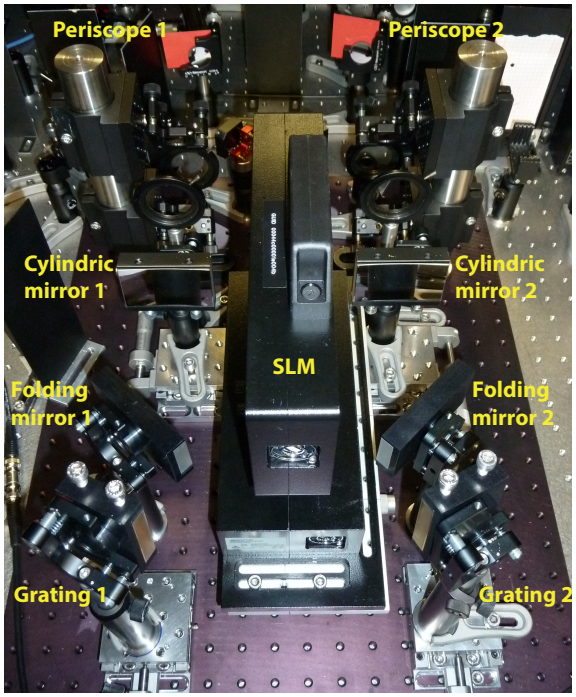

Figure 3.10: Picture of the pulse shaper setup with the spatial light modulator at its center.

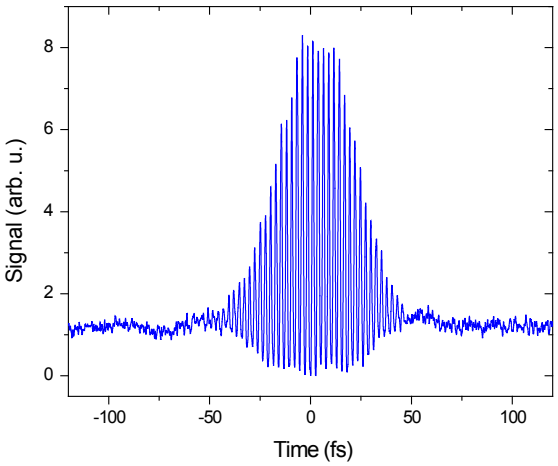

Figure 3.11: Measured interferometric autocorrelation of the laser pulses after propagation through the optimized pulse shaper setup. The signal reveals a pulse duration of about 26 fs indicating an optimal alignment of the pulse shaper and compensation of dispersion.

f, negative (positive) dispersion will be induced. However, due to the LCD, the dispersive optical elements and the additional air path through which the laser pulses propagate, a large phase is added to the spectral components of the pulses and the pulse length is increased. To compensate for this effect, the position of the gratings can be utilized as control knob.
Finally, the spatial light modulator can also be moved horizontally along and perpendicularly to the beam path by two crossed stages (M-423, Newport). It enables to exactly position the LCD in the Fourier plane and to illuminate the display in a centered way.
After optimizing the pulse shaper setup, an autocorrelation measurement was performed to check the pulse durations (see Fig. 3.11). The signal corresponds to a pulse duration of roughly 26 fs revealing an optimal alignment of the pulse shaper since no pulse stretching seems to occur due to uncompensated dispersion.

The entire setup features a very high stability. Even after four months of break caused by a downtime of the laser system, the alignment was still perfect.
The described setup of the pulse shaper is designed for shaping the 30 fs pulses that are directly obtained from the Ti:Sa laser system. The pulse shaper could be adapted to the shorter 7 fs pulses by exchanging the gratings. Only the groove density has to be chosen in a way that the resulting spatial splitting of the spectral components fits to the width of the SLM display.
The pulse shaper is located directly next to the transient-absorption setup that was introduced in the previous section 3.3.1. By flipping two mirrors into the beam path, the laser pulses can be shaped before they enter the spectroscopy section of the experiment.

Shaping pulses

The shaping of laser pulses is based on modulating the phases and/or amplitudes of the different spectral components of the laser pulse (cf. chapter 2.1). This can be done in the Fourier plane by blocking or attenuating particular frequencies with light shades, slits

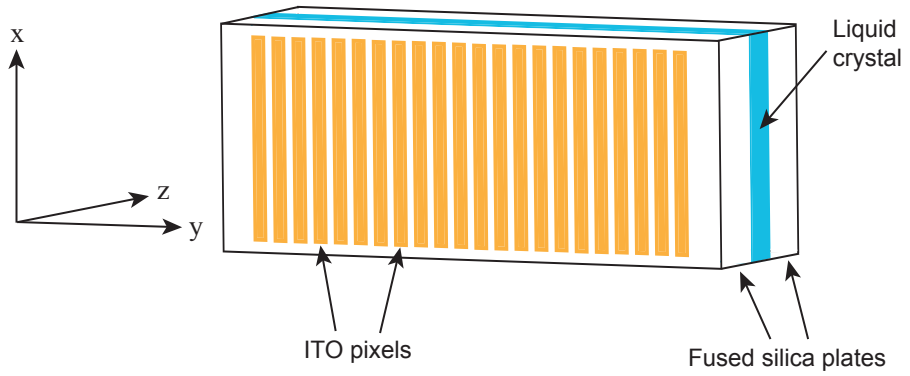

Figure 3.12: Sketch of the liquid crystal display of the spatial light modulator (based on [85]). The liquid crystal is sandwiched between two fused silica plates that are coated with indium tin oxide (ITO). The coating of one plate plate is structured into 320 pixels. The coordinate system indicates the defined directions: The z-axis corresponds to the propagation direction of the laser beam. The optical axis of the liquid crystal lies in y-direction. The pixels are oriented along the x-axis.

or apertures or by delaying them using transparent materials with different refractive indices. Typically, liquid-crystal spatial light modulators are utilized and allow a computer controlled shaping with high precision. Such a commercially available display usually consists of 120 to 640 pixels. By applying a voltage, the refractive index can be varied. Another option are acousto-optic modulators. An overview of the various pulse-shaping techniques and the principles can be be found in [47, 85] among other works.
The spatial light modulator SLM-S320 from Jenoptik features a liquid-crystal display with a width of 31.9 mm and a height of 13 mm. It is divided into 320 pixels [82]. The display is built up by two glass plates with a nematic liquid-crystal layer in between. Both glass substrates are coated with transparent and electrically conducting indium tin oxide (ITO). One of them is structured into an array of pixels. A schematic of an LCD is shown in Fig. 3.12. Without any voltage applied, the rod-shaped molecules are oriented along their predominant direction as it is depicted in Fig. 3.13(a) and the liquid crystal is optically birefringent. The predominant direction of the molecules defines the optical axis. The refractive index is larger for laser light which is polarized along the y-axis, i.e. parallel to the molecular orientation, (extraordinary ray) than for perpendicularly x-polarized light (ordinary ray). If a voltage is applied, the molecules are tilted along the z-axis which corresponds to the direction of the electric field (cf. Fig3.13(b)). The higher the electric field, the smaller the angle gets between optical axis and propagation direction of the light. The refractive index for the x-polarized light remains unchanged, whereas it decreases for the polarization component parallel to the optical axis. Thus, the phase of the y-polarized laser light transmitted through the display can be changed by controlling the applied voltage.

With a single display either amplitude or phase modulation can be performed. Amplitude modulation is obtained when the optical axis of the liquid crystal and the polarization direction of the incident light are rotated by 45°. The LCD acts as a waveplate, i.e. modifying the polarization state due to an induced phase shift. The amplitude can then be modulated by a subsequent polarization filter which only can be passed by light that is

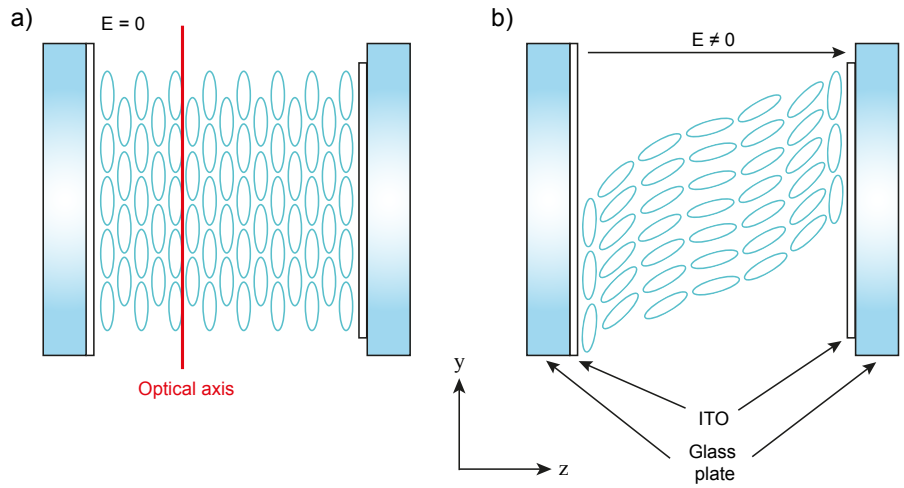

Figure 3.13: Schematic illustration of the molecules and their orientation in the liquid crystal without (a) and with (b) an external electric field applied by a voltage difference between the two ITO electrodes. Based on [82, 85].

polarized in a certain direction. For the combination of both phase and amplitude shaping, the SLM has to consist of two LCDs. In our case, the SLM is equipped with one LCD and we perform phase-only pulse shaping in the experiments.
As already explained in chapter 2.1, neither a constant phase offset nor a linear phase have an impact on the pulse shape (pulse envelope). A constant phase only changes the carrier-to-envelope offset, but the pulse remains bandwidth limited. A linear phase induces a shift in time. Therefore, higher-order phase changes are required to modify the pulse shape. For example, a sinusoidal phase pattern with frequency ω_s leads to a splitting into subpulses: A pulse train is created with a temporal spacing $\Delta t = 2\pi/\omega_s$ (cf. [86]) between the subpulses.

As already mentioned, the phases of the spectral components can be shifted by varying the voltage that is applied to the pixels of the SLM display. The control of the LCD is realized using LabView programs that were specifically written for the desired application. A program code to control the phase-pattern setting on the pulse shaper is exemplarily shown in the appendix A.2. Before any phase pattern is written onto the display, the SLM needs to be calibrated. The calibration includes the attribution of each pixel to the spectral component hitting the pixel and the assignment of the voltage to the induced phase shift. The procedure is explained in detail in the appendix A.1.
Now with the calibration at hand, any favoured phase pattern can be applied to the LC-display. To test the functionality of the pulse shaper in the experiment, sinusoidal phase patterns are imprinted on the spectral components of the 30 fs laser pulses. The influence on the pulse shape is checked by measuring the autocorrelation (AC) signal of the laser pulses. As it is explained in chapter 2.2, the autocorrelation alone provides only limited information about the exact pulse shape. However, a comparison to a simulation of the autocorrelation signal gives a better insight. In the simulation, the laser spectrum is mimicked by a Gaussian distribution with a center wavelength of about 780 nm and a pulse length of $\sim$26 fs. Sinusoidal phase patterns are applied to generate pulse trains. The case of a flat phase is also tested. The detected and calculated AC signals are shown in Fig. 3.14

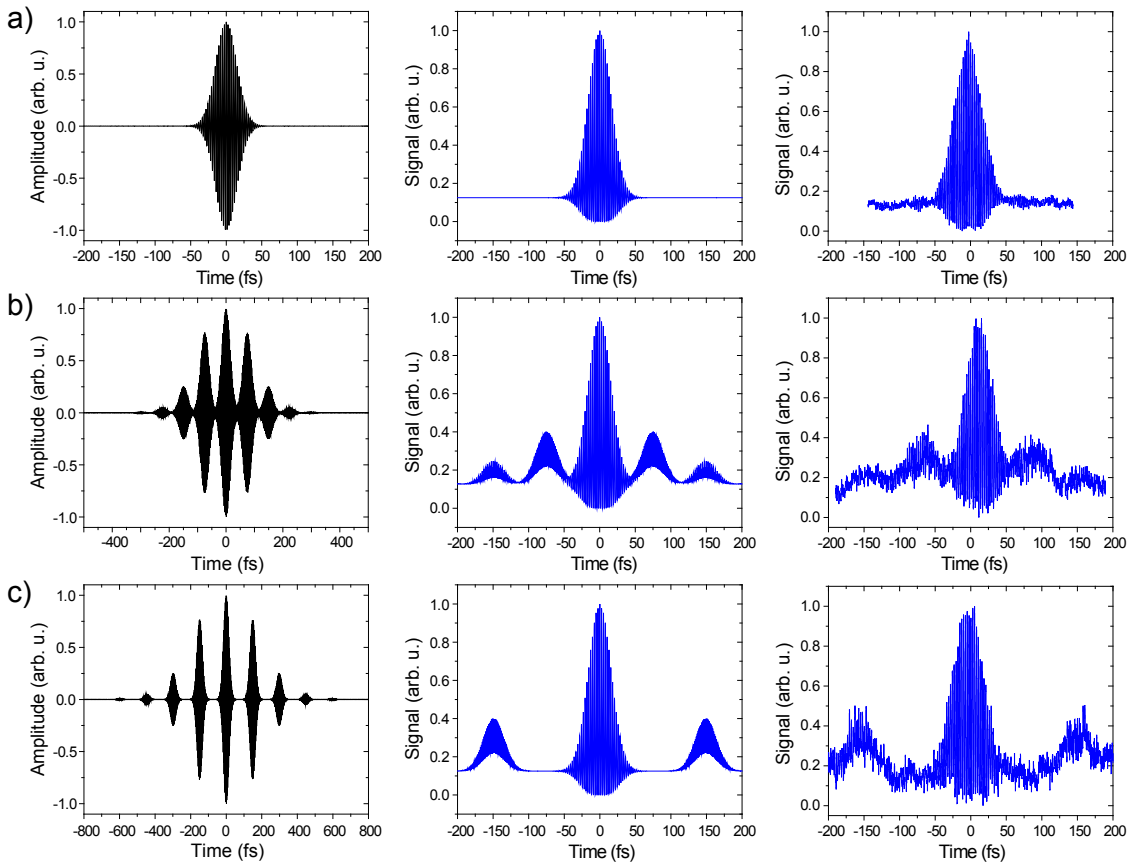

Figure 3.14: Interferometric autocorrelations of the shaped laser pulses for different phase patterns applied to the SLM display. From left to right are presented: the expected pulse shape, the calculated AC signal and the measured AC signal, (a) for a flat phase, (b) for a pulse train with a temporal spacing of 75 fs between the subpulses and (c) for a pulse train with twice the temporal spacing, i.e. 150 fs. The temporal spacing of the subpulses appears also in the autocorrelation signals determining the position of the sidelobes in the AC graph.

besides the simulated expected pulse shape. The cases for two pulse trains with different temporal subspacings are displayed (cf. Fig. 3.14(b) and (c)). Both, measurement and simulation, are in excellent agreement.

Pulse characterization: Multiphoton Intrapulse Interference Phase Scan

The possibility to shape laser pulses has paved the way towards quantum control. By tailoring the amplitude and phase of laser pulses a large variety of experiments were carried out, for instance controlling the two-photon absorption in atoms like cesium [87] or in molecules. The latter included not only small, but even large and complex systems like dyes or proteins [88]. In these experiments, the interference of two or more photons leading to a multiphoton transition (also termed multiphoton intrapulse interference) and the control of the process' probability by shaping the spectral phases was demonstrated.

It was the Dantus group that inverted the effect and developed the multiphoton intrapulse interference phase scan (MIIPS) method to characterize laser pulses (see e.g. [89–92]).

The method exploits the well-understood non-resonant second-harmonic generation (SHG) process. It reconstructs the phase of the laser pulses on the basis of the SHG probability. As explained at the end of chapter 2.3, the probability is proportional to equation (2.34) and it depends on the spectral phase $\varphi(\omega)$ of the laser pulses. The key idea of MIIPS is to introduce a reference phase $f(\omega)$ using the pulse shaper and to compensate the unknown intrinsic phase of the laser pulses. If the corresponding compensating phase is determined for each spectral component, the entire spectral phase is obtained.

As already mentioned, a pulse shaper is required to identify the spectral phase. Since the pulse shaper was already commissioned in our laboratory (cf. section 3.3.2), the decision in favour of MIIPS instead of another characterization method was taken. The MIIPS technique was implemented in the course of a Bachelor thesis under my supervision as part of this thesis [93].
After the pulse shaper the laser light is converted into second-harmonic light by a frequency doubling crystal. In our case, a 100 µm thick BBO crystal is used. The intensity of the frequency-doubled light is detected by a spectrometer (USB4000, Ocean Optics). As it is given by equation (2.34), the intensity is maximized for Fourier-limited pulses, i.e. $\varphi(\omega) = 0$ for each spectral component. The phases at negative and positive detuning of equation (2.34) can be expanded into a Taylor series around ω

$$\varphi(\omega \pm \Omega) = \varphi(\omega) \pm \varphi'(\omega)\,\Omega + \frac{1}{2}\,\varphi''(\omega)\,\Omega^2 + \mathscr{O}(\Omega^3), \tag{3.3}$$

where $\varphi^{n'}(\omega)$ is the nth derivative. The sum is given by

$$\varphi(\omega+\Omega) + \varphi(\omega-\Omega) = 2\,\varphi(\omega) + \varphi''(\omega)\,\Omega^2 + \ldots + \frac{2}{2n}\,\varphi^{2n'}(\omega)\,\Omega^{2n}. \tag{3.4}$$

Thus, the intensity of the SHG light can be written as (if higher orders are neglected)

$$I(2\omega) \propto \left| \int d\Omega \left|\widetilde{E}(\omega+\Omega)\right| \left|\widetilde{E}(\omega-\Omega)\right| e^{i2\varphi(\omega)}\, e^{i\varphi''(\omega)\,\Omega^2} \right|^2. \tag{3.5}$$

Therefore, the intensity of the second-harmonic spectrum at a given frequency ω is maximum if

$$\varphi''(\omega) = 0. \tag{3.6}$$

The phase imprinted on the laser pulses in such a MIIPS measurement is

$$\varphi(\omega) = f(\omega) + \phi(\omega), \tag{3.7}$$

where $\phi(\omega)$ represents the intrinsic spectral phase that has to be found out. The condition (3.6) for maximum SHG intensity is fulfilled, if

$$\phi''(\omega) = -f''(\omega). \tag{3.8}$$

Hence, the unknown intrinsic spectral phase of the laser pulses can be reconstructed by the reference phase $f(\omega)$ and the determination of its second derivative. As reference phase a sinusoidal function is typically chosen [89, 90]:

$$f(\omega, \delta) = \alpha \sin(\gamma\omega - \delta). \tag{3.9}$$

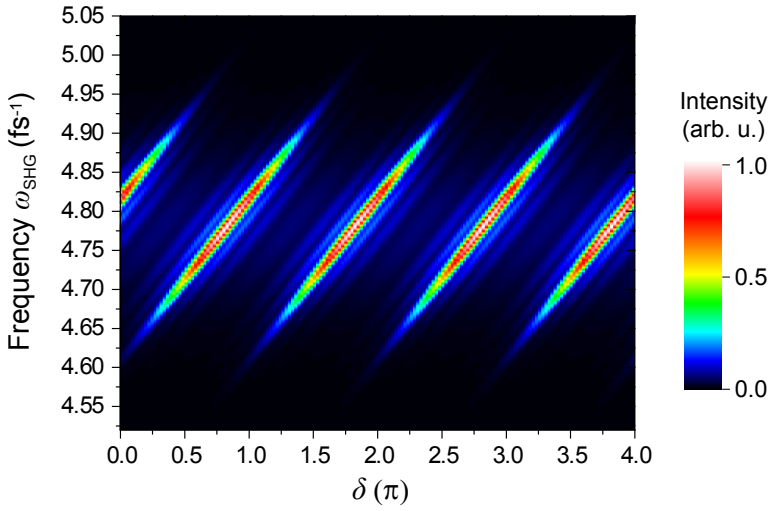

Figure 3.15: A typical two-dimensional MIIPS spectrum showing the second-harmonic light as a function of the parameter δ (simulation result). The intensity of the SHG spectrum peaks at a specific $\delta_{\max}$ for a given spectral component ω_{i}. In the case of a bandwidth-limited pulse as presented here, the maxima form parallel lines shifted by π as explained in the text.

α and γ are free parameters that can be adapted, but typically $\alpha = 1.5\,\pi$ and γ reflects the pulse duration [90]. The parameter δ is varied from 0 to 4π so that the second derivative of the reference phase covers the full phase range $[0, 2\pi]$ for each spectral component.

The principle scheme of the MIIPS is explained in the following: In the first step, the reference function $f(\omega, \delta)$ is applied to the pulse shaper. The parameter δ is scanned from 0 to 4π and for each δ-value an SHG spectrum is detected. Figure 3.15 shows a typical (simulated) MIIPS graph. The SHG spectra (corresponding to a vertical cut) as a function of δ are typically displayed in such a two-dimensional plot.
As second step, for each spectral component ω_{i} the value $\delta_{\max}(\omega_{\mathrm{i}})$ is determined for which the SHG intensity is maximized. The given example in Fig. 3.15 presents the case of ~ 26 fs short Fourier-limited pulses with $\phi(\omega) = \phi''(\omega) = 0$ and a central wavelength of about 780 nm. With the given reference function (3.9), the result is $\delta = \gamma\,\omega \pm n\,\pi$ ($n \in \mathbb{N}$). This means that the SHG maxima form lines with a slope γ. The lines are shifted by π along the δ-axis. In case of a quadratic phase the lines are not equidistant anymore, whereas for a cubic phase the shift is unchanged, but the lines are tilted. Thereby, an estimation of the type of intrinsic spectral phase from the shape of the measured SHG spectra is possible. More details can be found in [93].
As third step, the second derivative of the unknown intrinsic phase can be calculated for each frequency component taking equations (3.8) and (3.9) into account:

$$\phi''(\omega_{\mathrm{i}}) = -f''(\omega_{\mathrm{i}}) = \alpha\,\gamma^2 \sin\left(\gamma\omega_{\mathrm{i}} - \delta_{\max}(\omega_{\mathrm{i}})\right). \tag{3.10}$$

The original phase $\phi(\omega)$ is obtained by double integration:

$$\phi(\omega_{\mathrm{i}}) = -\alpha \sin\left(\gamma\omega_{\mathrm{i}} - \delta_{\max}(\omega_{\mathrm{i}})\right) + \tau_g\,\omega + \phi_0, \tag{3.11}$$

where two integration constants τ_g and ϕ_0 are required which are not known. ϕ_0 corresponds to the carrier envelope phase (CEP) and the linear contribution τ_g to a shift in time (cf. chapter 2.1).

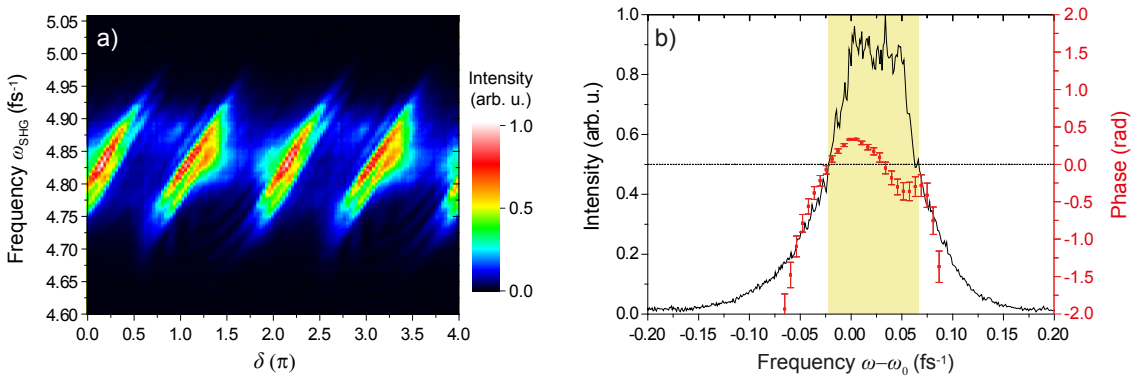

Figure 3.16: Determination of the intrinsic spectral phase of the 30 fs laser pulses. (a) 2D MIIPS scan of the first iteration step. (b) Obtained residual phase after three iteration steps. An average over three measurements is taken. For orientation, the laser spectrum (black curve) is also displayed. The frequency axis is centered around $\omega_0 = 2.416$ fs^{-1}. The shaded area indicates the frequency range of the FWHM which is used for reconstructing the laser pulse in the time domain (cf. Fig. 3.17). Figure (b) adapted from [93].

In order to improve the accuracy of this phase characterization, the method can be carried out iteratively. The phase $\phi^{(1)}(\omega)$ measured in the first iteration step is subtracted by the pulse shaper. Therefore, only deviations from the determined phase are detected in the second iteration step and contribute to $\phi^{(2)}(\omega)$. In the third iteration step, $\phi^{(1)}(\omega) + \phi^{(2)}(\omega)$ are subtracted and the scan is repeated yielding the phase correction $\phi^{(3)}(\omega)$. This procedure can be repeated over and over until the desired level of accuracy is reached. The total measured intrinsic spectral phase after n iteration steps is given by the sum of all corrective phases

$$\phi(\omega) = \phi^{(1)}(\omega) + \phi^{(2)}(\omega) + ... + \phi^{(n)}(\omega). \tag{3.12}$$

In principle, the intrinsic phase of a laser pulse can be determined with extremely high accuracy. However, as derived in chapter 2.1, a constant or linear phase does not have any impact on the intensity distribution of the laser pulses. Therefore, such phase contributions do not influence the second-harmonic spectrum and cannot be identified by the MIIPS method.

More information about the presented technique, the role of the parameters α and γ, other possible reference functions and the numerical and experimental results are contained in [93]. There, the software for the simulation, the experimental control and phase reconstruction implemented in LabView are discussed as well.

In order to demonstrate the operation of the MIIPS method, two cases are exemplarily shown: (i) the measurement of the intrinsic phase of the 30 fs pulses and (ii) the determination of an additionally imprinted phase.
The first application of MIIPS is to identify the intrinsic phase of the 30 fs laser pulses provided by the Femtolasers system. The pulses should be transform-limited, but the dispersion compensation might not be perfect and the air and other dispersive optical components in the beam path may cause a residual phase. The MIIPS was performed three times with three iteration steps each. Figure 3.16(a) displays one scan of detected SHG light as function of the parameter δ as example. The finally obtained averaged phase is presented

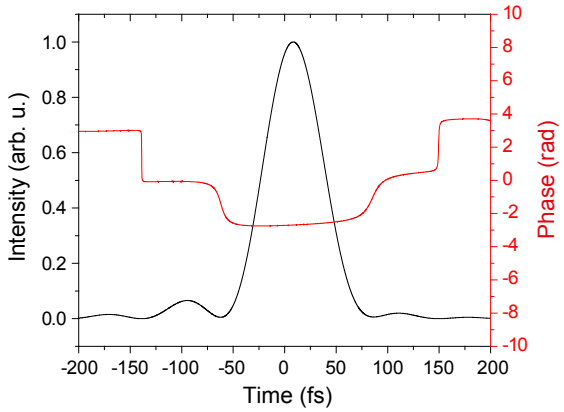

Figure 3.17: Reconstructed pulse in the time domain. From the measured spectrum and phase shown in Fig. 3.16(b), the intensity distribution of the laser pulse in the time domain is derived by Fourier transform (black curve). The temporal phase (red curve) is obtained by subtracting the linear contribution $\propto \omega_0 \cdot t$ which is determined by the central frequency ω_0 (cf. equation (2.12)). As slope of the linear fit a value of 2.436 fs^{-1} is found, excellently corresponding to ω_0.

in Fig. 3.16(b). Obviously, the laser pulses exhibit a residual phase in the range of 1 rad. The reproducibility of the method is very good in the frequency range of the FWHM of the spectrum. The reconstructed pulse in the time domain is shown in Fig. 3.17. It is obtained by the Fourier transform of the spectrum and phase in the FWHM range (shaded area in Fig. 3.16(b)).
In a further measurement, an additional phase was imprinted on the laser pulses by the pulse shaper, namely

$$\phi(\omega) = 1000\,\text{fs}^3\ (\omega-\omega_0)^3 + 500\,\text{fs}^3\ (\omega-\omega_0)^2 \tag{3.13}$$

with the central frequency $\omega_0 = 2.416\ \text{fs}^{-1}$. This corresponds approximately to the dispersion induced by a 2.5 mm thick plate of fused silica. Figure 3.18(a) illustrates the 2D MIIPS scan of the first iteration step. The measured corrective phases $\phi^{(i)}$ of each of the four iteration steps are shown in Fig. 3.18(b) - (e). It becomes directly apparent that the corrective phases converge more and more to zero. The finally determined phases after one and four iteration steps, respectively, are plotted in Fig. 3.18(f). The obtained phase after four iterations reproduces the added phase in the range $[\omega_0 - 0.05\ \text{fs}^{-1},\ \omega_0]$. In the range $[\omega_0,\ \omega_0 + 0.05\ \text{fs}^{-1}]$ it deviates, however, it resembles the intrinsic spectral phase in Fig. 3.16(b) and can be attributed to it. In general, the reliability of the MIIPS method is limited by spectral chirp and similar effects.

As a last remark, it has to be noted that the presented technique is not only suitable for characterizing laser pulses. Since the spectral phase is determined, the already available pulse shaper can compensate for it and produce bandwidth-limited pulses. Moreover, the technique can be used to determine the group-velocity dispersion of materials. For instance, the Dantus group measured the GVD of water, seawater and components of cow eyes with high precision [94] and investigated the second- and third-order dispersion of atmospheric gases [95].

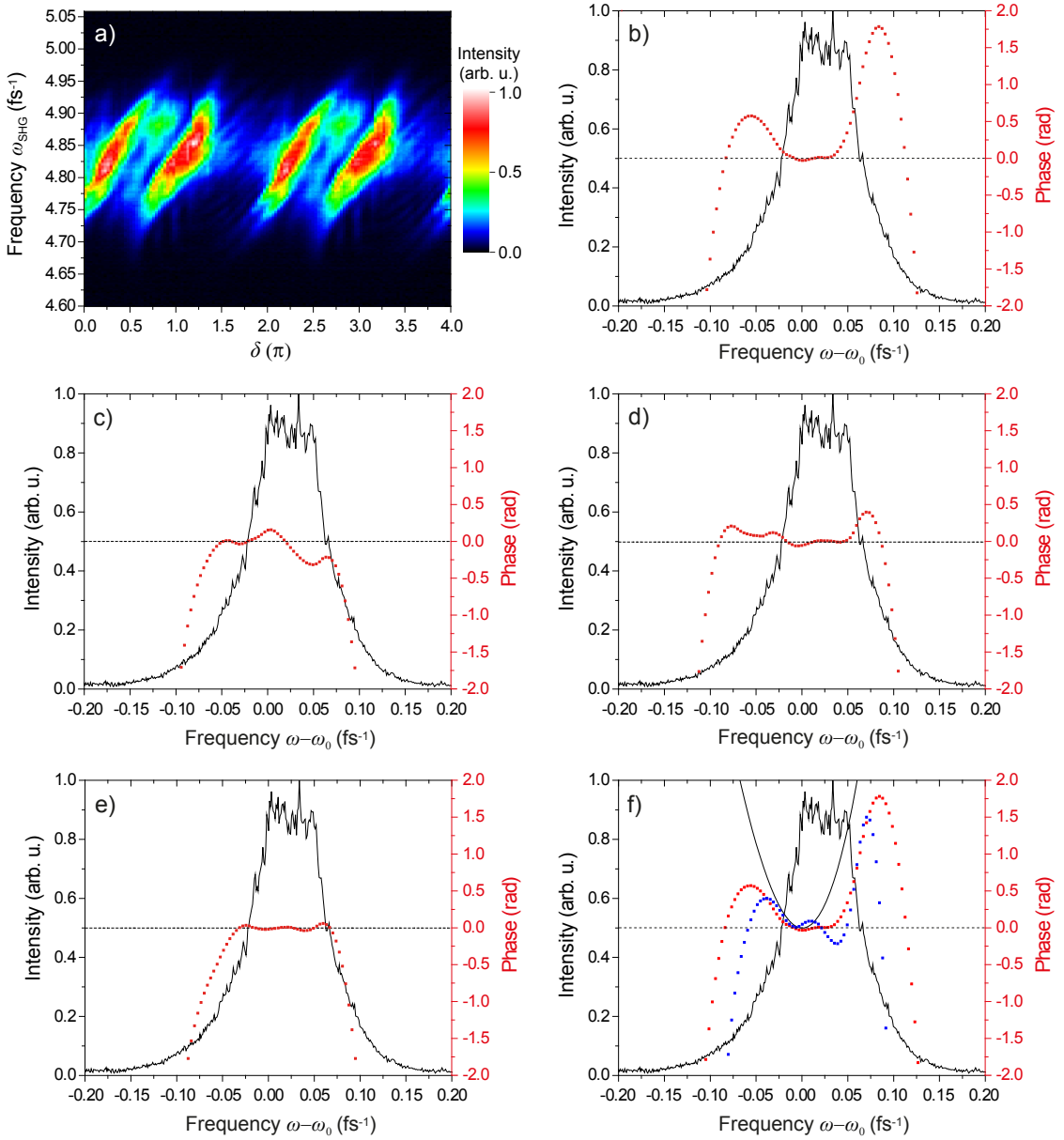

Figure 3.18: MIIPS scan and determination of corrective phases with an additionally imprinted phase $\phi = 1000\,\mathrm{fs}^3\ (\omega-\omega_0)^3 + 500\,\mathrm{fs}^3\ (\omega-\omega_0)^2$. (a) 2D MIIPS scan of the first iteration revealing that a quadratic and cubic spectral phase is present. (b) - (e) Determined corrective phases after the first ($\phi^{(1)}$), second ($\phi^{(2)}$), third ($\phi^{(3)}$) and fourth ($\phi^{(4)}$) iteration step. The corrective phase approaches zero successively. (f) Total phase $\phi^{(1)}+\phi^{(2)}+\phi^{(3)}+\phi^{(4)}$ (blue dots) compared to the added phase (black curve). The obtained phase after the first iteration step is depicted in red. The laser spectrum is plotted as well. Figures (b) - (f) adapted from [93].

Chapter 4

Phase-controlled polarization decay in small and complex systems

The absorption of light is a well-known phenomenon. In the beginning of the 19th century Joseph Fraunhofer discovered the famous absorption lines in the spectrum of the sunlight, afterwards named Fraunhofer lines [96]. It was Gustav Kirchhoff and Robert Bunsen who found out that each chemical element exhibits absorption lines which allows its clear identification. The characteristic absorption properties of the elements allowed the assignment of the absorption lines observed by Fraunhofer to the components in the sun's atmosphere [97].
Not only the chemical elements, but also the chemical compounds like small and large molecules show specific absorption properties. The energies of the absorption lines correspond to the energy differences between the populated states (typically the ground state) and the excited states. In atoms, the lowest-energy absorption lines are well separated. A typical absorption line shape is the Lorentzian profile whose width is determined by the natural lifetime of the excited state (cf. chapter 2.4). In molecules, not only electronical, but also rotational and vibrational excitations are possible. A large number of excitations are present, located close to each other in the spectral regime and even overlapping, resulting in broad absorption bands. However, only little (if any) information of the dynamics of the absorption process can be retrieved from these static absorption spectra. Due to their spectral overlap, the line-shapes and widths of individual transitions to infer information on couplings among states or their lifetime cannot be accessed.

The dynamics can be revealed in time-resolved spectroscopy as already introduced in chapter 3.2. Pump–probe experiments are a common technique for time-resolved measurements which are based on two time-delayed laser pulses. In this chapter we investigate the absorption process in small and complex systems and the modification of the absorption properties in the course of transient-absorption measurements (cf. chapter 3.2). These pump–probe experiments with attosecond extended/extreme-ultraviolet (XUV) pulse trains and femtosecond infrared (IR) pulses in helium revealed that the absorption line shapes are strongly modified by the presence of a second laser pulse. Thereby, we focus on the case of perturbed polarization decay, i.e. the XUV attosecond pulses induce polarization and the IR femtosecond pulse perturbs it. The measurements in helium and the observed results are discussed in section 4.1. Moreover, a formalism

is developed that explains the observed changes of the absorption profiles in the time domain by a laser-induced phase shift of the systems' response. In section 4.2 the obtained knowledge about the absorption process and the induced dynamics resulting in the modifications of the absorption profiles is applied to a large dye molecule in the liquid phase in order to test the universal applicability of the new concept in both simple and complex systems.

4.1 Gas-phase experiments in helium

Recently, our group performed transient-absorption measurements in helium in which the two-electron dynamics was studied [3, 4]. In the pump–probe experiments attosecond and femtosecond pulses are used. The attosecond pulses derived from the femtosecond infrared pulses via high-harmonic generation exhibit an extremely broad spectrum in the extended or extreme ultraviolet (EUV/XUV) regime giving rise to few-pulse attosecond pulse trains, each of a duration less than 500 as. The infrared pulses with a pulse duration of about 7 fs are provided by our laser system (cf. chapter 3.1.1). The intensity of the IR pulses can be varied by an iris. The attosecond and femtosecond pulses are focused into a cell filled with helium gas. The EUV/XUV spectrum of the transmitted attosecond pulses is detected as a function of the time delay between the EUV/XUV and IR pulses. Alternatively, the XUV spectrum can be measured as a function of the IR-pulse intensity at a fixed time delay τ. Thereby, the striking effect was discovered that the absorption line profiles can be modified by changing the intensity of the time-delayed infrared pulse. The details of the setup (including the description of the attosecond beam line and the high-harmonic generation) are provided by [66, 98]. The important features of the setup that has to be pointed out here are the high temporal and spectral resolution. The combination of both allowed the observation of the discovered effect of laser-controlled spectral line shapes, discussed in the following.

There are different processes induced in the helium atoms by XUV light exceeding $\sim$60 eV. As one possibility, the attosecond pulses can directly ionize a helium atom:

$$\mathrm{He} \longrightarrow \mathrm{He}^{+} + \mathrm{e}^{-}. \tag{4.1}$$

Another possibility is that both electrons are transfered into a doubly excited state. These doubly excited states are metastable because of the electron-electron interaction and decay via autoionization:

$$\mathrm{He} \longrightarrow \mathrm{He}^{**} \longrightarrow \mathrm{He}^{+} + \mathrm{e}^{-}. \tag{4.2}$$

Both pathways lead to the same result, i.e. singly ionized helium atoms. These two pathways can be regarded as the arms of an interferometer and their interference leads to the well-known asymmetric line shapes which can be observed e.g. in photoabsorption spectra. These asymmetric absorption lines were described by Ugo Fano [22] and are termed Fano resonances. The autoionization cross section according to Fano is given by

$$\sigma_{\mathrm{Fano}} = \frac{(q+\Delta)^2}{1+\Delta^2} \text{ with } \Delta = \frac{E-E_0}{\hbar\Gamma/2}, \tag{4.3}$$

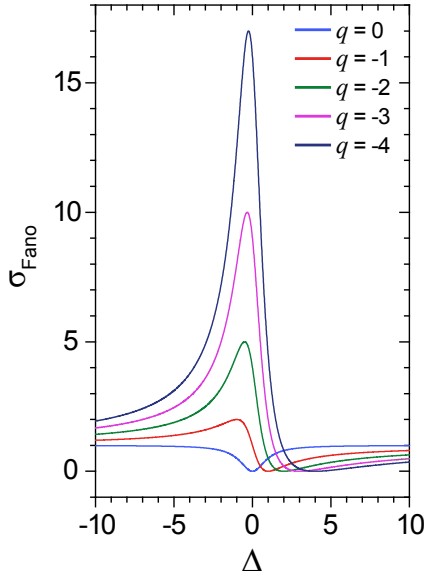

Figure 4.1: Lines shapes of Fano resonances for different asymmetry parameters q as function of the reduced energy Δ. For $q \to \pm\infty$ the profiles exhibit a Lorentzian line shape.

where E_0 corresponds to the resonance energy, Γ to the resonance width, Δ to the reduced energy and q is the Fano asymmetry parameter characterizing the asymmetry of the absorption line shape. The influence of the q parameter on the line shape is illustrated in Fig. 4.1.

The observations made in the experiment are that the Fano absorption line shapes of the doubly excited states can be transformed into Lorentzian profiles by increasing the intensity of the IR pulses that follow the XUV pulse. The scan of the IR-pulse intensity at a fixed time delay $\tau = 5$ fs, i.e. the XUV pulse excites the helium atoms first and the IR pulse arrives 5 fs later, is presented in Fig. 4.2. Lineouts of the absorption lines for the higher excited states are displayed in Fig. 4.3 for five different intensities. As it can be seen, the absorption lines of the different doubly excited states show the expected Fano shapes when there is no infrared laser present. For increasing IR-pulse intensity, the Fano lines are modified. At an IR peak intensity of about $2 \cdot 10^{12}$ W/cm^2 the profiles are Lorentzian. The absorption line shapes are further altered for higher intensities. The absorption peaks can be described by inverted Fano lines for about $3 \cdot 10^{12}$ W/cm^2. At $4 \cdot 10^{12}$ W/cm^2 window resonances can be assigned, before the absorption lines disappear at even higher intensities.

The infrared laser field obviously transforms the initially Fano-shaped absorption lines into Lorentzian profiles by increasing the pulse intensity. The arising question is how the observed effect can be explained. For this purpose, a closer look at the dipole response in the time domain is necessary.
The absorption of an XUV photon leads to the excitation of an electronic state. In the time domain picture, a dipole oscillation is induced which decays exponentially as given by the lifetime of the excited state. Symmetric Lorentzian absorption lines are obtained in the presence of isolated discrete states that are subject to exponential decay. Thereby, the linewidth Γ is determined by the inverse of the lifetime. As already introduced

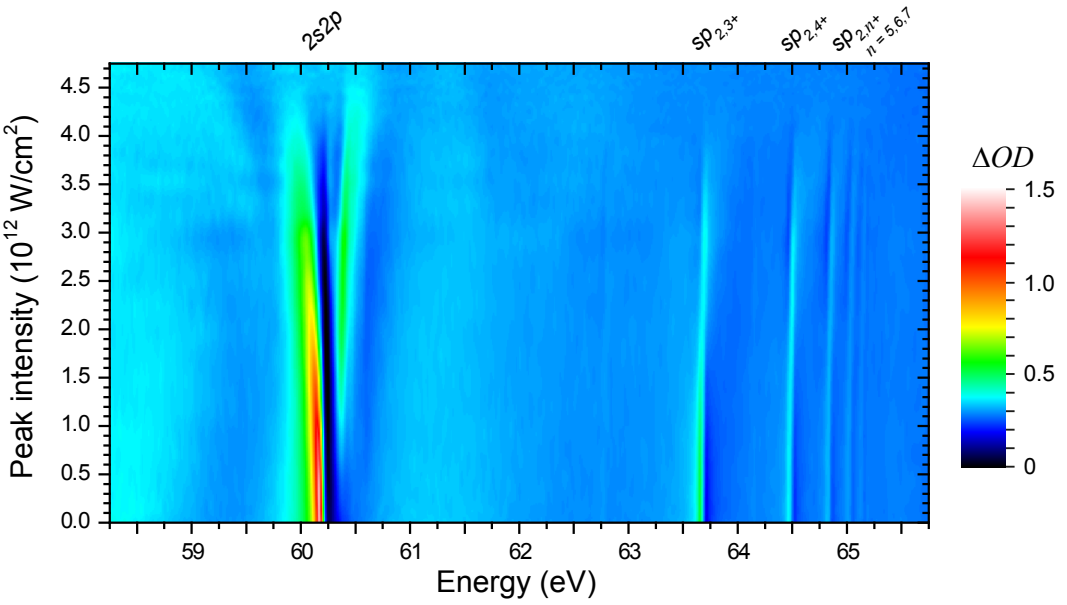

Figure 4.2: Two-dimensional plot of the measured absorption spectra as a function of the peak intensity of the infrared pulse at a fixed time delay $\tau \approx 5$ fs. The spectra are averaged over a range ± 2.4 fs. The chosen time delay corresponds to the case that the XUV pulse excites the helium atoms first, before the IR pulse follows 5 fs later. The different doubly excited states of helium are indicated. The modification of the absorption lines with increasing intensity is clearly visible.

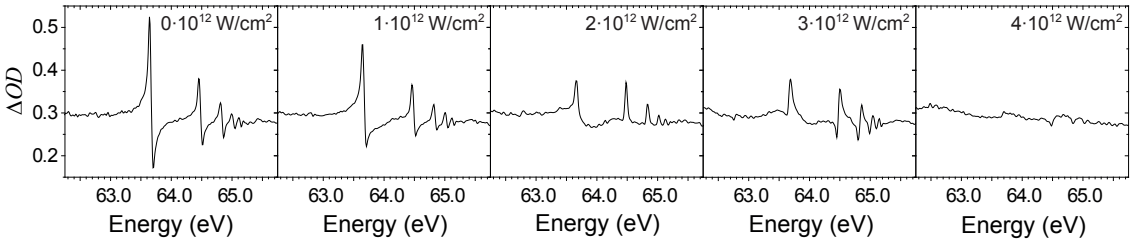

Figure 4.3: Absorption spectra at a fixed time delay $\tau = 5$ fs for different peak intensities of the infrared pulses as indicated (corresponding to lineouts of Fig.4.2 for the higher excited states). The initially Fano-shaped absorption lines are modified by the presence of the 7 fs short infrared laser pulse. The absorption profiles are transformed into Lorentzian lines at a peak intensity of about $2 \cdot 10^{12}$W/cm^2. For even higher intensities inverted Fano line shapes are obtained.

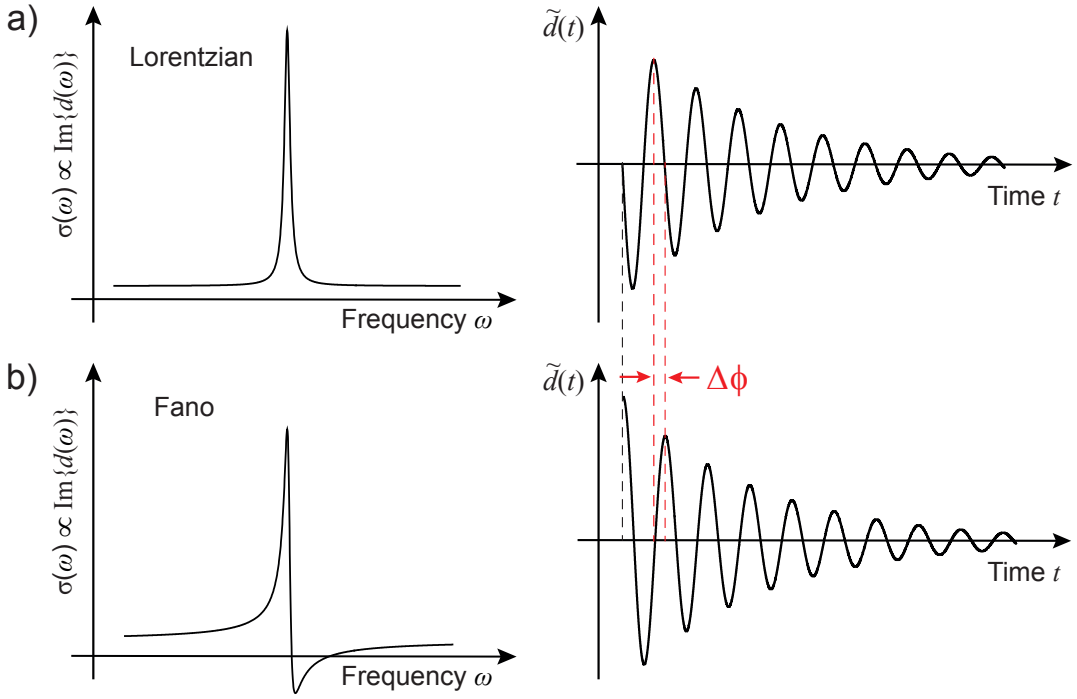

Figure 4.4: Line shapes and their corresponding dipole responses for a Lorentzian (a) and a Fano profile (b). The relation between absorption cross section $\sigma(\omega)$ and the dipole moment $d(\omega)$ is given by equation (2.47), i.e. $\sigma(\omega) \propto \mathrm{Im}\{d(\omega)\}$ where $d(\omega)$ is the Fourier transform of the dipole response $\tilde{d}(t)$. The additional phase leading to a Fano line profile stems from the coupling of the bound states to a continuum. However, a phase shift $\Delta\phi$ can also be induced by a laser field as demonstrated and discussed in this section.

in chapter 2.4, the absorption cross section can be derived from the dipole moment by $\sigma \propto \mathrm{Im}\{d\}$. The relation between the absorption cross section and the dipole response is depicted in Fig. 4.4. According to Fano's theory, asymmetric resonances appear if the discrete excited states are coupled to a continuum. In a time domain picture, an asymmetric Fano profile can also be explained by a phase shift of the dipole response (see Fig. 4.4). Thus, a phase shift of the dipole response causes a change of the line profile. The connection between the phase ϕ of the exponentially decaying dipole moment and the Fano q parameter was derived by our group and is given by

$$\phi(q) = 2\arg(q-i). \tag{4.4}$$

The inverse relation can be written as

$$q(\phi) = -\cot\left(\frac{\phi}{2}\right). \tag{4.5}$$

With the help of these equations, the phase of the dipole response can be mapped to the q parameter characterizing the absorption line shapes. For instance, a Lorentzian profile corresponds to a phase of $\phi = 2\pi \cdot n$ ($n \in \mathbb{Z}$) and $q \to +\infty$ or $q \to -\infty$.

Following the explanations above, the change of the absorption line profiles with increasing IR-pulse intensity, observed in the helium experiment, can be attributed to a phase

shift that is induced by the infrared laser. The presence of the laser field shifts the phases of the metastable doubly excited states and accordingly modifies the Fano line shapes. The laser-induced phases originate from the dynamical (AC) Stark effect where the electric laser field shifts the energy of the states. For monochromatic laser fields, the energy shift ΔE is constant. As the (non-monochromatic) laser pulses have a finite temporal duration, the energy shift is time-dependent. Since the pulse duration Δt_{laser} of the infrared laser is much shorter than the lifetime of the excited states, the total phase shift can be approximated by

$$\Delta\phi = -\frac{1}{\hbar}\int_{\Delta t_{\text{laser}}} dt'\,\Delta E(t'). \tag{4.6}$$

If the excitation by the IR pulse is impulsive, "kick-like", i.e. the pulse duration is much shorter than the lifetime of the states, the phase shift corresponds to the phase $\phi(q)$ and can thereby directly attributed to the q parameter. Thus, the modification of the absorption line shapes caused by the infrared pulse serves as a measure of this quantum phase and can be quantified using equations (4.4) and (4.5).

The manipulation of the phase of an excited state, induced by the interaction with short laser pulses, leads to a modification of the q parameter characterizing a natural Fano absorption line shape. Therefore, the inverse process, i.e. transforming a Lorentzian into a Fano absorption profile, should be possible as well. This scenario was proven by our group by focusing on the singly excited states of helium. These absorption lines exhibit a symmetric Lorentzian absorption profile in the absence of the additional laser field. However, the presence of the infrared laser pulse leads to the change of the absorption peaks into Fano lines and even more, an amplification of the EUV light at the resonances of the singly excited states, i.e. a gain, could be induced. The details concerning these measurements and experimental results are given in [3, 98].

The discussed experiments and the derived results provide clear evidence of the validity of the Fano-phase concept. The presented formalism enables the modification and control of the absorption profiles. The mapping between the Fano asymmetry parameter and the phase of the dipole response allows to extract information about the quantum phase of excited states and the dependence on interactions solely by analyzing line shapes. This offers the perspective to transfer the developed phase control of absorption profiles to more complex systems as it is discussed in the following section.

4.2 Experiments in the liquid phase

The possibility to control the absorption properties of a system, i.e. changing the absorption profile by an induced phase shift due to the variation of the laser pulse intensity, as demonstrated for the case of helium and explained in the previous section, is a promising result. It raises the question if the Fano-phase formalism can be adapted to other systems, not only atoms, but molecules or even larger systems like condensed-phase systems. In the case of helium, the singly excited states are well separated and the absorption profiles are spectrally narrow. The situation is different in larger systems like molecules. There are several states that even overlap spectrally, giving rise to broad absorption bands instead of single, isolated absorption lines.

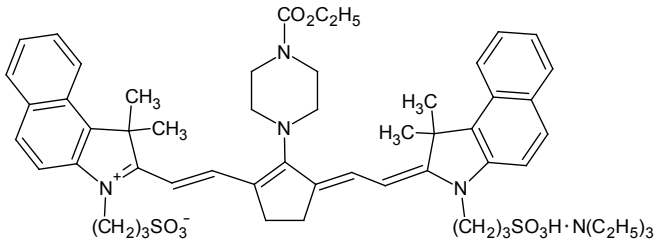

Figure 4.5: Molecular structure of the dye IR144. The central chain is framed by a nitrogen atom on either side. The conjugated double bonds form an extended π-electron system. Another mesomeric resonance structure with the positive charge located at the nitrogen atom at the other end of the central chain can be drawn so that the π-electrons can be regarded as delocalized.

Therefore, the idea is to choose a complex molecule as target and to perform transient-absorption measurements in order to investigate if the discovered control mechanism is applicable as well. Moreover, the liquid phase is chosen instead of a gaseous sample. The following sections give insight into the measurements and the obtained results. A numerical model is also introduced to reproduce and interpret the experimentally observed effects.

4.2.1 The liquid-phase target: dye IR144

The dye molecule IR144 is chosen as target system. It is a crystalline solid of dark maroon or bronze color. The following numbers are taken from [99, 100]. The chemical formula of IR144 is $C_{56}H_{73}N_5O_8S_2$ and it has a molar mass of 1008.34 g·mol^{-1}. The molecular structure of this complex molecule is shown in Fig. 4.5. The sequence of conjugated double bonds of the central chain framed by a nitrogen atom on the left and right side provides an extended π-electron system. The π-electrons are delocalized over the central nitrogen-carbon chain (more information is provided in section 4.2.3). Another mesomeric resonance structure where the positive charge is located at the nitrogen atom at the other end of the central chain can be drawn. The solution of IR144 in ethanol exhibits a broad absorption maximum at 750 nm (cf. Fig. 4.6) and the fluorescence maximum is located at 848 nm. IR144 is a laser dye which can be used for pulsed operation. The lasing wavelength is tunable around 880 nm.

Our decision for IR144 was taken because of several reasons. First of all, it is an example for a complex molecule which exhibits an absorption maximum close to a wavelength of 800 nm which is covered by the spectral range of our laser system. Secondly, IR144 is a standard dye and serves as a prototype system in spectroscopy, e.g. in transient-grating or 2D-spectroscopy [101–105]. Thirdly, it is a non-hazardous chemical, i.e. it is neither toxic nor carcinogenic. In our experiments, a solution of the dye IR144 in methanol is chosen which has a blue color. Such a solution (with a concentration typically smaller than 0.5 mmol/l) is used in the measurements described in the following as well as in the experiments discussed in chapter 5.3.

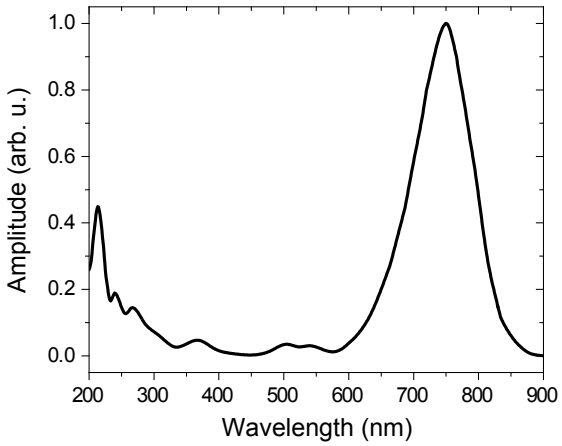

Figure 4.6: Absorption spectrum of the dye IR144 (solvent: ethanol). The dye has a broad maximum at a wavelength of 750 nm. Adapted from [100].

4.2.2 Transient-absorption measurements

For the transient-absorption measurements, the experimental setup described in chapter 3.3.1 is used. A solution of IR144 in methanol at a concentration of 0.125 mmol/l is prepared as sample. In the helium experiment, the pulse duration of the infrared pulse is much shorter than the lifetime of the dipole oscillation. In order to keep the pulse duration short compared to the decay times of the dye IR144, the sub-7 fs short pulses (obtained after the hollow-core fiber, cf. chapter 3.1.1) are used instead of the 30 fs laser pulses. The spectrum of the laser pulses is displayed in Fig. 4.7. The pump and probe beams are focused into the sample and the spot size amounts to roughly 240 µm in diameter. The time delay τ between pump and probe pulse is scanned in steps of $\sim$1.33 fs from the negative to the positive range. A positive τ corresponds to the usual pump–probe scenario in which the probe follows the pump pulse. The case of negative τ means that the probe pulse precedes the pump. The latter is equivalent to the positive time-delay range in the helium experiment presented in the previous section 4.1. There, the weak attosecond pulses can be regarded as probe pulses and the stronger IR laser pulse as pump. The energy of the probe pulse is kept constant at about 21 nJ, whereas the pump-pulse energy E_{pump} is varied in the course of the experiment and time-delay scans are carried out for different pump-pulse energies in analogy to the helium measurements. The more intense pump pulse in the liquid-phase experiments plays the role of the infrared pulse in the gas-phase helium measurements. For the derivation of the absorption spectra, the optical density $OD = -\log(S_p/S_L)$ (see equation (2.48)) is determined where S_p is the transmitted spectrum of the probe pulse as function of the time delay. The pure spectrum of the probe beam, i.e. no sample and no pump beam, is taken as reference laser spectrum S_L.

Figures 4.8 and 4.9 show time-delay scans in the range from -100 fs to +100 fs for different pump-pulse energies (ranging between 150 nJ and 1.25 µJ). In order to reduce noise induced by fluctuations of the laser pulse intensity, the absorption spectra for one specific τ are averaged over five pixels (one pixel corresponds to a time-delay step of about 1.33 fs). Combined with the error of the determination of the piezo position for $\tau = 0$ fs,

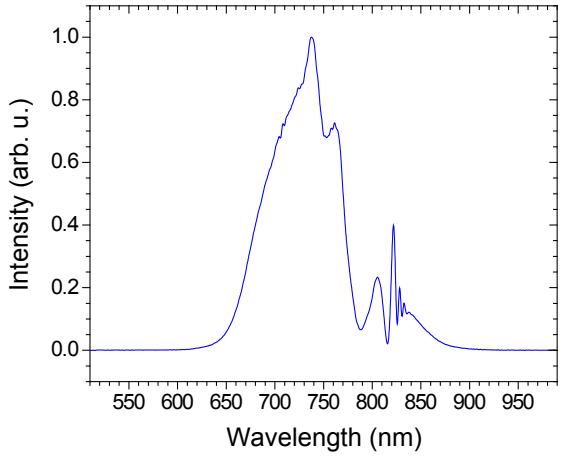

Figure 4.7: Spectrum of the laser pulses used for the liquid-phase transient absorption measurements.

the time delay τ can be estimated to an error of about ± 6 fs.
At low pump-pulse energies, the induced effects are minor, but become stronger for increasing pulse energies. A common feature of all scans is that the absorption signal is reduced at positive time delays compared to negative time delays. This can be explained by the fact that for positive time delays the pump pulse precedes the probe pulse. The pump pulse has already excited the sample prior to the probe pulse so that probe light is absorbed less. Around a time delay $\tau = 0$ fs, the modifications of the measured absorption spectra are strongest. The spectra get extended to the range of higher frequencies and the maximum is also shifted towards larger ω. In addition, a minimum (a dip-like feature) occurs in the range of $\omega \approx 2.4 - 2.5$ fs^{-1} at positive time delays with increasing pump-pulse energy. In the region around a time delay of 0 fs, the modifications are most distinct.

The interesting question is whether changes appear in the absorption spectra with increasing pump-pulse energy at negative τ, in order to investigate the analogous case to the helium perturbed polarization decay measurements. There, the change of the doubly-excited state absorption profiles from a Fano to a Lorentzian line shape was observed. For this purpose, the absorption spectra averaged over the time delay of the IR144 experiment are plotted as a function of E_{pump} for specific time delays close to $\tau = 0$ fs and presented in Fig. 4.10. Here, the spectra are normalized and scaled to the integrated spectral range 2.195 $-$ 2.902 fs^{-1}. Time delays of τ = -30 fs, -20 fs, -10 fs and 0 fs are chosen for comparison. Lineouts for τ = -20 fs and $\tau = 0$ fs are displayed exemplarily in Fig. 4.11.

For a time delay of -30 fs there are hardly any changes of the absorption spectrum visible. When the time delay approaches 0 fs, the modifications become stronger. First of all, the maximum at about 2.55 fs^{-1} shifts to higher frequencies for an increasing pump-pulse energy. Secondly, a minimum appears around 2.5 fs^{-1}. Thirdly, looking at the lineouts for a time delay τ = -20 fs, a shoulder becomes evident at about 2.4 fs^{-1} with a second minimum at lower frequencies next to it. This shoulder resembles more and more a peak if the time delay reaches $\tau = 0$ fs. The feature at about 2.3 fs^{-1} does not show any systematic trend and can be regarded as an artefact due to a strong oscillation of the

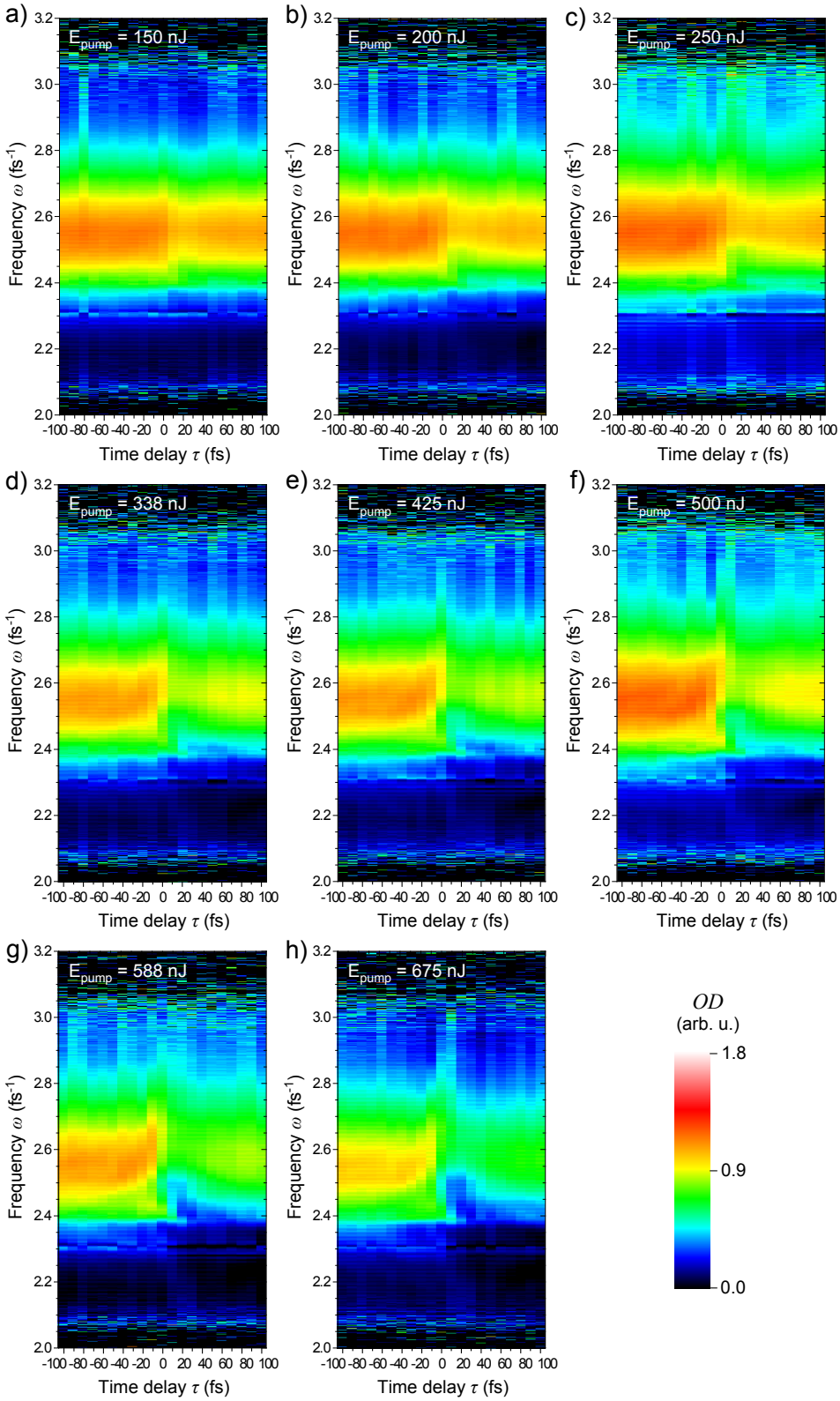

Figure 4.8: Measured absorption spectra of the transient-absorption experiment with IR144 in methanol for a pump–probe time-delay range from -100 fs to +100 fs. The transient-absorption measurements are carried out for different pump-pulse energies: (a) 150 nJ, (b) 200 nJ, (c) 250 nJ, (d) 338 nJ, (e) 425 nJ, (f) 500 nJ, (g) 588 nJ and (h) 675 nJ. The spectra are averaged over about ± 2.6 fs for each time delay τ.

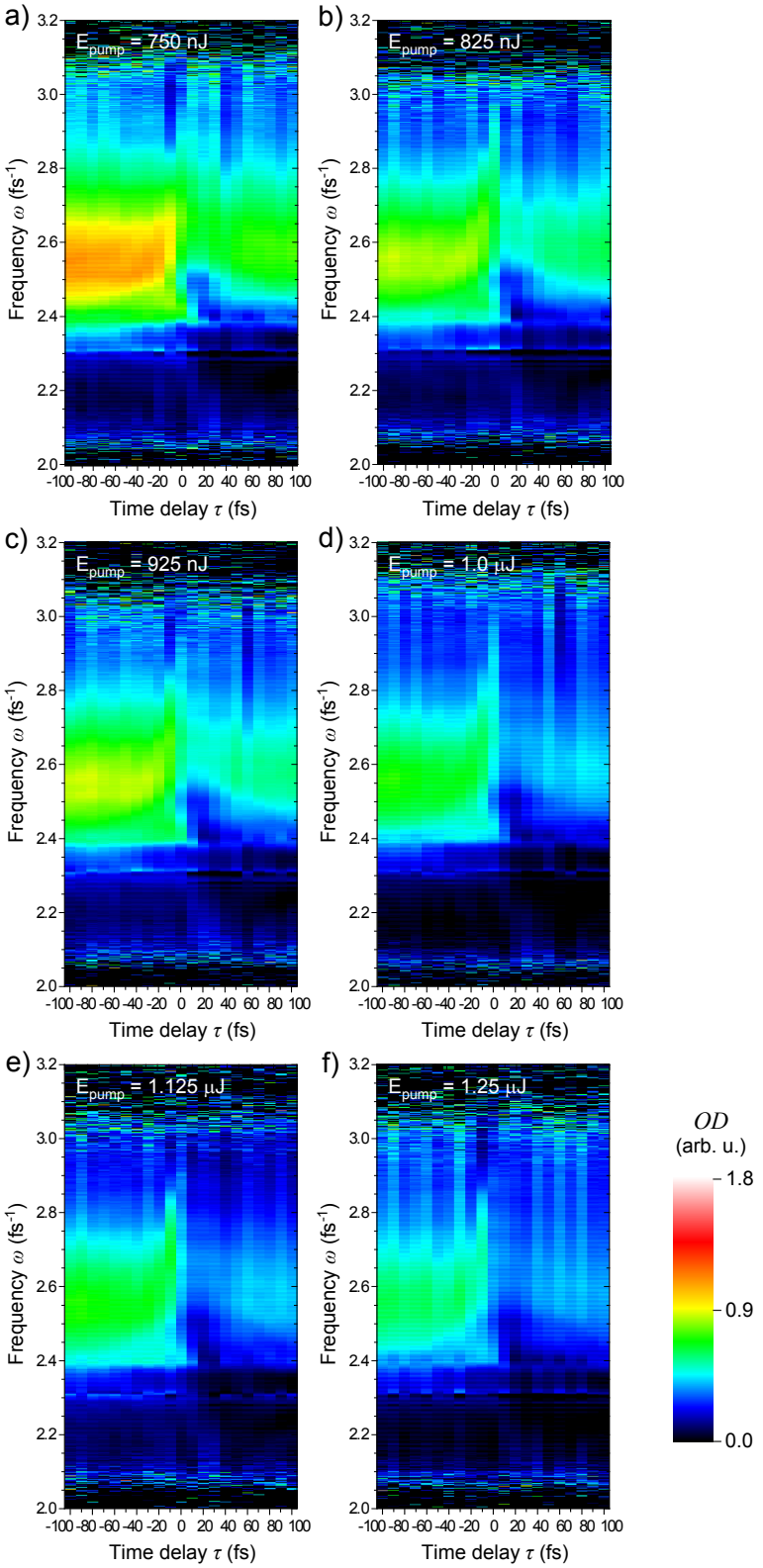

Figure 4.9: Transient-absorption measurements in a solution of IR144 in methanol for a pump–probe time-delay range from -100 fs to +100 fs. The transient-absorption measurements are carried out for different pump-pulse energies: (a) 750 nJ, (b) 825 nJ, (c) 925 nJ, (d) 1.0 µJ, (e) 1.125 µJ and (f) 1.25 µJ. The spectra are averaged over about ± 2.6 fs for each time delay τ.

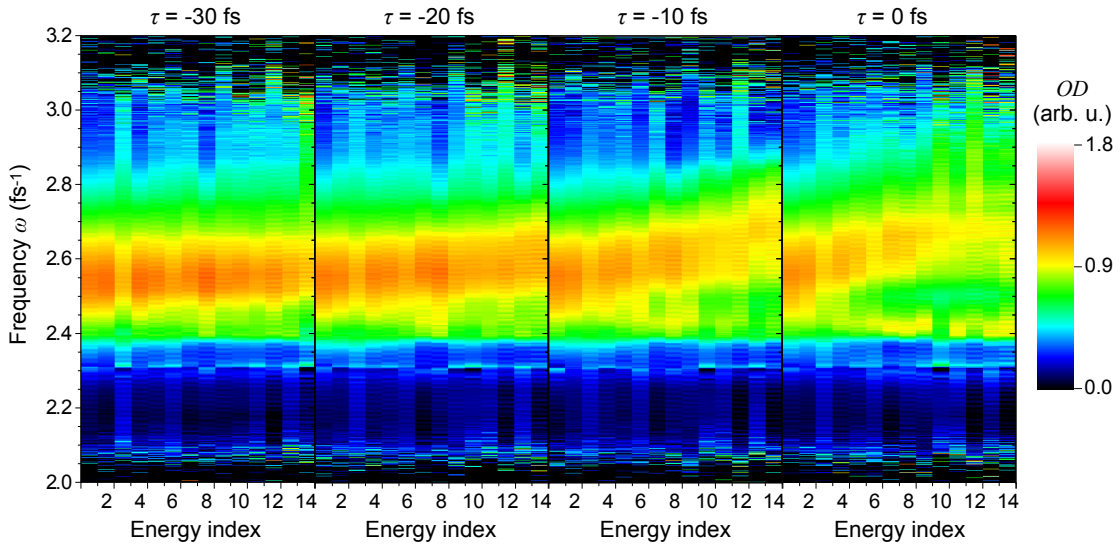

Figure 4.10: Intensity scans for different time delays τ = -30 fs, -20 fs, -10 fs and 0 fs ($\pm$6 fs). The pump-pulse energies are 150 nJ (1), 200 nJ (2), 250 nJ (3), 338 nJ (4), 425 nJ (5), 500 nJ (6), 588 nJ (7), 675 nJ (8), 750 nJ (9), 825 nJ (10), 925 nJ (11), 1.0 µJ (12), 1.125 µJ (13) and 1.25 µJ (14).

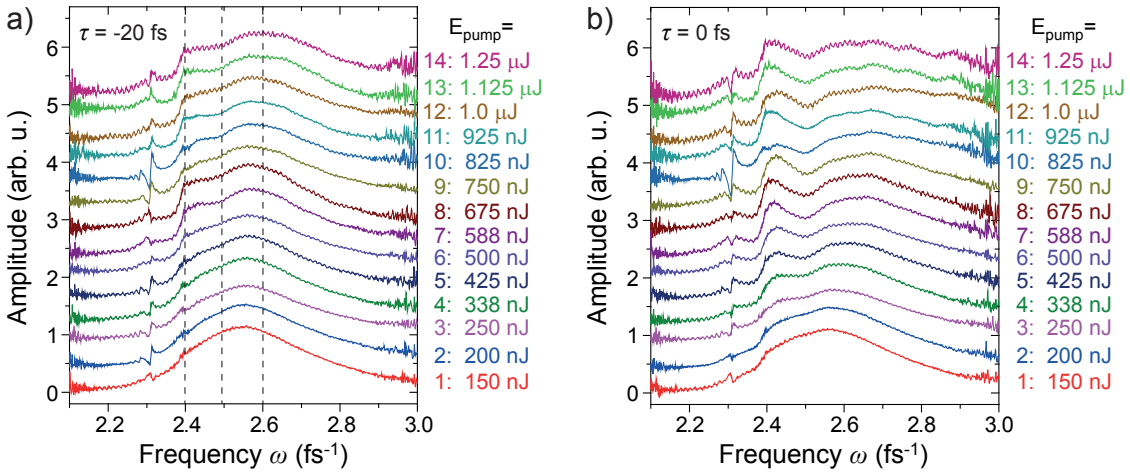

Figure 4.11: Lineouts of the absorption spectra for $\tau = -20 \pm 6$ fs (a) and $\tau = 0 \pm 6$ fs (b) to demonstrate the induced modifications with increasing pump-pulse energy. Dashed lines are added to guide the eye. The maximum at initially about 2.55 fs^{-1} is shifted to larger frequencies and a minimum at roughly 2.49 fs^{-1} occurs. Moreover, a shoulder/peak at about 2.4 fs^{-1} becomes apparent.

reference laser spectrum in this spectral regime (cf. the region around 810 - 830 nm in Fig. 4.7).
At a time delay of 0 fs, the pump and probe pulses overlap and the observed effects are very strong. However, even at a significant pulse separation of about -20 fs, modifications can be identified. There are various possible excitations in such a complex molecule like IR144 and the corresponding absorption lines are located spectrally close to each other and even overlap. Nevertheless, changes in the absorption spectra with increasing pump-pulse energy can be definitely recognized.
The questions we want to address in the subsequent section are: Is it possible to describe the observed modifications in analogy to the Fano-phase mechanism as it was developed for the case of helium? Can the formalism be applied to such a complex system?

4.2.3 Numerically modeling the absorption spectra

In order to understand and interpret the experimental results, a simulation is carried out. Our aim is to describe the observed changes in the absorption spectra at negative pump–probe time delays in analogy to the helium measurements where the Fano-phase concept was introduced. There, the changes of the line shapes are explained by a phase shift of the induced dipole oscillation. Thereby, the phase shift increases with the intensity of the infrared (pump) pulse. The model used for the description of the measurements in IR144 is discussed in the following. It has to be noted that a toy model is developed which can describe the observed features qualitatively. The toy model provides an intuitive and simple access to the description of the dynamics and can serve as a basis for more complex models or ab-initio simulations. The simulation was implemented in the course of a Bachelor thesis under my supervision and the following discussion refers to [106] in which further details can be found as well.

The theoretical model

In the provided explanation of the underlying model, a two-level system is assumed for simplicity. As derived in chapter 2.4, an oscillating electric field (e.g. a laser pulse) induces a dipole $d = q \cdot x$ in the atoms or molecules. The induced dipole can be related to the absorption coefficient α or the absorption cross section σ by (cf. equation (2.47))

$$\sigma(\omega) \propto \alpha(\omega) \propto \mathrm{Im}\left\{\frac{d(\omega)}{E_\mathrm{s}(\omega)}\right\} = \mathrm{Im}\left\{\frac{\mathscr{F}\left\{\widetilde{d}(t)\right\}}{E_\mathrm{s}(\omega)}\right\}, \tag{4.7}$$

where $E_\mathrm{s}(\omega)$ is the spectrum of the laser pulse and $d(\omega)$ can be derived from the Fourier transform of the induced dipole oscillation.
The crucial part of the simulation is the determination of the dipole response $\widetilde{d}(t)$ which is given by the expectation value of the dipole moment $\langle\Psi(t)\,|d|\,\Psi(t)\rangle$ with $d = q \cdot x$ (cf. chapter 2.4). The temporal evolution of the state has to be taken into account:

$$|\Psi(t)\rangle = c_n(t)\, e^{-i\frac{E_n}{\hbar}t}\,|n\rangle + c_m(t)\, e^{-i\frac{E_m}{\hbar}t}\,|m\rangle\,, \tag{4.8}$$

where $|n\rangle$ is the ground state, $|m\rangle$ the excited state and the E_i are the eigenenergies of the respective states given by the stationary Schrödinger equation. $|c_i(t)|^2$ corresponds to the population of state $|i\rangle$.
Hence, the dipole response can be written as

$$\widetilde{d}(t) = c_m^*(t)\, c_n(t)\, \langle m|d|n\rangle\, e^{-i\frac{E_n-E_m}{\hbar}t} + c.c. \tag{4.9}$$

where the transition dipole moments $\langle i|d|i\rangle$ are assumed to be zero. The transition dipole matrix element $\langle m|d|n\rangle$ is time-independent.

Furthermore, the dipole oscillation does not remain for infinity, but decreases in time with a damping constant Γ. The damping constant is determined by the lifetime of the polarization which is limited by system relaxation and inhomogeneous broadening within the system. Thus, the dipole oscillation can be written as

$$\widetilde{d}(t) = c_m^*(t)\, c_n(t)\, e^{i\frac{(E_m-E_n)}{\hbar}t}\, \langle m|d|n\rangle\, e^{-\frac{\Gamma}{2}t} + c.c. = c_m^*(t)\, c_n(t)\, e^{i\omega_{mn}t}\, \langle m|d|n\rangle\, e^{-\frac{\Gamma}{2}t} + c.c., \tag{4.10}$$

with $\omega_{mn} = (E_m - E_n)/\hbar$. As we do not know the matrix element $\langle m|d|n\rangle$, it is assumed to be constant. Since the laser pulse is regarded as a small perturbation of the system, the population of state $|n\rangle$ is approximately unchanged and $c_n(t) \approx 1$. Therefore, the expression for the dipole oscillation simplifies to

$$\widetilde{d}(t) \approx c_m^*(t)\, e^{-\frac{\Gamma}{2}t}\, e^{i\omega_{mn}t} + c.c. \tag{4.11}$$

The coefficient $c_m^*(t)$ can be calculated by time-dependent perturbation theory which is described in detail in [107, 108] and only a summary is provided here.

The laser pulse acts as a small perturbation to the system under study. The time-dependent Schrödinger equation with a small perturbation $\lambda\, \hat{W}(t)$ generally reads as

$$i\hbar\, \frac{\partial}{\partial t}\, |\Psi(t)\rangle = \left(\hat{H}_0 + \lambda\, \hat{W}(t)\right)\, |\Psi(t)\rangle\,. \tag{4.12}$$

The solution can be expanded into the eigenfunctions of the unperturbed Schrödinger equation (cf. chapter 2.5):

$$|\Psi(t)\rangle = \sum_j c_j(t)\, e^{-i\frac{E_j}{\hbar}t}\, |j\rangle\,. \tag{4.13}$$

Inserting this ansatz into equation (4.12) and taking the projection onto state $\langle m|$, the relation for the coefficient $c_m(t)$ is obtained:

$$i\hbar\, \frac{d}{dt}\, c_m(t) = \lambda \sum_j c_j(t)\, e^{i\omega_{mj}t}\, \left\langle m\left|\hat{W}(t)\right|\, j\right\rangle, \tag{4.14}$$

with $\omega_{mj} = (E_m - E_j)/\hbar$. Equation (4.14) is equivalent to the Schrödinger equation (4.12). As $\lambda \ll 1$, the coefficients can be expanded into a power series in λ:

$$c_m(t) = c_m^{(0)}(t) + \lambda\, c_m^{(1)}(t) + \lambda^2\, c_m^{(2)}(t) + ... \tag{4.15}$$

By inserting this expansion of $c_m(t)$ into equation (4.14) and sorting by the different orders of λ, the $c_m^{(i)}(t)$ can be determined.
At time $t = 0$ the system is in its ground state $|n\rangle$. Hence, $c_m^{(0)}(0) = \delta_{mn}$ and $c_m^{(i)}(0) = 0$ for $i \geq 1$. Then, the solution in first order of λ reads as

$$c_m^{(1)}(t) = -\frac{i}{\hbar} \int_0^t dt' \, e^{i\omega_{mn}t'} \, \langle m | \hat{W}(t) | n \rangle . \tag{4.16}$$

In our case, the perturbation $\hat{W}(t)$ is given by the dipole moment $d = q \cdot x$ and the laser field $E_{\text{laser}}(t)$:

$$\begin{aligned} c_m^{(1)}(t) &= -\frac{i}{\hbar} \int_0^t dt' \, e^{i\omega_{mn}t'} \, \langle m | d \, E_{\text{laser}}(t') | n \rangle \\ &= -\frac{i}{\hbar} \int_0^t dt' \, e^{i\omega_{mn}t'} \, E_{\text{laser}}(t') \, \langle m | d | n \rangle . \end{aligned} \tag{4.17}$$

Since we do not know the dipole matrix elements $\langle m|d|n\rangle$ for the dye IR144, this term is set constant again. Therefore, by inserting the result for $c_m^*(t)$ the dipole oscillation is determined in our simulation via

$$\widetilde{d}(t) \propto \frac{i}{\hbar} \left(\int_0^t dt' \, e^{-i\omega_{mn}t'} \, E_{\text{laser}}(t') \right) e^{-\frac{\Gamma}{2}t} \, e^{i\omega_{mn}t} + c.c. \tag{4.18}$$

In the simulation, the real electric field of the laser pulse is mimicked by a typical Gaussian envelope with a sinusoidal carrier wave,

$$E_{\text{laser}}(t) \propto e^{-\frac{(t-t_s)^2}{2\sigma^2}} \, e^{i\omega_0 t} + c.c., \tag{4.19}$$

where ω_0 represents the center frequency and t_s a shift in time, so that the full pulse profile is located in the range $t > 0$.
Finally, it has to be taken into account that the excited states are not populated at the same instant of time. The dipole oscillations of states that are excited later in time will last longer. Therefore, an imaginary part is added to the transition frequency, i.e. $\omega_{mn} + i\Gamma/2$, which contains the decay constant Γ.
The final result describing the dipole oscillation is given by

$$\widetilde{d}(t) \propto \frac{i}{\hbar} \left(\int_0^t dt' \, e^{i(\omega_0 - \omega_{mn})t'} \, e^{\frac{\Gamma}{2}t'} \, e^{-\frac{(t'-t_s)^2}{2\sigma^2}} \right) e^{-\frac{\Gamma}{2}t} \, e^{i\omega_{mn}t}. \tag{4.20}$$

Here, the rotating-wave approximation is applied in which the rapidly oscillating term $\omega_0 + \omega_{mn}$ is neglected and the complex representation of $\widetilde{d}(t)$ is used.
Now, the absorption spectrum for the transition $|n\rangle \longrightarrow |m\rangle$ can be derived by equation (4.7).

So far, only one single pulse, i.e. the excitation pulse, is considered. In the experiment, two laser pulses of identical shape, i.e. a strong pump pulse and a weak probe pulse, interact with the sample and the time delay between the two pulses is scanned. Therefore, a second pulse, i.e. the control pulse, is introduced in our model. As the two pulses exhibit an identical shape, but they are delayed in time by τ, the complex control pulse is described by

$$E_{\text{control}}(t) \propto e^{-\frac{(t-t_s-\tau)^2}{2\sigma^2}} e^{i\omega_0 t}. \tag{4.21}$$

The control pulse causes a shift of the resonance frequency due to the dynamical Stark effect. The shift of the resonance frequency depends on the intensity of the laser pulse and the modified resonance frequency is given by

$$\widetilde{\omega}_{mn} = \omega_{mn} + \Delta\omega(t) = \omega_{mn} + \widetilde{c} \cdot |E_{\text{control}}(t)|^2 = \omega_{mn} + \widetilde{c} \cdot I_{\text{control}}(t). \tag{4.22}$$

The coupling constant $\widetilde{c}$ is a measure for the magnitude of the laser-induced frequency shift. In contrast to the monochromatic case where the induced frequency shift is constant, the laser pulse induces a time-dependent shift $\Delta\omega(t)$. Therefore, the additional phase ϕ imprinted on the dipole oscillation can be expressed by

$$\phi(t) = \int_0^t dt' \, \Delta\omega(t') = \int_0^t dt' \, \widetilde{c} I_{\text{control}}(t'). \tag{4.23}$$

Moreover, the term $\exp(i\omega_{mn}t)$ and, hence, the phase $\phi(t)$ is included twice in equation (4.20): firstly as part of the coefficient $c_m^*(t)$ and secondly as additional term to the carrier frequency of the dipole oscillation $\omega_{mn}t$. Thus, the induced phase does not only shift the resonance frequency, but leads to a change of the excited state population. Therefore, the simulation does not describe the phase shift to be "kick-like", i.e. instantaneous, but following the control pulse envelope. The dipole oscillation is altered and the additional phase causes a change of the absorption profile as already observed in helium.

As there is not only one single transition in the dye molecule IR144, but a large number of possible excitations, a dipole response consisting of the sum of different dipole oscillations $\widetilde{d}_k(t)$ is assumed. However, each $\widetilde{d}_k(t)$ is calculated in the way explained above. The absorption spectrum is then determined by

$$\alpha(\omega) \propto \text{Im}\left\{ \frac{\mathscr{F}\left\{\sum_k \widetilde{d}_k(t)\right\}}{E_{\text{s}}(\omega)} \right\}. \tag{4.24}$$

The spectrum $E_{\text{s}}(\omega)$ is the Fourier transform of the temporal electric field of the laser pulse.

Modeling the transitions in the molecule IR144

In order to determine the dipole responses $\widetilde{d}(t)$, the possible excitations of the IR144 molecule need to be known. As the dye IR144 is a complex molecule (see structure shown in Fig. 4.5), the electronic and vibrational energy levels cannot be calculated in a simple,

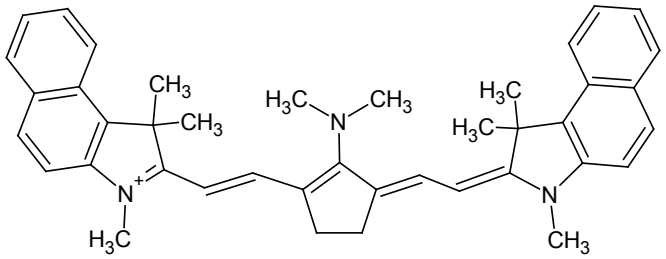

Figure 4.12: Simplified molecular structure of IR144 used in the calculations of the infrared vibrational transitions in the ground and first excited state.

straightforward way. However, we can estimate the energy levels and derive the possible transitions by a very simple model. The electronic transition from the ground state to the first excited state is estimated by the particle-in-a-box model. The vibrational levels in the ground and first excited state (infrared absorption) are calculated by Jan Mewes from the Dreuw group, IWR Heidelberg, but for a simplified molecular structure where the substituents are replaced by methyl groups as depicted in Fig. 4.12.

As already mentioned in section 4.2.1, the central chain consists of conjugated double bonds so that it has a planar geometry. The electron density of the π molecular orbitals is concentrated above and below the molecular plane and the π electrons can be regarded as delocalized along the chain. We assume that the lowest energy electronic transition will stem from the excitation of this π-electron system. Only the two naphthalene groups at either side of the molecule exhibit another conjugated π-electron system. However, the lowest excitation energies of naphthalene are about 3 eV [109] so that contributions to the lowest energy absorption band of IR144 can be excluded. In the lowest energy transition, a π electron is excited from the highest occupied molecular orbital (HOMO) to the lowest unoccupied molecular orbital (LUMO). The excitation energy is estimated by a semiempirical method, the so called free-electron molecular-orbital (FE MO) method [110]. The model assumes that the π electrons can move freely along the conjugated chain of the molecule. In case of the IR144 molecule, the chain is built up by nine carbon atoms and two nitrogen atoms, each of which form the end of the conjugated chain. The π electrons are trapped in this nitrogen-carbon chain corresponding to the particle-in-a-box principle. The energy levels of a particle in a box are given by

$$E_n = \frac{h^2 n^2}{8mL^2}, \tag{4.25}$$

where m is the electron mass and L is the box length. The transition energy is given by

$$\Delta E = E_{\mathrm{LUMO}} - E_{\mathrm{HOMO}} = \frac{h^2}{8mL^2}\left(n^2_{\mathrm{LUMO}} - n^2_{\mathrm{HOMO}}\right) = \frac{h^2}{8mL^2}\left(2n_{\mathrm{HOMO}} + 1\right), \tag{4.26}$$

since the LUMO is the next higher state of the HOMO, i.e. $n_{\mathrm{LUMO}} = n_{\mathrm{HOMO}} + 1$. Thus, the box length L and the n state of the highest occupied π molecular orbital need to be found out which is done in the following way: The central chain contains five double bonds with two π electrons each, yielding ten electrons. As the lone pair of the nitrogen atom takes part in the π bonding as well (cf. [110]), twelve electrons have to be considered in total.

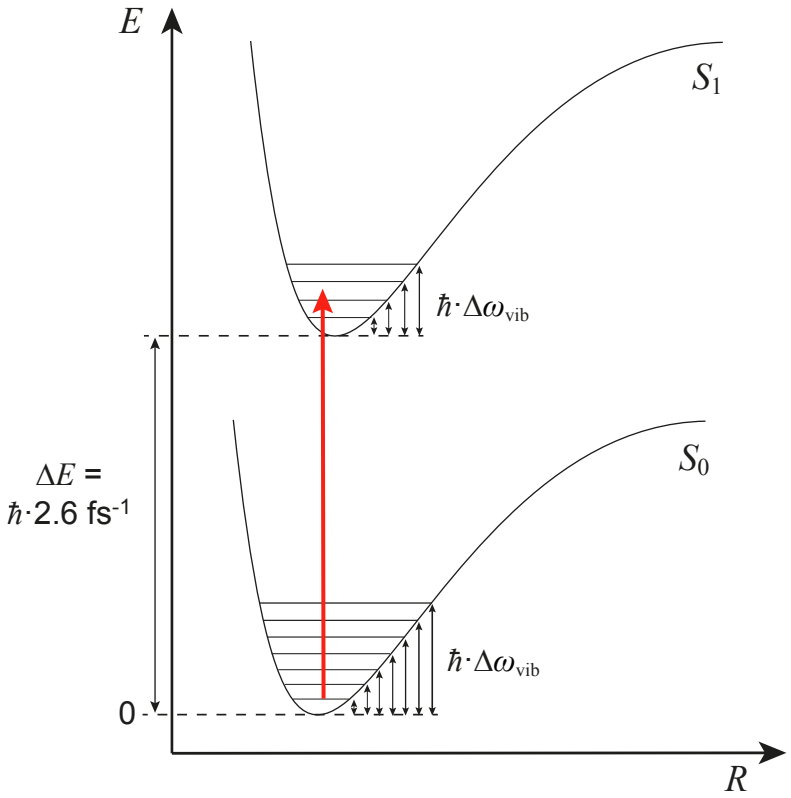

Figure 4.13: Schematic of the calculated energy levels of IR144 used in the simulation. The offset energy of the first electronically excited state is estimated by the free-electron molecular orbital method which treats the π electrons as particles in box. The vibrational states $\Delta\omega_{\text{vib}}$ were obtained by cooperation with a theory group [111].

Hence, the six lowest energy levels, $n = 1,\ 2,\ 3,\ 4,\ 5$ and 6 are occupied, because each molecular orbital is filled with two π electrons of opposite spin, and $n_{\text{HOMO}} = 6$.
The nitrogen-carbon chain includes ten bonds. As conjugated bond length, 1.40 Å are typically assumed. Adding an extra bond length at each end of the nitrogen-carbon chain yields a total box length of $12 \cdot 1.40$ Å $= 16.8$ Å. Thus, a transition energy of

$$\Delta E \approx 1.73 \text{ eV} \tag{4.27}$$

is determined which corresponds to a wavelength of about 717 nm and a frequency of approximately 2.6 fs^{-1}. This is in very good agreement to the absorption maximum of the dye IR144 located at about 750 nm (cf. Fig. 4.6). ΔE is taken as the energy difference between the first electronical excited state and the ground state as indicated in Fig. 4.13.

The vibrational states in the electronical ground (S_0) and first excited (S_1) state are calculated by Jan Mewes [111] as already mentioned at the beginning of this section. The calculations are based on density functional theory. The Schrödinger equation for the electrons is iteratively solved in the field of the nuclei, using the Born-Oppenheimer approximation. After the electronic wave functions of the ground and excited state are obtained, the vibrational states are determined. For this purpose, the normal modes and their frequencies are calculated by the conventional method of diagonalizing the Hessian matrix [112–114].

Frequency $\Delta\omega_{\text{vib}}$ (fs^{-1})	Intensity (arb. u.)	Population probability
0.230	2784	0.30
0.239	1487	0.24
0.249	1232	0.19
0.265	3284	0.12
0.295	2861	0.06
0.297	1637	0.05
0.303	2040	0.04

Table 4.1: Calculated vibrational states of the ground state S_0 [111]. Only the states with a population probability (given by the Boltzmann distribution) > 0.1 are taken into account in the simulation (cf. [106]). A schematic drawing of the energy levels is shown in Fig. 4.13.

As result a few hundred of vibrational states are calculated for both the ground and excited state, however, they exhibit different contributions. We restrict ourselves to the vibrational states with strongest contributions, i.e. we select only the vibrational states with an intensity > 1000. Thus, for the first excited state only four vibrational states are selected, whereas for the S_0 electronic ground state seven vibrational states are chosen. The number of relevant vibrational states in S_0 is further reduced since the population of the vibrational states in S_0 is determined by the temperature T. The population probability is given by the Boltzmann distribution

$$w(\Delta E) \propto e^{-\frac{\Delta E}{k_B T}}, \tag{4.28}$$

where a thermal energy of $k_B T = 1/40$ eV is assumed. Only the infrared vibrational states with a population probability ≥ 0.1 are considered so that in total four vibrational states are taken into account in the electronic ground state. For the ground state, the offset energy (zero-point energy) is neglected and the offset of the first excited state is assumed to be 2.6 fs^{-1} as derived above. The vibrational states are listed in Tab. 4.1 for the ground state and in Tab. 4.2 for the first excited state. The considered vibrational states in the ground and excited state and the used energy assignments are shown schematically in Fig. 4.13.
Finally, the transition frequencies are determined by taking all possible combinations between the states in S_1 and in S_0. Thereby, the Franck-Condon overlap is neglected to keep the model simple. Thereby, it is assumed that all transitions have the same transition strength. The determined spacing of the various transitions is in the range of 0.01 – 0.02 fs^{-1}.

In order to cross-check our toy model, we compare it to the measured fluorescence spectrum by Carson et al. [115]. From their fluorescence spectrum a difference of about 0.025 fs^{-1} between the transition modes can be deduced (cf. [106]). Therefore, we can make the assumption that the separation of the possible transitions is in the range of 0.010 – 0.025 fs^{-1}. Here, it has to be emphasized again that our aim is to qualitatively model and understand the experimental absorption spectra. Since we do not seek to give

Frequency $\Delta\omega_{\mathrm{vib}}$ (fs^{-1})	Frequency ω (fs^{-1}) $= \Delta\omega_{\mathrm{vib}} + 2.6$ fs^{-1}	Intensity (arb. u.)
0.215	2.815	3504
0.238	2.838	1398
0.240	2.840	1041
0.292	2.892	2117

Table 4.2: Calculated vibrational states of the first electronically excited state S_1 [111] considered in the numerical model (cf. [106]). A sketch of the energy levels is presented in Fig. 4.13.

quantitative results and to calculate the spectra with high accuracy, the approximations and simplifications made are justified.

Comparison of simulation and experiment

The considerations explained in the previous section are now used to mimic the measured absorption spectra by 22 equidistant transitions in the frequency range from 2.34 to 2.76 fs^{-1}. A spacing of 0.02 fs^{-1} and equal amplitudes are assumed. The laser pulses are modeled by a Gaussian spectrum centered around 2.6 fs^{-1} and have a pulse duration of about 8 fs. As the lifetimes of the various transitions are not known, a common damping constant Γ is chosen for all considered transitions. A value of $\Gamma = 0.1$ fs^{-1} is found to match the intensity-scan spectra best. In the experiment, the energy of the pump pulse is varied. In the Fano formalism, the phase shift induced by the pump pulse leads to a modification of the absorption profile. The higher the pulse intensity, the larger is the change of the line shape. In the simulation, the induced phase shift is implemented by equation (4.23) and determined by the intensity of the laser pulse I and the coupling constant $\widetilde{c}$. In the following, we refer to the product $\widetilde{c}I$ as coupling c. The coupling is assumed to be the same for all transitions that couple to the laser pulse. In the numerical model, the experimental intensity change of the pump pulse is imitated by changing the coupling c which is a measure for the induced phase shift. The value of $\widetilde{c}$ is varied to modify the coupling. However, a change of the coupling c can be interpreted in two ways: (i) the pulse intensity is constant so that the coupling constant is different or (ii) the coupling constant remains unchanged, but the pulse intensity varies. A value of 106 for the coupling $\widetilde{c}I$, in the units chosen here, corresponds to an accumulated phase of 2π for the laser pulse of duration 8 fs as used here throughout.

In the simulation, it is assumed that different transitions are coupled to the laser pulse and experience the induced additional phase. The aim is to find a configuration of coupled transitions, which best fit the experimentally measured spectra in their dependence on time delay and intensity. In Fig. 4.14, the measured absorption spectra versus pump-pulse energy are shown for different pump–probe time delays and compared to two simulations. The time delays are chosen to be in the negative range, but close to the full pulse overlap at $\tau = 0$ fs. This corresponds to the situation in the helium measurements (cf. section 4.1) where the line shape modifications are observed if the IR laser pulse (pump) follows

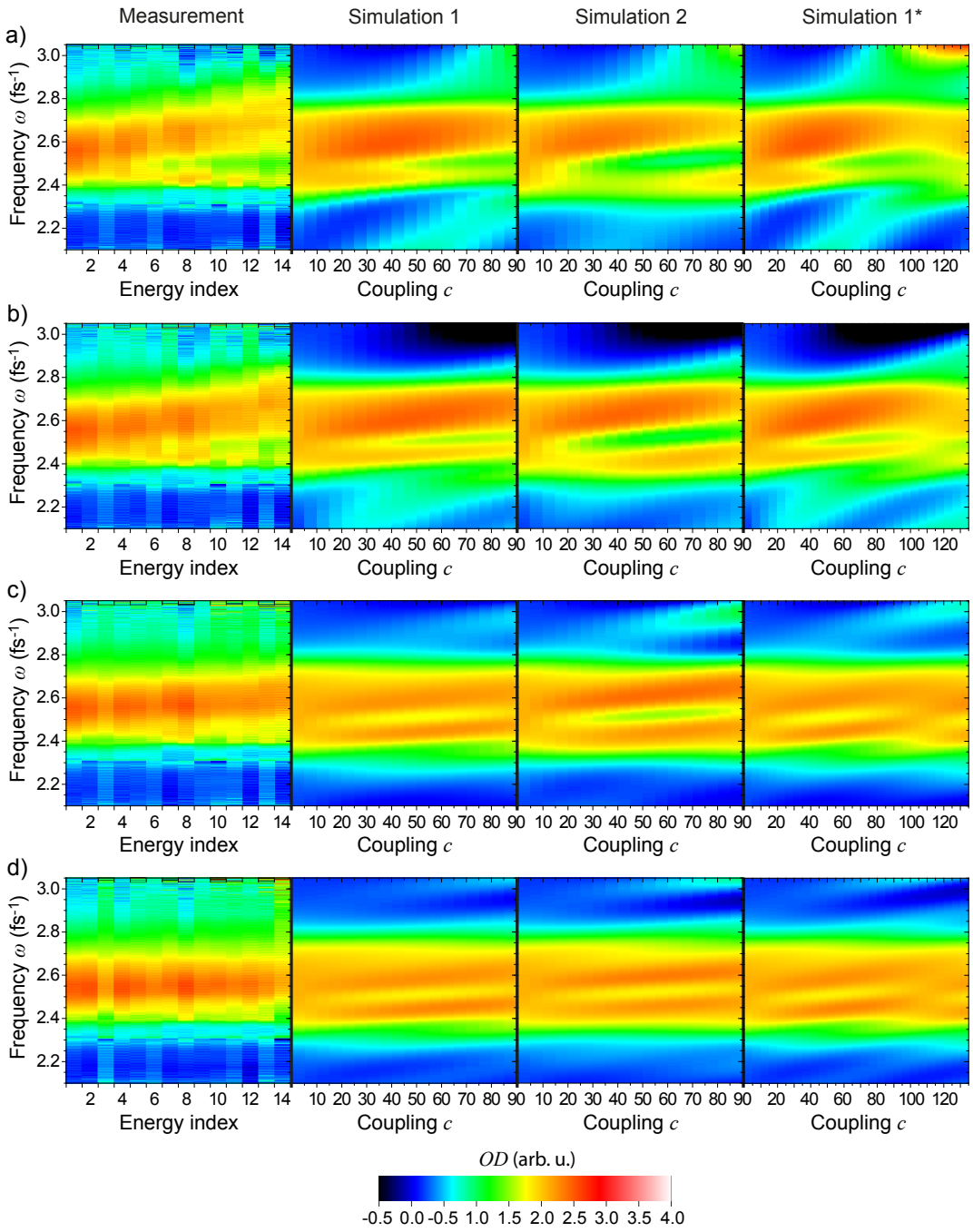

Figure 4.14: Comparison of measurement and simulation. Two-dimensional representation of the measured and simulated absorption spectra as a function of the pump-pulse energy E_{pump} and the coupling constant c, respectively, for different time delays τ: (a) -5 fs, (b) -10 fs, (c) -20 fs and (d) -30 fs. The pump-pulse energies are 150 nJ (1), 200 nJ (2), 250 nJ (3), 338 nJ (4), 425 nJ (5), 500 nJ (6), 588 nJ (7), 675 nJ (8), 750 nJ (9), 825 nJ (10), 925 nJ (11), 1.0 µJ (12), 1.125 µJ (13) and 1.25 µJ (14). In the simulations, 22 transitions ranging from 2.34 to 2.76 fs^{-1} in steps of 0.02 fs^{-1} with a damping constant $\Gamma = 0.1$ fs^{-1} are taken into account to model the measured absorption spectra. Laser pulses with a duration of 8 fs and a Gaussian spectrum centered at 2.6 fs^{-1} are considered. In simulation 1, it is assumed that the four transitions at frequencies 2.36 fs^{-1}, 2.38 fs^{-1}, 2.50 fs^{-1} and 2.52 fs^{-1} couple to the control pulse. In simulation 2, three transitions with frequencies 2.50 fs^{-1}, 2.52 fs^{-1} and 2.54 fs^{-1} are coupled to the laser field. Simulation 1^* presents the results of simulation 1, but for a larger range of the coupling c corresponding to higher pulse intensities for a constant coupling constant $\widetilde{c}$.

the attosecond pulse train (probe). The absorption spectra are all normalized to the integral of the spectral range $2.195 - 2.952$ fs^{-1}. For comparison, two simulations are presented that closely mimic the measurements. The two simulated cases differ in the selected transitions that couple to the control laser pulse. In simulation 1, it is assumed that the four transitions at frequencies 2.36 fs^{-1}, 2.38 fs^{-1}, 2.50 fs^{-1} and 2.52 fs^{-1} experience the laser-induced phase shift. In simulation 2, only the transitions at frequencies 2.50 fs^{-1}, 2.52 fs^{-1} and 2.54 fs^{-1} are considered to be affected by the laser. Simulation 1* represents simulation 1, but for a larger coupling range. The coupling starts at 0 in all simulations, whereas in the measurement the minimum pump-pulse energy is 150 nJ.

In the measurements, it can be clearly seen that the absorption maximum shifts to higher frequencies with increasing pump-pulse energy. This effect becomes stronger when the time delay τ approaches 0 fs. At $\tau =$ -30 fs, the shift is difficult to identify. Another feature that appears for time delays close to 0 fs is a minimum at approximately 2.5 fs^{-1}. The question is if the simulation parameters can be adapted in such a manner that the experimental data are reproduced. Comparing simulation 1 to the measurements, the answer is yes. Especially for time delays $\tau =$ -5 fs and $\tau =$ -10 fs, the agreement is very good. For larger time delays $\tau =$ -20 fs and $\tau =$ -30 fs, the simulation still exhibits the minimum at about 2.5 fs^{-1} that shifts to slightly higher frequencies with increasing coupling c. In the measured data, the minimum lacks or exists only rudimentary.
Simulation 2 seems to agree with the experimental results as well for $\tau =$ -5 fs, maybe even better than simulation 1. The shift of the absorption maximum and the minimum around 2.5 fs^{-1} resemble the measurement. However, for the other time delays displayed in Fig. 4.14 simulation 2 is less suitable as the characteristic features are much more pronounced than in the measured spectra.
Simulation 1* covers a larger coupling range which can be understood in the way that a larger intensity range is scanned. This scenario is less able to mimic the experimental results. The minimum at $\omega \approx 2.5$ fs^{-1} becomes less for higher couplings in the range of 100 – 110 (corresponding to an accumulated phase shift of 2π) before it reappears for even higher values of c. This feature is not observed in the measurements and implies that such high pulse intensities are not achieved in the experiment.
The simulation results and their agreement with the experimental data highly depend on the chosen parameters. It is possible to reconstruct the measured absorption spectra, but it has to be noted that there is not only one specific set of parameters that can be used. The chosen coupling range from 0 to 90 seems to be appropriate for simulation 1, but it could be argued, for example, that a smaller coupling range for simulation 2 might also serve as description.

The lineouts of the measurement and simulation 1 for time delays $\tau =$ -5 fs, -10 fs, -20 fs and -30 fs are displayed in Fig. 4.15 for a more detailed comparison than it is possible with the two-dimensional plots shown in Fig. 4.14. For small time delays, the simulation reproduces the measurement very well. The minimum at $\omega \approx 2.5$ fs^{-1} and the second minimum at $\omega \approx 2.35$ fs^{-1} can be described. Furthermore, the absorption maximum shifts to higher frequencies. At larger time delays between the two pulses, the spectral position of the minima changes in the simulation. As this is not the case in the measurement where the minima do not shift with time delay τ, the agreement of simulation and measurement is reduced.

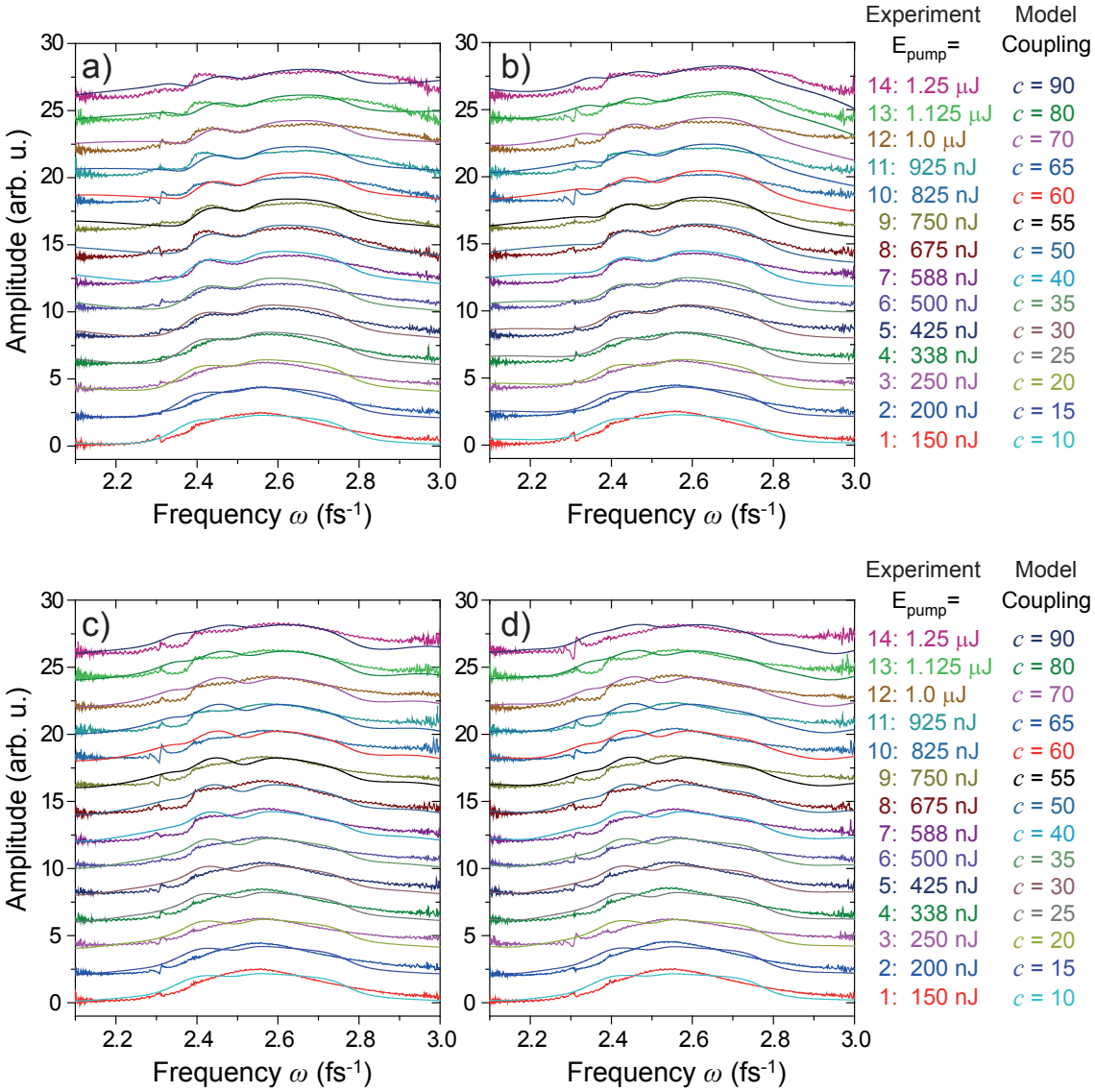

Figure 4.15: Comparison of measurement and simulation. Lineouts for time delays τ of -5 fs (a), -10 fs (b), -20 fs (c) and -30 fs (d) for the different pump-pulse energies used in the experiment and the adapted coupling constants c chosen in the simulation. The simulation to model the measured absorption spectra is simulation 1 which is displayed in Fig. 4.14. The assumption is made that four transitions with frequencies 2.36 fs^{-1}, 2.38 fs^{-1}, 2.50 fs^{-1} and 2.52 fs^{-1} couple to the control pulse. Especially for a time delay around -5 fs the simulation can qualitatively recover the measurements. The more negative the time delay is, the less well is the agreement. The feature at $\omega \approx 2.3$ fs^{-1} in the experimental data has to be regarded as an artefact originating from a fast oscillation in the reference laser spectrum in this specific spectral range.

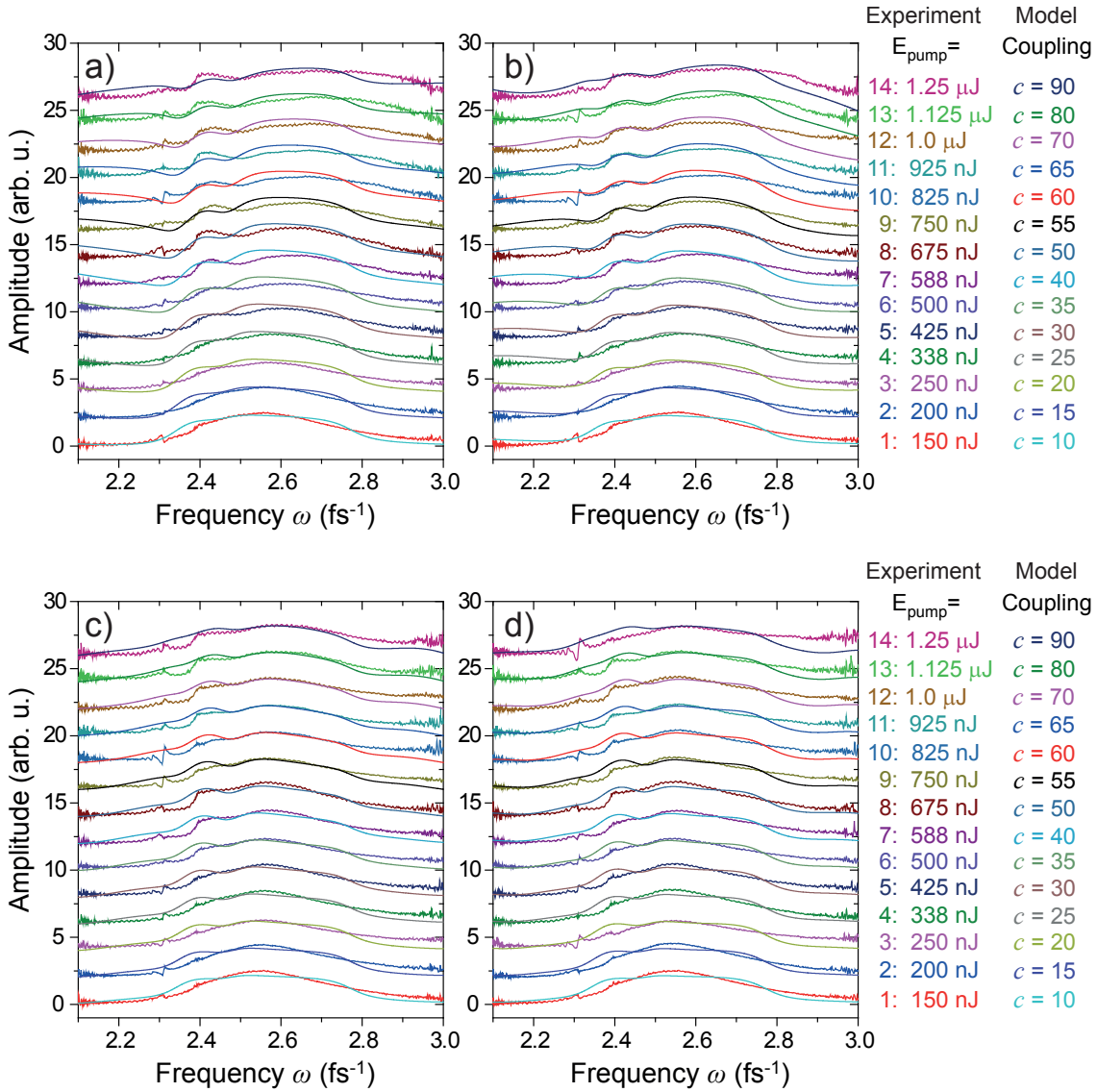

Figure 4.16: Comparison of measurement and simulation. Lineouts for time delays τ of -5 fs (a), -10 fs (b), -20 fs (c) and -30 fs (d) for the different pump-pulse energies used in the experiment and the adapted coupling constants c chosen in the simulation. The simulation to model the measured absorption spectra takes transitions into account which are slightly shifted compared to simulation 1. This time it is assumed that the four transitions with frequencies 2.34 fs^{-1}, 2.36 fs^{-1}, 2.46 fs^{-1} and 2.48 fs^{-1} are coupled to the control laser field. Now, simulation and measurement agree better for time delays of -10 fs and -20 fs. However, at $\tau = 0$ fs a reduced agreement is observed. Again, the feature at about 2.3 fs^{-1} in the measured spectra has to be regarded as an artefact.

In order to achieve a better agreement for intermediate time delays (τ = -10 fs and -20 fs), simulation 1 is modified (cf. Fig. 4.16). Now, transitions at slightly shifted frequencies of 2.34 fs^{-1}, 2.36 fs^{-1}, 2.46 fs^{-1} and 2.48 fs^{-1} are considered to experience the laser-induced phase shift, but this implies a larger deviation of the simulation from the measurements at τ = -5 fs. However, the overall agreement is improved.
It has to be stated that the absorption spectra can be mimicked by the simulation. We are able to qualitatively model the experimental results. However, there is no specific parameter set that can be assigned to describe the measurements for all time delays, but small variations of the parameters are required. Nevertheless, it is possible to reproduce the various details of the measured absorption spectra using our numerical model. With the chosen parameter sets, it is difficult to reconstruct the shoulder/peak at about 2.4 fs^{-1} and the minimum adjacent to it on the lower frequency side. A small minimum at $\omega \approx 2.35$ fs^{-1} can be included in the simulation, but the feature is much less pronounced than in the measurements.
In the future, several improvements of the simulation could be carried out in order to achieve an even better agreement with the experimental results. For instance, the damping and coupling constants could be chosen for each transition individually. Moreover, we could consider a change of the damping constant Γ with the intensity of the coupling laser pulse. The choice of transitions with a constant separation of 0.02 fs^{-1} only serves as simple model. To obtain a better agreement, much more details about the exact states and transitions (energies, their spacings, amplitudes and lifetimes) of the dye molecule IR144 need to be known. Since we have this information not available and we restrict ourselves to a toy model, a more detailed search for a suitable parameter set to achieve a quantitative description is not reasonable within the scope of this work. We do not seek to study the dye molecule IR144 specifically, but to understand the general physical mechanism on which the modifications of the absorption spectra are based. This is the aim of the developed numerical model. Further issues that are worth to give thought to are (i), which universal features can be identified when the absorption spectra are a superposition of spectrally close transitions, (ii) how differences or similarities of the couplings become manifest in the spectra and if they can be identified and (iii), whether it is possible to learn more from the line-shape modifications if additional information is taken into account that is derived from the spectra at positive time delays or from other spectroscopy measurements (e.g. 2D spectroscopy).

In summary, the key message is that we are able to qualitatively reproduce the measured absorption spectra and the occurring changes with a numerical model based on the Fano formalism discussed in section 4.1. The modifications of the absorption spectra with increasing pulse intensity can be attributed to changes of the absorption line profiles due to a laser-induced phase shift of the dipole response. Thus, the Fano concept that was originally developed for the case of gas-phase helium with single, well separated and spectrally narrow absorption lines can be transferred to larger systems like the complex dye molecule IR144 in liquid solution used in the presented measurements. Although the absorption lines are spectrally broad with small spectral separation or even overlap, the systems' response can be described by dipole oscillations whose phase is altered due to a laser-induced Stark shift. The imprinted phase leads to the modification of the absorption line shapes. However, there is a difference that has to be pointed out: In case of helium,

the laser pulse is very short compared to the decay time of the dipole response. Thus, the effect of the laser pulse can be regarded as "kick-like" and the phase shift is instantaneously induced at the beginning of the dipole response leading to an entire shift of the dipole oscillation. In case of the complex dye molecule, the laser-induced perturbation occurs on a similar time scale as the dipole response. Therefore, the variation of the absorption profile does not only consist of a single phase shift of the dipole response, but the modification persists even while the dipole oscillation decays.
Indeed, not all absorption lines are influenced by the presence of the pump laser pulse. As we demonstrated in this section, the observed changes of the IR144-absorption spectra can be explained by the coupling of single transitions to the laser field. The question why this is the case cannot be answered here and is left for future work. In particular, a much more detailed knowledge of the dye molecule IR144 and its molecular structure is necessary to carry out a quantitative analysis.
The important fact is that we showed the universal applicability of the Fano-phase formalism. The described simulation is not only applicable to the dye IR144. The numerical model can also be used to study other complex systems with a large number of transitions of finite widths where the overlap of these transitions leads to broad absorption peaks and modifications of single transitions cause variations affecting the entire absorption spectrum. Measurements in an analogous manner to the ones discussed could be performed and, if the energy-level structure of the system of interest is known, even a quantitative analysis with the help of the presented method might be carried out.

Chapter 5

Statistical phases in time-resolved spectroscopy

In the previous chapter we studied the dynamics of the dipole response after excitation by two time-delayed laser pulses in a small, atomic system, i.e. the rare gas helium, but also in a large, complex system, i.e. the dye molecule IR144. In both systems the dipole response can be controlled by the intensity of coupling laser pulses, which thus seems to be a universal physical phenomenon. The observed modifications of the absorption line profiles by increasing the intensity of the time-delayed second laser pulse could be assigned to an induced phase shift of the decaying dipole oscillation. The intensity of the coherent laser pulses serves as an effective control knob for the system's dipole response. In the helium experiments for instance, an initially absorptive behaviour was converted into an amplification of the light at the resonances. The intensity control of the coherent laser pulses provides direct access to the phases of quantum state coefficients.
In this chapter now, we want to focus on the laser pulse itself and the role played by its spectral phase in nonlinear time-resolved spectroscopy applications. Generally, noise is regarded as a nuisance. In experiments, it is usually a challenge to remove the possible sources for noise, be it the reduction of environmental electronic signals for example, in order to improve of the signal-to-noise ratio. According to traditional belief that for highest time resolution in experiments the shortest pulses are needed, particular technological emphasis was devoted to the generation of coherent laser pulses and the compensation ("linearization") of their spectral phase in order to achieve bandwidth-limited laser pulses. However, there are also major technical limitations due to the lack of suitable, chirp-compensating optics. Light sources were even developed which inherently deliver partially coherent, statistical laser pulses (cf. chapter 3.1.2). The question arises as to whether noise imprinted on the phase of laser pulses automatically implies drawbacks or if there are beneficial outcomes.
In section 5.1 the role of partially coherent lasers pulses in gas-phase pump–probe experiments and the discovered positive effect on the temporal resolution is discussed. The demonstration of the properties of statistical pulses is provided in section 5.2 where the second-harmonic generation process is investigated. The application to transient-absorption experiments in the liquid phase is presented in section 5.3 to confirm the generality of the physical mechanism.

5.1 Enhanced temporal resolution in pump–probe experiments

The aim to get access to the electron dynamics in atoms and molecules sets strong constraints on the properties of the laser pulses being used. Since the dynamics occur on extremely short time scales, i.e. in the femto- (10^{-15} s) or even attosecond (10^{-18} s) regime, a high temporal resolution is required which can only be achieved, following the commonly held belief, by extremely short pulses. For this purpose the laser pulses have to be spectrally very broad, but it is extremely difficult to compress these ultrabroad spectra to their bandwidth limit using the available dispersion-compensating optical devices (e.g. chirped mirrors). As will be shown below, statistical pulses, as they are delivered by Free-Electron Laser sources for instance, can provide an alternative route to resolve dynamics on ultrashort time scales. We developed a new method to enhance the temporal resolution in time-resolved spectroscopy by using statistical ("noisy") pulses. It needs to be emphasized that this concept is universal and applicable to a wide range of spectroscopy techniques, e.g. studying molecular or electronic dynamics, expanding it to non-optical spectroscopy techniques not only in physics, but also chemistry, life sciences or technology. In order to explain the general principle, an FEL pump–probe experiment studying the molecular wave-packet dynamics is picked exemplarily and presented in this section. The main results have already been published in [1] to which the following sections refer.

5.1.1 Wave-packet dynamics in D_2

The advantages of statistical pulses became apparent in the XUV-pump–XUV-probe experiment performed by Jiang et al. [40] at the Free-Electron Laser in Hamburg (FLASH). There, the sequential two-photon double ionization of D_2 molecules is studied using pulses at a photon energy of 38 eV (0.5 eV FWHM) with an average pulse duration of about 30 fs. A wave-packet dynamics on a time scale of 20 fs is discovered, although it is shorter than the average pulse duration.

A spherical mirror cut into two halves creates two identical copies, i.e. the pump and the probe pulse, out of each single FEL pulse and focuses them on the D_2 gas jet. By moving one of the mirror halves with a piezo stage the time delay between the pump and probe pulses can be adjusted (see Fig. 5.1). The created D^+ ions are detected by means of a position- and time-sensitive detector. From their time-of-flights and momentum distributions the kinetic-energy release (KER) is determined.

The underlying process in this pump–probe experiment is as follows: Due to the absorption of the first photon, the deuterium molecules are singly ionized to ${D_2}^+$. A nuclear wave packet evolves in the $1s\sigma_g$ state of the singly ionized molecule in the time before photon 2 is absorbed. The absorption of a second photon removes the remaining electron and the obtained ${D_2}^{2+}$ ions Coulomb explode and dissociate into two D^+ ions (see also Fig. 5.2). The kinetic energy of the detected ion, i.e. the KER, can be estimated by the energy difference $V(R) - V(\infty)$ of the dissociative $1/R$-potential curve as depicted in Fig. 5.2.

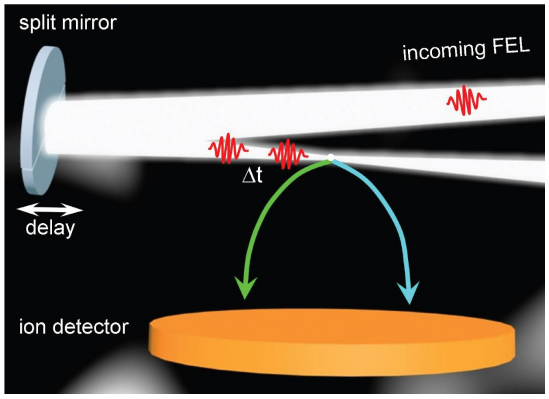

Figure 5.1: Sketch of the pump–probe experimental setup using Free-Electron Laser (FEL) pulses. Two identical copies of the incident FEL pulse are created and focused on the gas jet. The kinetic-energy release of the generated ions is detected as a function of the time delay between pump and probe pulse. Reprinted figure with permission from [116]. Copyright 2010 by the American Physical Society.

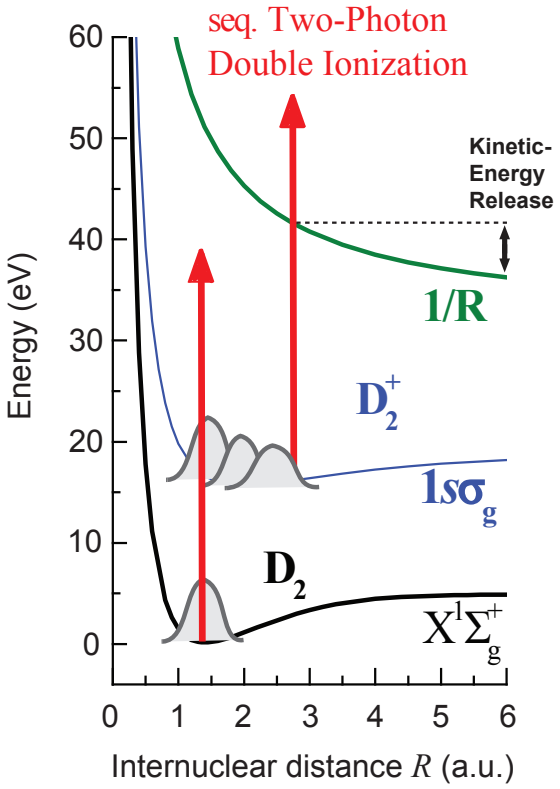

Figure 5.2: A schematic plot of the potential-energy curves of the D_2-molecule and its cations. The described two-photon double ionization (TPDI) process is indicated by red arrows. Figure adapted from [1].

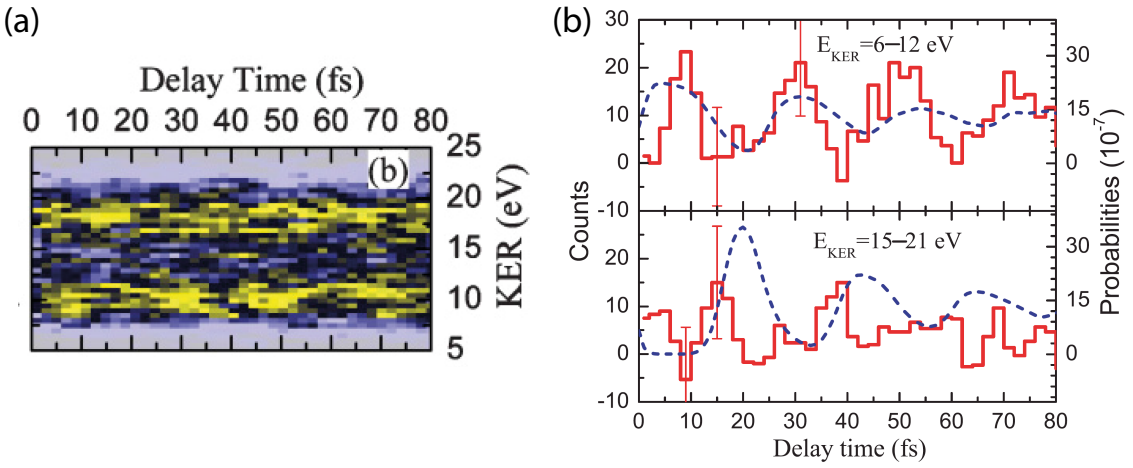

Figure 5.3: Measured kinetic-energy release distribution of the D^+ ions as a function of the time delay between pump and probe pulse (a) and integrated ion yield for the two different KER regimes $6-12$ eV and $15-21$ eV (b). An oscillation of the KER distribution (red curves) at a time scale of about 20 fs is obvious. The blue curves indicate the theoretical ionization probabilities. Reprinted figures with permission from [40]. Copyright 2010 by the American Physical Society.

The measured KER distribution of the deuterium ions vs. the pump–probe time delay is shown in Fig. 5.3(a) and covers a range of about $6-21$ eV. The kinetic-energy release of an ion depends on the time at which the D_2^+ is ionized. If it absorbs an additional photon when the nuclear wave packet is at the inner classical turning point (i.e. at small interatomic distance R), the KER is maximum and can be assigned to the range around 18 eV. If the wave packet reaches the outer turning point (i.e. large R) at the moment of ionization, the ion energy is minimum corresponding to the regime of approximately 9 eV. The ion yield integrated over the regimes of $6-12$ eV and $15-21$ eV, respectively, is displayed in Fig. 5.3(b). An oscillation is clearly visible and monitors the motion of the wave packet in the $1s\sigma_g$ state. The period of the dynamics amounts to 22 ± 4 fs [40]. This is a striking result. The average pulse duration is about 30 fs and thus dynamics occurring on shorter time scales should not be revealed as commonly assumed. How is it possible to achieve a better temporal resolution than given by the pulse duration? In order to answer this question we introduce a concept to reveal the influence of the statistical pulses and their properties on the experimental results. The numerical simulation is explained in the following.

5.1.2 Numerical simulation of FEL pulses

As a first step, a set of FEL pulses needs to be generated for the numerical simulation. Therefore, the so-called partial-coherence method (PCM) [117] is used which requires only two parameters that are both accessible in the experiment: the average spectrum $\overline{I}(\omega)$ and the average pulse duration t_{pulse}.

To construct the electric field of the FEL pulses the measured spectrum $\overline{I}(\omega)$ is discretized into sampling points ω_i, where $|\omega_i-\omega_{i+1}|\ll 2\pi/t_{\text{pulse}}$. The spectral amplitude is derived by $\overline{A}(\omega_i)=\sqrt{\overline{I}(\omega_i)}$ and for each spectral component ω_i a random phase $\phi(\omega_i)$

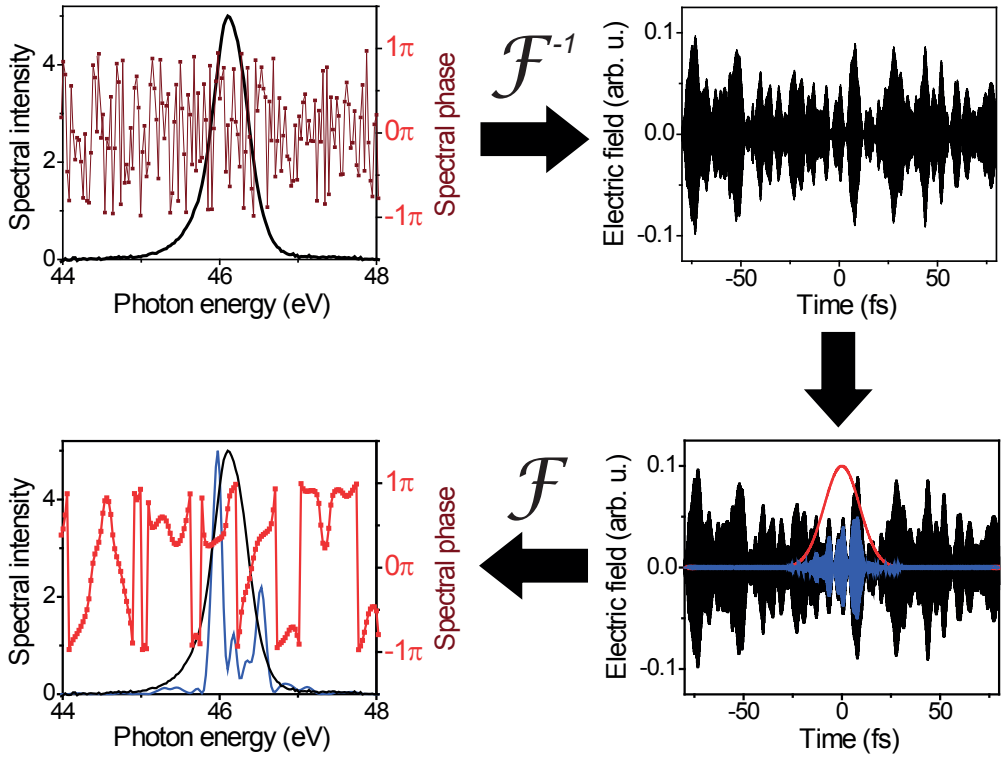

Figure 5.4: Illustration of the partial-coherence method. Upper left panel: An experimental average spectrum (black curve) and the corresponding set of random phases (red curve). Upper right panel: Conversion of the spectral field $\widetilde{E}(\omega_i) = \overline{A}(\omega_i) \cdot \exp(i\,\phi(\omega_i))$ into a temporal electric field $E(t)$ via Fourier transform. Lower right panel: Multiplication with a temporal Gaussian filter $F_G(t)$ (red curve) that accounts for the average pulse duration yields the final electric field of an FEL pulse $E_{FEL}(t)$ (blue curve). Lower left panel: The inverse Fourier transform reveals the spectrum (blue curve) and the partially coherent phase (red curve) of a single FEL pulse. The average of many such spectra reproduces the measured average spectrum (black curve).

between 0 and 2π is chosen, so that an electric field $\widetilde{E}(\omega_i) = \overline{A}(\omega_i) \cdot \exp[i\,\phi(\omega_i)]$ is obtained. Figure 5.4, upper left panel, shows an exemplary spectrum and a set of random phases. The electric field in the time domain is calculated by the Fourier transform $E(t) = \mathscr{F}^{-1}\left\{\widetilde{E}(\omega)\right\}$. Due to the initially random phase the temporal electric field is infinitely long (Fig. 5.4, upper right panel). A Gaussian envelope filter function, $F_G(t)$, whose width corresponds to t_{pulse} is multiplied and yields the final electric field of an FEL pulse $E_{FEL}(t)$ (see Fig. 5.4, lower right panel):

$$\begin{aligned} E_{FEL}(t) &= F_G(t) \cdot E(t) \\ &= \frac{1}{2\pi} \int_{-\infty}^{\infty} d\omega A_G(\omega) e^{i\omega t} \cdot \int_{-\infty}^{\infty} d\omega \overline{A}(\omega) e^{i\phi(\omega)} e^{i\omega t}. \end{aligned} \tag{5.1}$$

The inverse Fourier transform $\mathscr{F}\{F_G(t) \cdot E(t)\}$ gives the spectrum and the phase of one single pulse (cf. Fig. 5.4, lower left panel). The spectral phase is not arbitrary anymore, revealing a characteristics of FEL pulses, namely their partial coherence. For each single FEL pulse a new set of random initial phases is chosen so that after Fourier transform and temporal filtering the pulse shape and its corresponding spectrum and spectral phase

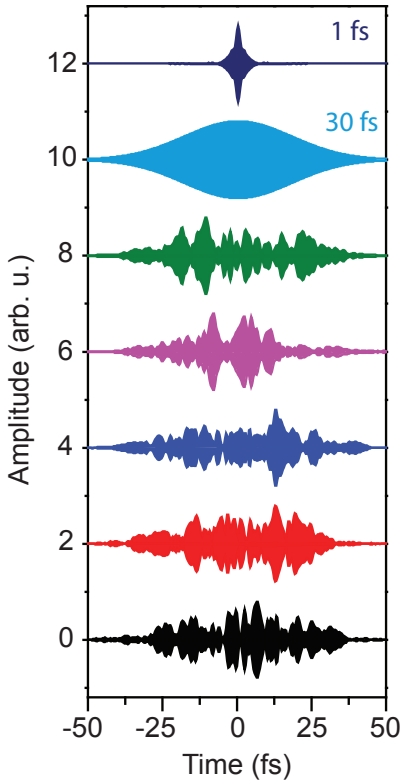

Figure 5.5: A set of temporal FEL pulse shapes generated by the partial-coherence method described in the text and the pulse shapes of a very short 1.12 fs and a Gaussian bandwidth-limited 30 fs pulse. Figure adapted from [1].

will vary. However, the average spectrum of many pulses that are derived in the manner specified yields the measured average spectrum.

A set of 2000 FEL pulses is generated for the simulation taking the average spectrum of the D_2 experiment into account. The width of the Gaussian temporal filter, $F_G(t)$, is chosen such that it matches the measured average pulse duration of 30 fs. The results are compared to the case of a bandwidth-limited Gaussian pulse, $E_G(t)$, with a pulse duration of 30 fs FWHM:

$$E_G(t) = \frac{1}{\sqrt{2\pi}} \int_{-\infty}^{\infty} d\omega A_G(\omega) e^{i\omega t}. \tag{5.2}$$

Furthermore, a 1.12 fs short pulse, $E_{short}(t)$, corresponding to the bandwidth limit of the experimental average spectrum, $\overline{A}(\omega) = \sqrt{\overline{I}(\omega)}$, is also considered where its pulse duration represents the coherence time of the FEL pulses:

$$E_{short}(t) = \frac{1}{\sqrt{2\pi}} \int_{-\infty}^{\infty} d\omega \overline{A}(\omega) e^{i\omega t}. \tag{5.3}$$

The temporal pulse shapes of the short pulse, of the Gaussian pulse and of five FEL pulses produced via the PCM are displayed in Fig. 5.5.

5.1.3 Modeling the wave-packet dynamics

As a second step, the pump–probe light-matter interaction experiment is modeled. For this purpose we try to keep the model as simple as possible, but nevertheless to include all necessary ingredients. The D_2 molecules in the laser focus experience the superposition of the XUV-electric fields of the pump and the time-delayed probe pulse. As the two laser pulses are derived out of the same FEL beam, the intensity in the interaction region is given by

$$I_\tau(t) = |E_{\mathrm{FEL}}(t) + E_{\mathrm{FEL}}(t+\tau)|^2 , \tag{5.4}$$

where the index τ denotes the dependence on the time delay between pump and probe.

The molecules can absorb the two photons that lead to the dissociation at any time, for instance the first photon is absorbed at time t' and the second photon at t''. Due to the high photon energy of 38 eV the first absorption step ionizes the D_2 molecule into a continuum which is far away from bound-state resonances. This is the reason why we can develop a rate-equation model which is frequency independent to describe the ionization process. The rates to generate singly and doubly ionized ions are proportional to the intensity $I_\tau(t)$ and given by

$$\frac{dN_1}{dt} \propto N_0 \cdot I_\tau(t) \quad \text{and} \quad \frac{dN_2}{dt} \propto N_1(t) \cdot I_\tau(t) \tag{5.5}$$

with the number of singly ionized D_2^+ molecules, N_1, and of doubly ionized D_2^{2+} molecules, N_2. Integration and combination of the equations yields

$$N_1(t) \propto N_0 \int_{-\infty}^{t} dt'\, I_\tau(t') \tag{5.6}$$

and

$$N_{2,\infty} = N_{\mathrm{tot}} \propto \int_{-\infty}^{\infty} dt'\, N_1(t')\, I_\tau(t') = \int_{-\infty}^{\infty} dt'' \int_{-\infty}^{t''} dt'\, I_\tau(t')\, I_\tau(t''). \tag{5.7}$$

If we introduce the time difference $t_c = t'' - t'$ between the absorption of photon 1 and photon 2, substitute variables and swap the integration order, the result for the number of doubly ionized molecules reads as

$$\begin{aligned} N_{\mathrm{tot}}(\tau) &\propto \int_0^{\infty} dt_c \int_{-\infty}^{\infty} dt''\, I_\tau(t'' - t_c) I_\tau(t'') \\ &= \int_0^{\infty} dt_c\, A_c^{(2)}(t_c, \tau). \end{aligned} \tag{5.8}$$

The expression $A_c^{(2)}(t_c, \tau) = \int_{-\infty}^{\infty} dt\, I_\tau(t) \cdot I_\tau(t - t_c)$ is the two-dimensional autocorrelation (2DAC) function with the correlation time t_c. It is an intensity autocorrelation of two identical pulses as function of the time delay τ. The 2DAC is a general function describing the properties and structure of the probing light field. It is not only suitable for laser light in the XUV, but can be applied for fields in any spectral region.

So far, only the physical description of the probing light field is included. The physical information about the system that is studied is still missing. For the chosen pump–probe experiment the situation is as follows: When the deuterium molecule absorbs the first photon, one electron is removed, i.e. it is singly ionized. A molecular wave packet is created and oscillates in the $1s\sigma_g$ state of the $D_2{}^+$ molecule. The second photon fully ionizes the molecule and the produced $D_2{}^{2+}$ ions Coulomb explode. Depending on the time when photon 2 is absorbed the wave packet is located at different internuclear distances R and hence the measured kinetic-energy release of the D^+ ions varies.

Therefore, the molecular dynamics that has to be modeled is the evolution of the nuclear wave packet in the $1s\sigma_g$ state. This is done by introducing the so-called molecular response function $M(E_{\mathrm{KER}}, t_{\mathrm{c}})$. It maps the waiting time t_{c} between the two absorbed photons to a kinetic-energy release distribution of the produced D^+ ions. Inserting the derived molecular response function finally gives for the number of doubly ionized molecules as a function of the pump–probe time delay τ and the KER E_{KER}:

$$N(E_{\mathrm{KER}}, \tau) \propto \int_0^\infty dt_{\mathrm{c}}\, M(E_{\mathrm{KER}}, t_{\mathrm{c}})\, A_{\mathrm{c}}^{(2)}(t_{\mathrm{c}}, \tau). \tag{5.9}$$

It has to be pointed out that this expression for $N(E_{\mathrm{KER}}, \tau)$ is universal and not restricted to the scenario discussed in this section, but is applicable to any pump–probe experiment. The response function can be calculated so that it matches and describes the given physical properties and dynamics of the system under investigation.

The obtained autocorrelation functions are shown in Fig. 5.6. If the pump and probe beams propagate collinearly, optical-cycle interferences occur. As the two beams overlap at some angle in the experiment, these interferences are washed out. Therefore, in the numerical simulation we convolute the calculated autocorrelation functions along the time-delay axis with a Gaussian function whose temporal width is in the range of one optical cycle. The 2DACs for the short 1.12 fs and the long 30 fs bandwidth-limited pulses are displayed in Fig. 5.6(a) and (b). In the first case, three narrow lines are visible. The width of these lines (which corresponds to the coherence time) and the time delay τ at which the three peaks can be separated along t_{c} determine the possible temporal resolution. For the 30 fs long Gaussian pulse, the three lines are broad leading to an accordingly limited time resolution. Figure 5.6(c) presents the 2DAC function for a statistical average over a set of 2000 FEL pulses that were generated as explained in the previous section 5.1.2. Here, broad pedestals appear, but with narrow features sitting on top of the broad lines. These narrow lines cause the enhancement of the time resolution in comparison to the bandwidth-limited 30 fs pulses. For a better visibility, a lineout at $\tau = 100$ fs for each of the pulse types is plotted in Fig. 5.6(d). There is also a physical interpretation of the main peak at $t_{\mathrm{c}} = 0$ fs and the smaller peaks at $t_{\mathrm{c}} = \tau$: The center peak corresponds to the scenario that the two photons originate from the same pulse (either pump or probe) and the side peaks belong to the case that the photons are absorbed in different pulses.
In Fig. 5.6 the number of doubly ionized molecules, N_{tot}, as described by equation (5.8) is also displayed. The enhanced signal at small τ is visible for the FEL case which is consistent with earlier experiments [116].

Figure 5.7(a) represents the evolution of the nuclear wave packet $|\Psi(R, t_c)|^2$ as a function

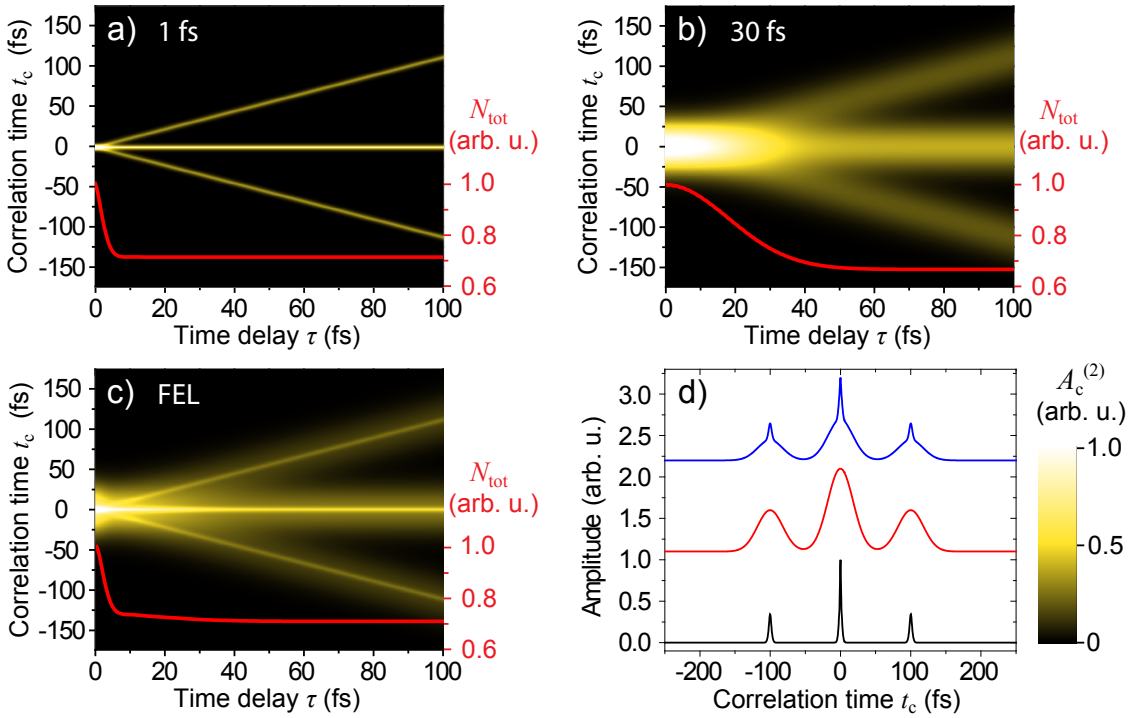

Figure 5.6: Calculated two-dimensional autocorrelation functions $A_c^{(2)}(t_c,\tau)$: (a) for 1.12 fs bandwidth-limited pulses derived from the average FEL spectrum, (b) for 30 fs bandwidth-limited Gaussian pulses and (c) for an average over 2000 statistical FEL pulses. The red curves depict the number of doubly ionized molecules N_{tot}. (d) Lineouts of the 2DAC at $\tau = 100$ fs for the 1.12 fs (black), the 30 fs (red) and the FEL pulses (blue). Figure adapted from [1].

of time after ionization. The wave packet $\Psi(R,t_c)$ is calculated by solving the time-dependent Schrödinger equation with a split-step operator method [118–120]. The initial condition is set so that $\Psi(R,t_c)$ equals the stationary ground-state wave function of the D_2 molecule. The final response function is obtained by converting the internuclear distance R to the kinetic-energy release via the Coulomb-explosion mechanism [121], i.e. $E_{KER} = 1/R$. The oscillatory motion of the wave packet with a period of about 20 fs is clearly visible.

The KER distributions of the D^+ ions derived by equation (5.9) are shown in Fig. 5.7. As expected, the 30 fs long pulse washed out all dynamics so that no oscillation of the ion yield appears (Fig. 5.7(c)). In contrast, the wave-packet dynamics is unambiguously revealed in the case of the very short pulse (Fig. 5.7(b)). However, the result for the average over many statistically varying FEL pulses is surprising. Even though the average pulse duration amounts to 30 fs, the wave-packet oscillation can be identified (see Fig. 5.7(d)). It becomes even more clear by Fourier filtering the KER-vs.-τ trace of the averaged FEL pulses: A Fourier transform is taken along the time-delay axis (cf. Fig. 5.8(a)), the DC peak is removed and after the inverse transform the wave-packet motion is uncovered as it is displayed in Fig. 5.8(b). The obtained KER distribution is very similar to the expected result for the 1.12 fs pulse (cf. Fig. 5.7(b)). Here, it needs to be stressed again that the time resolution is enhanced for the FEL pulses, because the intensity subspikes of the pump and probe beam (which are identical copies) are temporally correlated. The high temporal

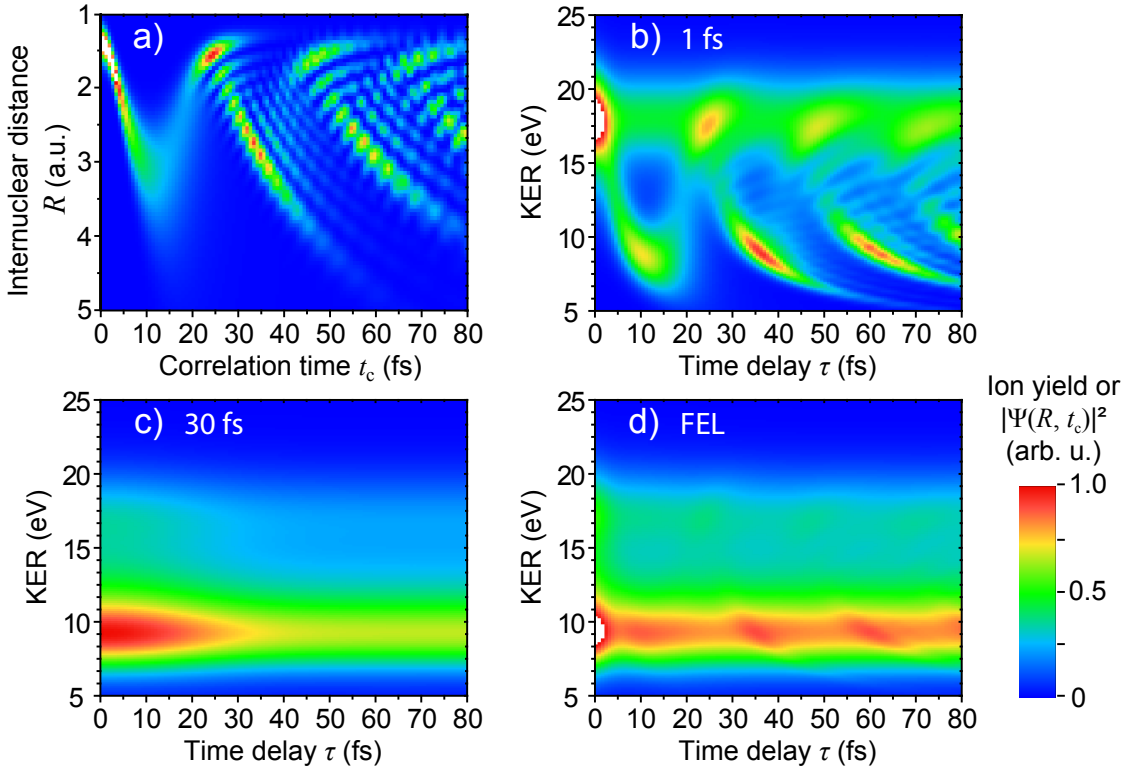

Figure 5.7: Molecular wave-packet dynamics. (a) Evolution of the nuclear wave packet $|\Psi(R,t_c)|^2$ in the $1s\sigma_g$ state as a function of time after ionization. (b) - (d): The kinetic-energy release distribution of the doubly ionized molecules as given by equation (5.9) for 1.12 fs coherence-time limited pulses, 30 fs bandwidth-limited Gaussian pulses and an average over 2000 FEL pulses. Figure adapted from [1].

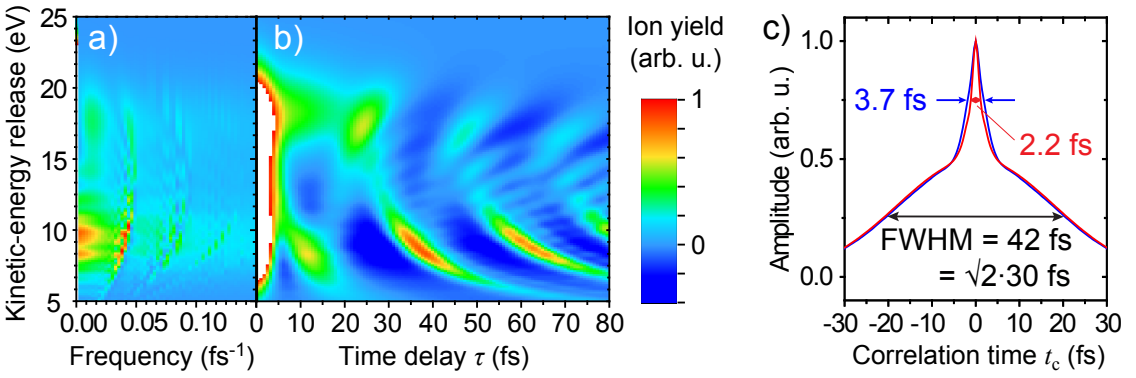

Figure 5.8: Temporal resolution. (a) Fourier transform of the KER distribution for the set of FEL pulses (cf. Fig. 5.7(d)). (b) KER-vs.-τ trace after Fourier filtering clearly resolving the molecular wave-packet dynamics. (c) Comparing the $A_c^{(2)}(t_c,\tau)$: the main peak at $t_c = 0$ fs for the FEL pulses (blue curve) and for the sum of the 1.12 fs short and 30 fs pulse (red curve) at $\tau = 100$ fs. Figure adapted from [1].

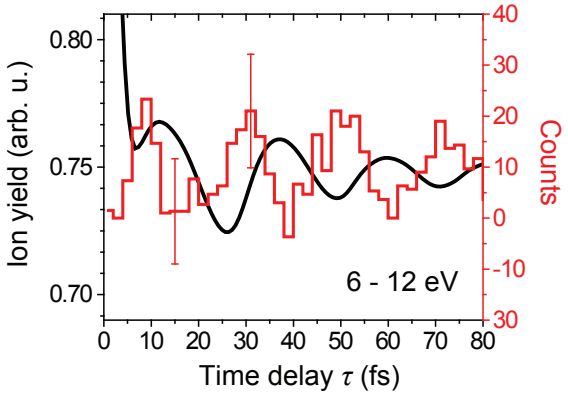

Figure 5.9: Ion yields as a function of delay time reflecting the wave-packet dynamics. The simulation result (black curve), i.e. the integration of the KER distribution over $6 - 12$ eV (see Fig. 5.7(d)), reveals an oscillatory dynamics with a period of 23 ± 1 fs. The experimentally measured ion yield (taken from [40]) is displayed in red for comparison. Figure adapted from [1], supplemental material.

accuracy achieved can also be explained by comparing the center peak of the 2DAC function for the FEL pulses and for the sum of the very short and the 30 fs bandwidth-limited pulse as indicated in Fig. 5.8(c) at a time delay $\tau = 100$ fs. The width of the pedestal in the intensity autocorrelation matches the average pulse duration via 42 fs $= \sqrt{2} \cdot 30$ fs (cf. the theoretical derivation in section 2.2). The autocorrelation of the FEL pulses exhibits a slightly larger width of the narrow spike compared to the 2DAC sum of the 1.12 fs and 30 fs pulse. This means that the noisy FEL pulses provide a time resolution that is slightly reduced. Anyhow, the temporal resolution is a factor of 10 better than in the case of the 30 fs bandwidth-limited pulse.

Two further remarks should be added when comparing simulation to experiment. From the FEL kinetic-energy distribution of the D^+ ions, we can determine the oscillation period of the molecular wave packet. The ion yield depicted in Fig. 5.7(d) is integrated over the KER range of $6 - 12$ eV and shown in Fig. 5.9. We find an oscillation period of 23 ± 1 fs for the numerical model which is in very good agreement to the experimental period of 22 ± 4 fs [40]. The shift along the time-delay axis between experiment and simulation can be explained since the zero time delay is often difficult to determine experimentally.

Moreover, the kinetic-energy release signal in the regime $15 - 21$ eV is underestimated in the numerical simulation. First of all, we restrict ourselves to the sequential TPDI process, neglecting the direct two-photon double ionization which would contribute at higher KER. Secondly, we assume a constant cross section of the second ionization step ($D_2^+ \longrightarrow D_2^{2+}$), disregarding the fact that it is dependent on the internuclear distance R.

5.1.4 The influence of statistics

This subsection investigates the influence of statistics on the numerical results presented in the previous sections and the experimental measurements.

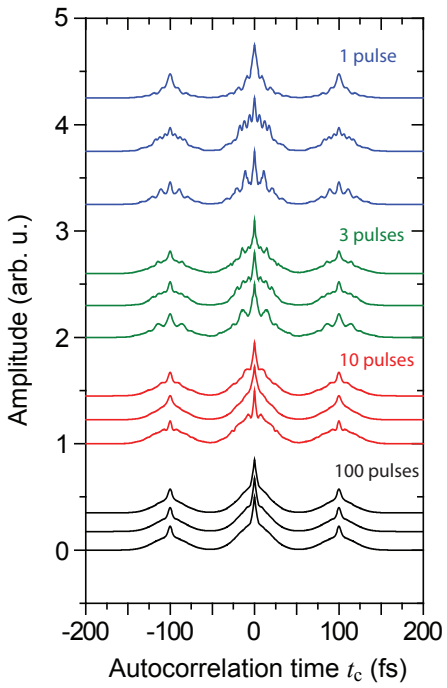

Figure 5.10: Influence of statistics on the two-dimensional autocorrelation. Lineouts at a time delay of 100 fs for averages over $N = 1$, 3, 10 and 100 FEL pulses, three different averages for each N. For small N several side peaks appear randomly distributed. The 2DAC shape corresponds more and more to the known structure of a narrow spike sitting on top of the broader pedestals with increasing number N. Figure adapted from [1], supplemental material.

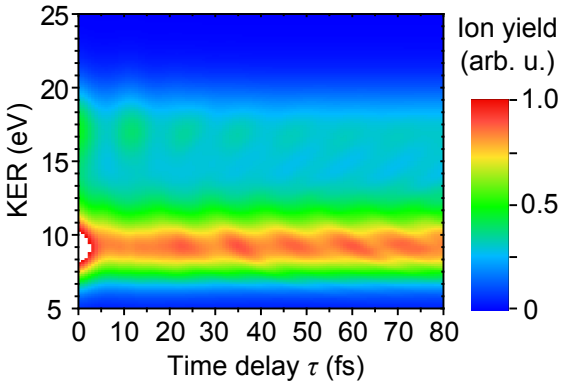

Figure 5.11: Simulated kinetic-energy release distribution for one single FEL pulse. The various side peaks in the 2DAC lead to artefacts that in this case falsely represent oscillatory dynamics on a faster time scale than the actual vibrational period.

First, we examine the role of the statistically fluctuating FEL pulses in our method. As indicated before, Figs. 5.6(c) and 5.7(d) are obtained for an average of 2000 FEL pulses. How do the results depend on the size of the used set of FEL pulses? In order to find an answer the two-dimensional autocorrelation function $A_c^{(2)}(t_c, \tau)$ is calculated for averages over different numbers N of noisy FEL pulses. The lineouts at a time delay $\tau = 100$ fs for one single pulse and an average over 3, 10 and 100, respectively, FEL pulses are presented in Fig. 5.10. For each set three different averages are plotted. The common features of these lineouts are the narrow spikes sitting on top of the broader pedestals. The width and the amplitude of these spikes determines the time resolution. However, for small numbers N the averaged 2DAC features in addition a lot of randomly distributed spikes. Furthermore, the number, amplitudes and positions of these extra spikes vary for the different averages of a fixed number of FEL pulses. These side peaks are artefacts containing no physical information. A KER-vs.-τ distribution calculated for one single FEL pulse is displayed in Fig. 5.11. It seems as if the molecular wave-packet oscillation period amounts to roughly 10 fs, but the structure observed stems from the statistical nature of the FEL pulses and it would look different if another FEL pulse was used. Thus, the averaging over a large statistical set of FEL pulses is essential to obtain a physically meaningful result. The additional peaks disappear when the number of averaged pulses is increased and the shape of the 2DAC finally corresponds to the already known (Fig. 5.6(d)). The maximum temporal resolution is achieved if only the central spikes on each pedestal remain. A sufficient number of pulses seems to be $N = 100$ for the experiment modeled in this section. For another experiment with different average spectrum and average pulse duration the number N may differ and has to be determined again.

As second aspect, we study how the experimental count statistics affects the measured KER distribution and with which quality the wave-packet motion can be identified. For this purpose, we modeled the KER-vs.-τ diagrams with a Poissonian counting statistics and Fourier filtered them (in the same way as described in the previous section 5.1.3) in order to reveal the molecular wave-packet dynamics. As total count numbers $4.5 \cdot 10^5$, $9 \cdot 10^5$, $1.8 \cdot 10^6$ and $4.5 \cdot 10^6$ are chosen. Figure 5.12 shows the obtained KER traces. As it can be clearly seen, the larger the total number of counts the better the wave-packet dynamics is resolved which is the case for $4.5 \cdot 10^6$ counts. For low count numbers the oscillation is hardly distinguishable. So, a minimum level of count statistics is necessary in the experiment to reveal the molecular dynamics.

5.1.5 Resolution limit at ultrashort time scales

As mentioned before, the scheme of noise-enhanced temporal resolution presented in detail herein is not restricted to pump–probe spectroscopy using Free-Electron Laser pulses. The universality of equation (5.9) permits to apply the method to a variety of experiments. As possible further application, this section briefly addresses attosecond pump–probe experiments. The dynamics of deeply-bound electrons in atoms and molecules happens on the order of attoseconds. Pump–probe spectroscopy using attosecond pulses would pave the way to study sequential electron dynamics on its natural time scales. Recently, a first proof-of-principle experiment was performed [122]. The pulses created by high-harmonic generation have an extremely broad spectrum, but there is no experimental means to com-

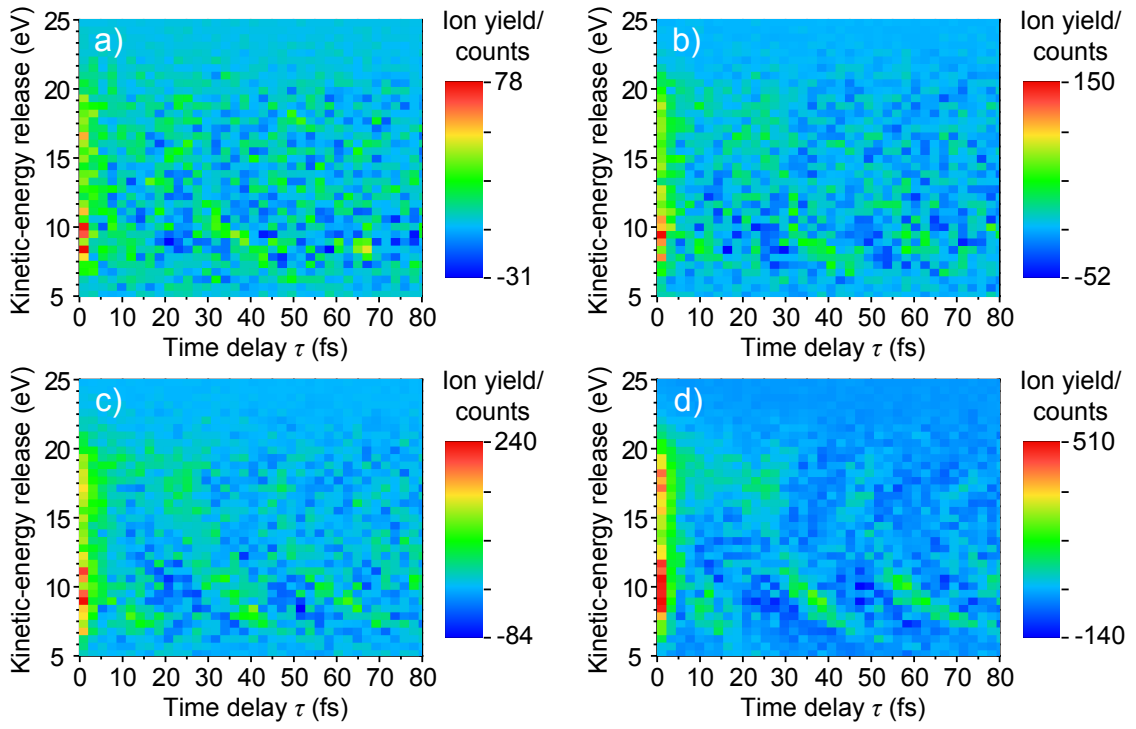

Figure 5.12: Influence of random Poissonian (counting) statistics on the experimental result. The Fourier filtered KER distributions are numerically simulated for a total number of $4.5 \cdot 10^5$ (a), $9 \cdot 10^5$ (b), $1.8 \cdot 10^6$ (c) and $4.5 \cdot 10^6$ counts (d). Figure adapted from [1], supplemental material.

press these spectra to their bandwidth limit. The remaining chirp limits the pulse lengths to a few hundred attoseconds. Therefore, the "noisy-pulse concept" might allow to reach the limit of highest resolution on the atomic-unit time scale.

Again, a numerical simulation is performed in which the amount of noise imprinted on the phase is varied and its implications are studied. We assume that an infrared laser pulse with a pulse duration of 5 fs FWHM, a peak electric field of 0.2 a.u. and a central wavelength of 800 nm generates an isolated attosecond pulse. The bandwidth limit of the attosecond pulse is approximately 0.8 a.u. ($\approx$ 19 as), but due to chirp the actual pulse length amounts to 9 a.u. ($\approx$ 220 as) FWHM. The calculation of the statistically fluctuating pulses and the 2DAC function is carried out as demonstrated in subsections 5.1.2 and 5.1.3. The attosceond pulse spectrum is resampled in frequency steps of 0.2 fs^{-1} and a random phase between 0 and x is assigned to each frequency component. Four cases are analyzed: $x = 0.2\pi, 0.6\pi, 1.4\pi$ and 2π. An average pulse duration of 600 as is implemented via the Gaussian filter function F_G. Figure 5.13 illustrates the lineouts of the resulting $A_\text{c}^{(2)}(t_\text{c}, \tau)$ at a time delay $\tau = 60$ a.u.. For a maximum random amplitude of the added noise ($x = 2\pi$) the features are the same as in the case of FEL pulses: Very narrow peaks are located on top of the broad pedestals. The width of the pedestals is consistent with the average attosecond pulse duration of 600 as. The narrow spikes have a width of about 1.5 a.u. ($\approx$ 36 as) which corresponds to a pulse duration of 25 as. Thus, the achievable temporal resolution is extremely close to the bandwidth limit (which is not possible to be realized in the experiment). However, it has to be noted that there is a critical amount of noise below which no enhanced time resolution occurs. For decreasing x the spikes be-

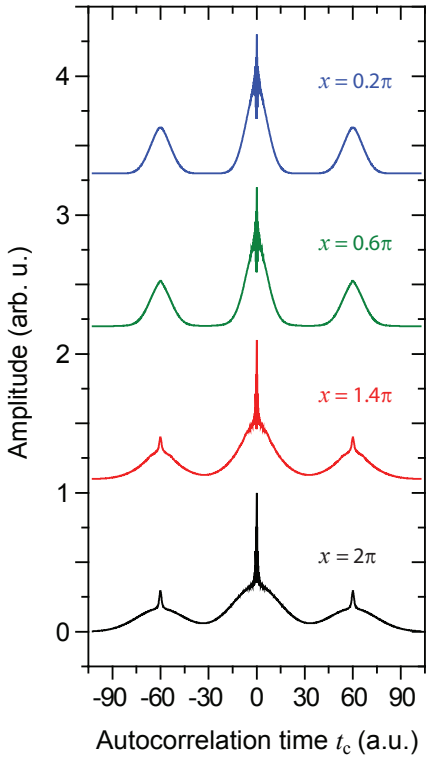

Figure 5.13: Two-dimensional autocorrelation function at a time delay $\tau = 60$ a.u. for attosecond pulses with noise added to their spectral phase. The amount of noise x is changed from 0.2π (blue line) over 0.6π (green line) and 1.4π (red line) to 2π (black line). Figure adapted from [1], supplemental material.

come smaller and disappear. For $x = 0.2\pi$ the shape of the 2DAC function resembles the case of a 220 as pulse so that the pulses can be considered as almost fully coherent. For $x = 0.6\pi$ the shape of the pedestal seems to be triangular. In this regime of x the transition from the coherent to the statistically fluctuating case can be identified and the critical value is close to $x_c = 1.4\pi$. This numerical simulation demonstrates that the noisy-pulses scheme would have a strong impact on attosecond pump–probe spectroscopy, pushing the limit of temporal resolution far down to the atomic-unit scale. Furthermore, this method is applicable to attosecond pulses irrespective of their chirp and thus very robust.

A short comment on the question how to imprint the additional noise on the spectral phase of the attosecond pulses: Possible realizations could be multilayer-nanofluidic mirrors. Depending on the penetration depth into the mirror the spectral components would be randomly delayed or phased. Another option would be non-stationary mirrors exhibiting a rough surface.

The presented concept of statistically varying the spectral phases of light pulses is an excellent alternative to attain resolution on ultrashort time scales. It has a wide applicability for nonlinear spectroscopy in physics and chemistry and even for processes in biology, life sciences and communication technology when noisy signal sources play a role.

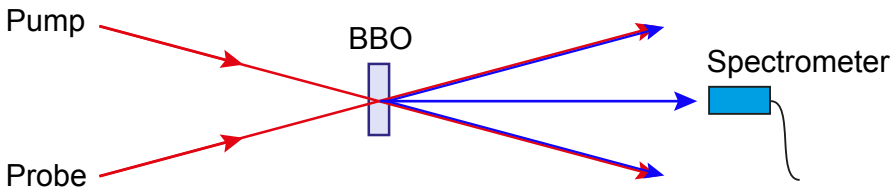

Figure 5.14: Sketch of the beam configuration of the SHG measurements. The non-collinear pump and probe beams (red arrows) are focused into a frequency-doubling BBO crystal. Each single beam creates second-harmonic light (blue arrows) in beam direction. However, only if the pump and probe pulses overlap in time second-harmonic light is emitted into the center direction and detected by a spectrometer.

5.2 Table-top noisy-pulse experiments

Free-Electron Lasers provide statistically fluctuating (noisy) pulse shapes, however, beam-time availability is very limited. There are a lot of proposals for experiments at these research facilities, but only a few are accepted. It would be a great advantage if such noisy pulses could be produced in the own laboratory. Moreover, the generation of statistical pulses not only in the X-ray, but different wavelength ranges (like the visible or infrared) would offer applications in a variety of experiments. Therefore, the idea is to use the pulse shaper (as described in chapter 3.3.2) to create noisy pulses in the visible to infrared regime in our lab.

As discussed in the previous section 5.1, the autocorrelation function of statistically varying pulses is characterized by a narrow spike sitting on top of a broad pedestal (cf. Fig. 5.8(c)). The width of the narrow feature reveals the bandwidth limit provided by the laser spectrum, whereas the width of the pedestal corresponds to the average pulse duration. In order to check the successful phase-modulation of the laser pulses in our lab, the intensity autocorrelation needs to be determined. Such an autocorrelation can be realized by a two-photon process like second-harmonic generation (cf. chapter 2.2). The shaped laser pulses enter the transient-absorption setup where two identical beams, the pump and probe pulse, are created by the four-hole mask as described in chapter 3.3. The two beams are focused into a frequency-doubling BBO crystal (thickness: 300 µm). Figure 5.14 shows a schematic of the beam configuration. Since pump and probe beam do not propagate collinearly, but are combined under an angle, second-harmonic light will be emitted in three directions. SHG light generated by each single beam propagating in beam direction only gives an offset contribution. The crucial contribution to the frequency-doubled light stems from the temporal (and of course spatial) overlap of the pump and probe beam and propagates in the center direction between pump and probe. The generated second-harmonic light depends on the pump–probe time delay and detecting the SHG spectrum as a function of the time delay τ provides the intensity autocorrelation of the shaped pulses.

The pulse shaper introduced in chapter 3.3.2 is used to create the statistically fluctuating pulse shapes. The procedure is the same as in the simulation of the FEL pulses which is described in section 5.1.2. To each frequency component of the spectrum, a random phase between 0 and 2π is assigned. A LabView program performs a Fourier transform into the

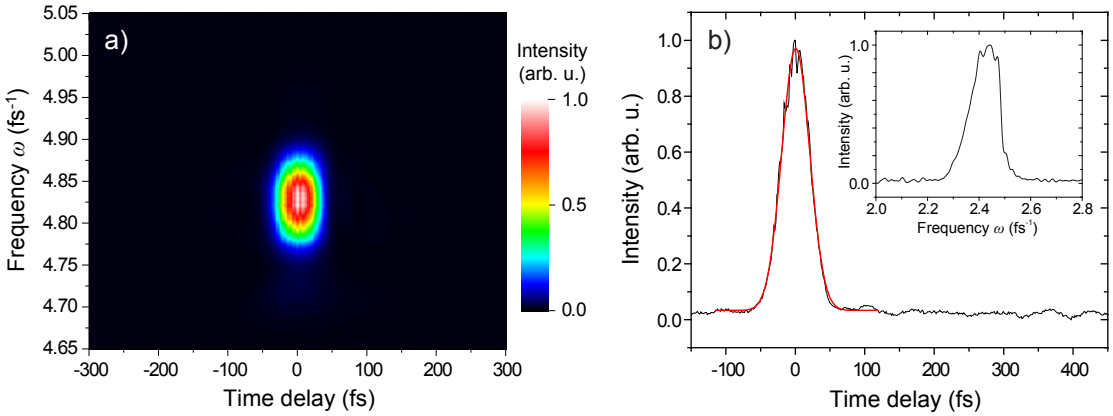

Figure 5.15: Measured second-harmonic light for bandwidth-limited pulses. (a) Two-dimensional plot of the measured SHG spectra (emitted in center direction, cf. Fig. 5.14) as a function of the time delay between pump and probe beam. (b) SHG light integrated over frequency versus time delay. The determined FWHM of about 48 fs corresponds to a pulse duration of about 34 fs of the bandwidth-limited pulses. The Gaussian fit is indicated in red. The inset shows the measured laser spectrum.

time domain. A Gaussian function as envelope whose width determines the average pulse duration of the noisy pulses is multiplied to the obtained electric field. The inverse Fourier transform provides the spectrum and the partially coherent phase of a single pulse. This phase is applied to the LC-display of the spatial light modulator. The partially coherent phases are calculated in an infinite loop and applied to the display at a rate of 4 Hz, i.e. each 250 ms the phase pattern is changed. In our case only the phase, but not the amplitude is modified by the pulse shaper.

In the experiment, the time delay between pump and probe pulse is scanned and the frequency doubled light is detected by a spectrometer (USB4000, Ocean Optics). In the case of statistically fluctuating pulses, the scan is repeated several times. The measured results for transform-limited pulses, i.e. no phase pattern was applied to the LCD, and for an average of 15 scans with statistically varying pulses are displayed in Fig. 5.15 and Fig. 5.16, respectively. The second-order autocorrelation reveals a pulse duration of about 34 fs $\approx 48\,\text{fs}/\sqrt{2}$. The autocorrelation obtained for the noisy pulses has the known characteristic structure: a narrow peak on top of a broad pedestal. The FWHM of the narrow feature of $\sim$47 fs corresponding to a bandwidth limit of $\sim$33 fs is in excellent agreement with the transform-limited case. The average pulse duration can be derived and amounts to approximately 262 fs $\approx 370\,\text{fs}/\sqrt{2}$. This is in the range of the chosen width of about 230 fs of the Gaussian envelope used in the partial-coherence algorithm to construct the noisy pulses. The deviation might stem from the discretization of the LCD pixels and also from the presence of a spatial chirp. The errors of the determined autocorrelation widths are on the order of 1 – 2 fs in the bandwidth-limited case and about 5 fs in the case of noisy pulses.
The measured second-order autocorrelation and its characteristic features are in excellent agreement with the results obtained using FEL pulses (cf. section 5.1). This is a clear signature that partially coherent pulses can be produced in the table-top setting of our lab.

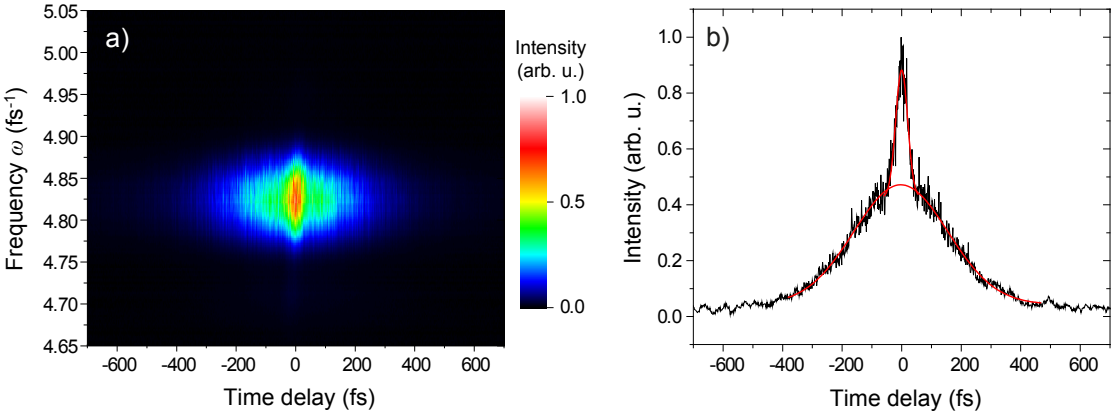

Figure 5.16: Measured second-harmonic light for partially coherent (noisy) pulses. (a) 2D plot of the detected SHG spectra versus the time delay τ. An average over 15 measurements is taken. (b) Integrated second-harmonic light depending on the pump–probe time delay. The narrow spike sitting on top of the broader pedestal is clearly visible. The narrow spike has a FWHM of ∼47 fs representing the bandwidth limit of about 33 fs. The width of the broader pedestal of approximately 370 fs reveals the average pulse duration of the generated statistically varying laser pulses of about 262 fs. The Gaussian fits are indicated in red.

In order to test the measurement results, a simulation is carried out. Starting from the spectrum of the pulses (either mimicked by a Gaussian function or taking the measured laser spectrum) and the applied phase, the electric field is calculated by a Fourier transform. Then, the electric fields of the pump and time-delayed probe pulse are superposed yielding the total electric field $\widetilde{E}(t)+\widetilde{E}(t-\tau)$. The frequency-doubling is realized in the simulation by taking the square, i.e. the term $e^{i2\omega t}$ appears. The inverse Fourier transform yields the SHG spectrum where only the contribution depending on the time delay τ is considered. In the case of statistically fluctuating pulses, an average of 100 scans is taken.

In a first simulation, the widths and pulse durations obtained in the measurements are inserted as parameters. The calculated spectra are shown in Fig. 5.17. As laser spectrum a Gaussian distribution with a center frequency of 2.415 fs^{-1} is chosen. The simulation reproduces the measurements exactly for both cases. In the transform-limited case, the width of the distribution reveals a pulse duration of about 33 fs ≈ 47 fs$/\sqrt{2}$. In case of noisy pulses, the determined time scales are approximately 35 fs ≈ 50 fs$/\sqrt{2}$ for the bandwidth limit and 262 fs ≈ 370 fs$/\sqrt{2}$ for the average pulse duration. As the input parameters are taken from the measurement results, the perfect agreement is expected.

A second simulation considers the measured laser spectrum (displayed in the inset of Fig. 5.15(b)) and is presented in Fig. 5.18. Again, an average pulse duration of about 265 fs is obtained in agreement with the input parameter. However, the FWHM of the autocorrelation in Fig. 5.15(b) corresponds to a bandwidth limit of about 23 fs ≈ 32 fs$/\sqrt{2}$ and the width of the narrow feature in (c) reveals a pulse duration of about 21 fs ≈ 30 fs$/\sqrt{2}$.
The simulation provides pulse durations that are a little bit shorter than the measured ones. A reason for the longer pulse durations obtained from the measurements might again be a residual spatial chirp. Such a chirp cannot be compensated by the pulse shaper and the transform limit is not achieved. The issue of phase matching in the SHG process could be

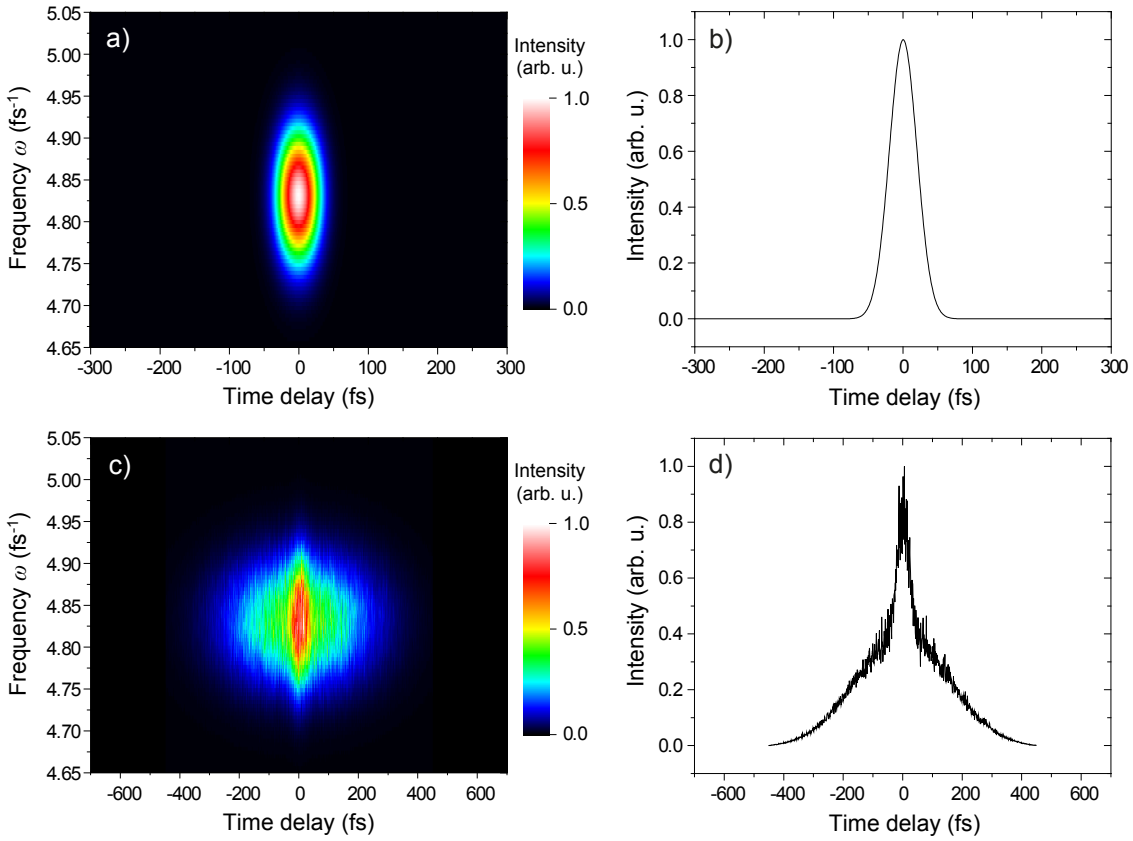

Figure 5.17: Simulation of the SHG scan. The SHG spectra as function of the time delay are calculated with the parameters determined in the measurements, i.e. a Gaussian spectrum with a center frequency of 2.415 fs^{-1} leading to bandwidth limited pulses of about 33 fs is assumed as well as an average pulse duration of 262 fs. The simulation exactly reproduces the measurements for transform-limited pulses, (a) and (b), and statistically varying pulses, (c) and (d). An average over 100 time-delay scans is taken for the case of noisy pulses. The determined FWHM are ∼47 fs (bandwidth-limited pulses) and ∼50 fs and ∼370 fs (noisy pulses), respectively.

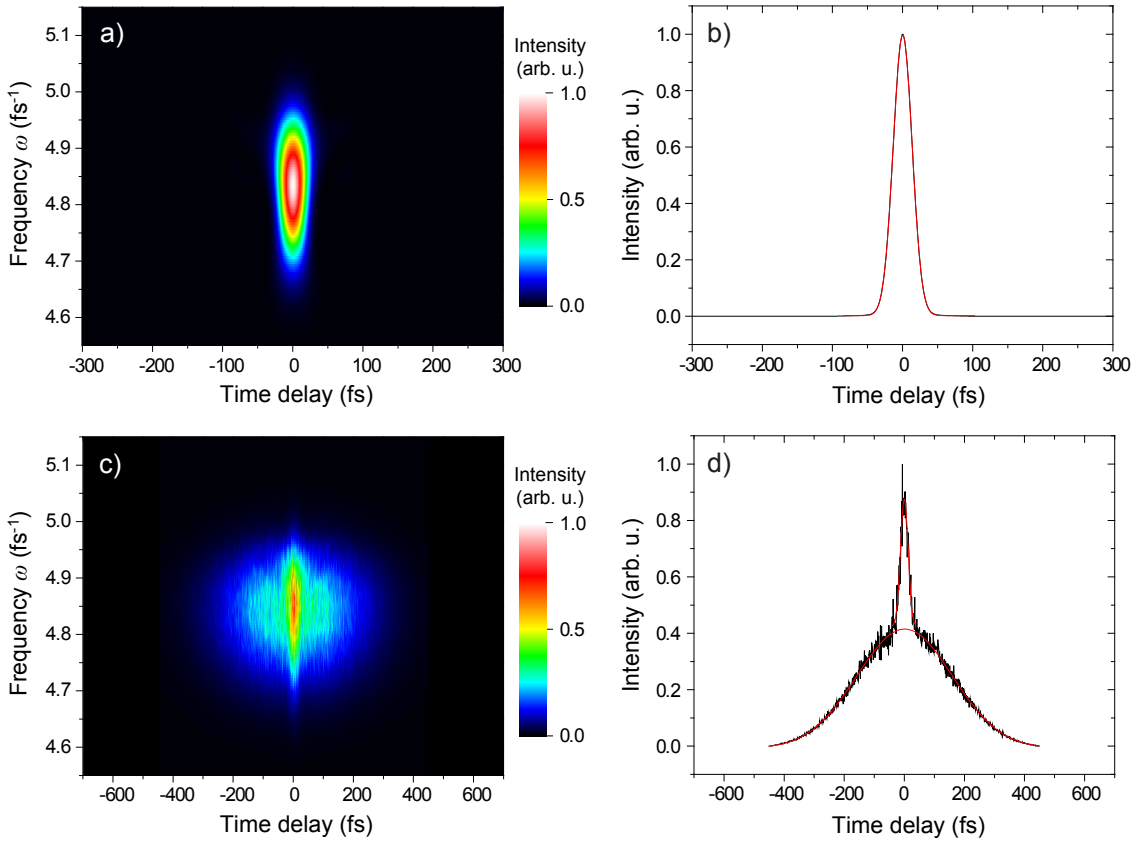

Figure 5.18: Simulation of the SHG scan with the measured laser spectrum as input parameter. (a) and (b) present the results for bandwidth-limited pulses and (c) and (d) for statistically varying pulses averaged over 100 time-delay scans. The distribution in (b) has a FWMH of ∼32 fs and reveals a bandwidth limit of about 23 fs. For the case of noisy pulses the widths are about 30 fs and 375 fs corresponding to a 21 fs transform-limited and 265 fs averaged pulse duration. The Gaussian fits are indicated in red.

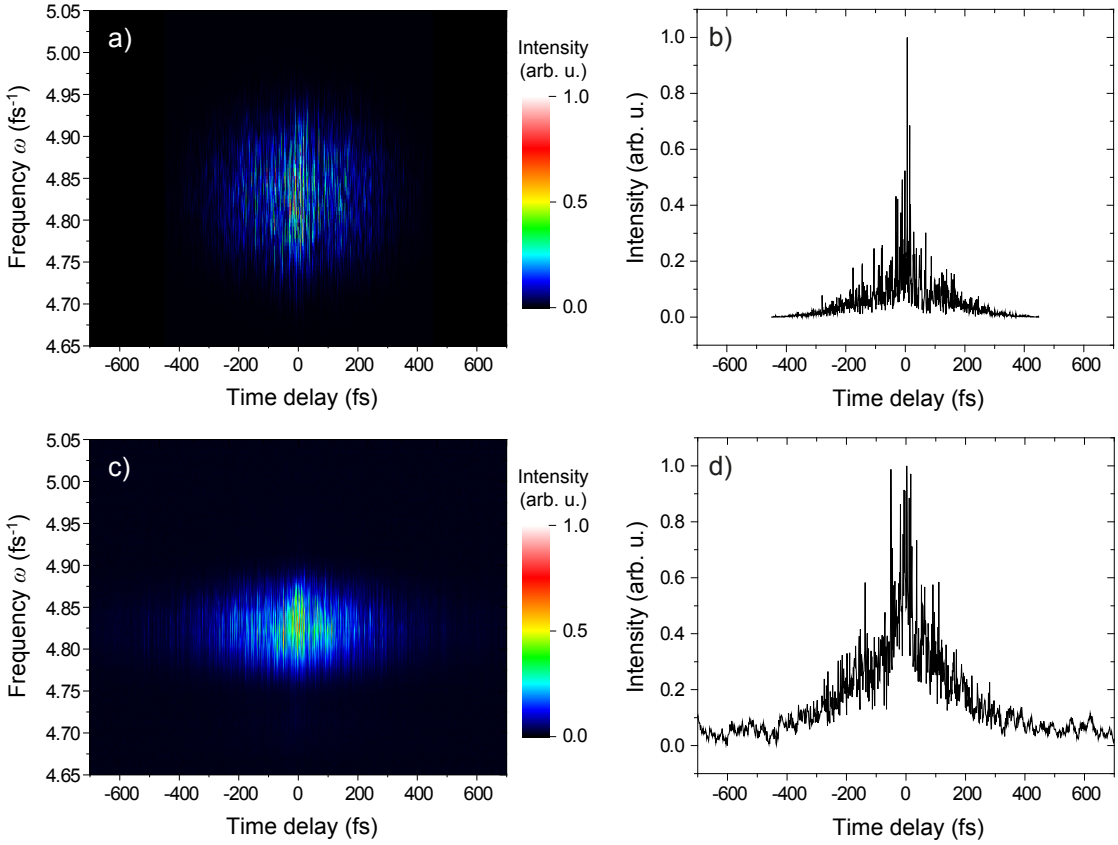

Figure 5.19: Single SHG scans for the case of statistically varying pulses in simulation, (a) and (b), and measurement, (c) and (d). The characteristic structure, i.e. a narrow spike sitting on top of a broad pedestal, is rudimentary visible. A lot of side peaks exist. Moreover, the result varies from scan to scan. Only an average over a significant number of such scans reveals the typical structure as it appears in Figs. 5.16 – 5.18.

another possible reason. In the simulation, all spectral components contribute to the SHG. The calculated SHG spectra cover a larger spectral range than the measured spectra.

If there is a phase mismatch, the different spectral contributions will not add up constructively and the second-harmonic conversion efficiency in the BBO will be reduced in the measurement.

As it is already discussed in section 5.1.4, it has to be pointed out again that sufficient statistics is necessary in case of partially coherent pulses. A single scan does not uncover the desired information. Figure 5.19 displays the SHG spectra of a single scan for both, simulation ((a) and (b)) and experiment ((c) and (d)). In both cases, the typical features cannot be revealed, but are covered by a lot of spikes. Moreover, the shapes of the spectra and integrated distributions vary from scan to scan. Therefore, an average over a number of scans needs to be taken to provide reliable information about the laser pulses.
The simulation of the SHG spectra using partially coherent pulses and the SHG measurements are also part of a Bachelor thesis carried out under my supervision [106]. Further details can be found therein.

The results confirm that the random-phase shaping implemented by our pulse-shaper

setup leads to the generation of partially coherent laser pulses in time. Thus, we are able to produce statistically varying pulse shapes which in turn allow us to study the effects in time-resolved experiment as demonstrated in the following section.

5.3 Measurements in the liquid phase

In section 5.1 the benefits of statistically fluctuating laser pulses are introduced for the example of an FEL pump–probe experiment studying the dynamics of D_2 molecules. It is demonstrated that the application of these laser pulses leads to an enhanced temporal resolution and dynamics on time scales shorter than the average pulse duration can be revealed. Now, the questions are (a), if the described new method can be transferred to other spectroscopy methods, (b) whether the dynamics of more complex systems can be investigated as well and (c), whether the concept can be generalized to other states of matter, i.e. not only gaseous, but also liquid phases for instance.
With the possibility at hand to produce partially coherent (noisy) laser pulses in our laboratory (as described in the previous section 5.2), the idea is to test the application of such laser pulses in transient-absorption measurements in the liquid phase. As model system we choose the dye IR144 again which is a complex molecule (cf. Fig. 4.5). It needs to be stressed that we are not interested in studying and understanding the dynamics of the dye in detail. The aim is to check whether the physics of the partial-coherence approach can be generalized to other pump–probe scenarios.

5.3.1 Transient-absorption measurements and their results

In order to answer the raised questions, transient-absorption measurements are carried out in a 0.25 mmol/l solution of the dye IR144 in methanol. The statistically fluctuating laser pulses are generated in the same way as explained in the previous section 5.2. An autocorrelation measurement (i.e. detecting the second-harmonic light as a function of the pump–probe time delay) yields a FWHM of $\sim$45 fs which corresponds to a transform-limited pulse duration of about 32 fs (FWHM). However, due to the partially coherent phases an average pulse duration of roughly 300 fs (cf. section 5.2) can be assumed for the noisy pulses. The pump and probe beam are focused to a size of about 150 µm in diameter (FWHM). The time delay between pump and probe pulse is scanned in steps of $\sim$2 fs over a range of about 1.8 ps, covering negative, i.e. the probe precedes the pump pulse, and positive time delays, i.e. the probe follows the pump pulse. For each time delay τ the spectrum of the transmitted probe beam, S_p, is measured and the reference laser spectrum, S_L, is detected as well (cf. chapter 3.3.1). In the analysis, the optical density is then calculated via equation (2.48) by $OD = -\log(S_p/S_L)$. It has to be noted that this definition of the optical density deviates from the one usually used in spectroscopy. There, the signal of the transmitted probe beam without the pump beam serves as reference spectrum. The reference spectrum in our case corresponds to the probe spectrum without pump multiplied by a factor c. Hence, the OD calculated in our case includes a constant offset which, however, does not influence the temporal dynamics at all.

The transient-absorption measurements are carried out for different pump-pulse energies. The energy of the probe pulse is always kept constant at about 27.5 µJ. For each pump energy, the scan is repeated five times and the average is taken. The transient-absorption measurements for the different pump-pulse energies are presented in Fig. 5.20. Figure 5.20(h) shows a time-delay scan for coherent, bandwidth-limited pump and probe pulses and a pump-pulse energy of 750 µJ as comparison. All scans have a minimum around zero time delay in common. The optical density is larger for negative than for positive time delays. This can be understood as for positive τ the pump beam has already excited the IR144 molecules and reduced the population of the ground state so that the probe light is absorbed less.

In order to unravel the temporal dynamics contained in the measurements, the signal is integrated over the spectral range $\omega \approx 2.249$ fs^{-1} - 2.587 fs^{-1}. These integrated signals are displayed in Fig. 5.21. The plots show all a common behaviour which is most distinct in Fig. 5.21(h), the case of 30 fs transform-limited pulses: The signal starts at a constant level. At a time delay of about 0 fs the signal begins to decrease exponentially. At zero time delay a dip appears on top of the exponential. The change between constant signal at negative time delays and exponential decay is very distinct. In case of statistically varying pulses shapes (Fig. 5.21(a) - (g)), this transition is washed-out due to the much longer pulse duration.
The signals are emulated by a fit function to get an estimate of the occurring dynamics and its time scales. The described characteristic behaviour is mimicked by an exponential decrease combined with a Heaviside function:

$$f(t) = a + b\,\Theta(t)\,\left[\left(a + b\,\mathrm{e}^{-\frac{t}{t_d}}\right) - (a+b)\right], \tag{5.10}$$

where t_d is the time constant of the exponential decay. In order to account for the temporal resolution given by the pulse duration, the model function $f(t)$ has to be convoluted with a Gaussian envelope of characteristic width σ

$$g(t) = d \cdot \mathrm{e}^{-\frac{t^2}{\sigma^2}}. \tag{5.11}$$

Then, the obtained fit function, $F(t) = f(t) * g(t)$, can be expressed as

$$F(t) = A + B\left[1 - \mathrm{erf}\left(\frac{t-t_0}{\sigma}\right) + \mathrm{e}^{\frac{\sigma^2}{4t_d^2}}\,\mathrm{e}^{-\frac{t-t_0}{t_d}} - \mathrm{e}^{\frac{\sigma^2}{4t_d^2}}\,\mathrm{e}^{-\frac{t-t_0}{t_d}}\,\mathrm{erf}\left(-\frac{t-t_0}{\sigma} + \frac{\sigma}{2t_d}\right)\right] \tag{5.12}$$

with a constant offset A, an overall amplitude B and a shift in time t_0. The addition of a Gaussian includes the fit of the dip. As the convolution of a Gaussian function with another Gaussian function yields a Gaussian again, the final fit function can be written as

$$F_{\mathrm{final}}(t) = F(t) + D\,\mathrm{e}^{-\frac{(t-t_C)^2}{2s^2}}. \tag{5.13}$$

The fit curves are indicated in red in Fig. 5.21 and the fit parameters of the exponential decay are summarized in Tab. 5.1 and of the dip in Tab. 5.2.

Comparing the integrated *OD* traces depicted in Fig. 5.21, it is clearly visible that their shapes are all similar as already mentioned above. All graphs exhibit a dip, i.e. a fast

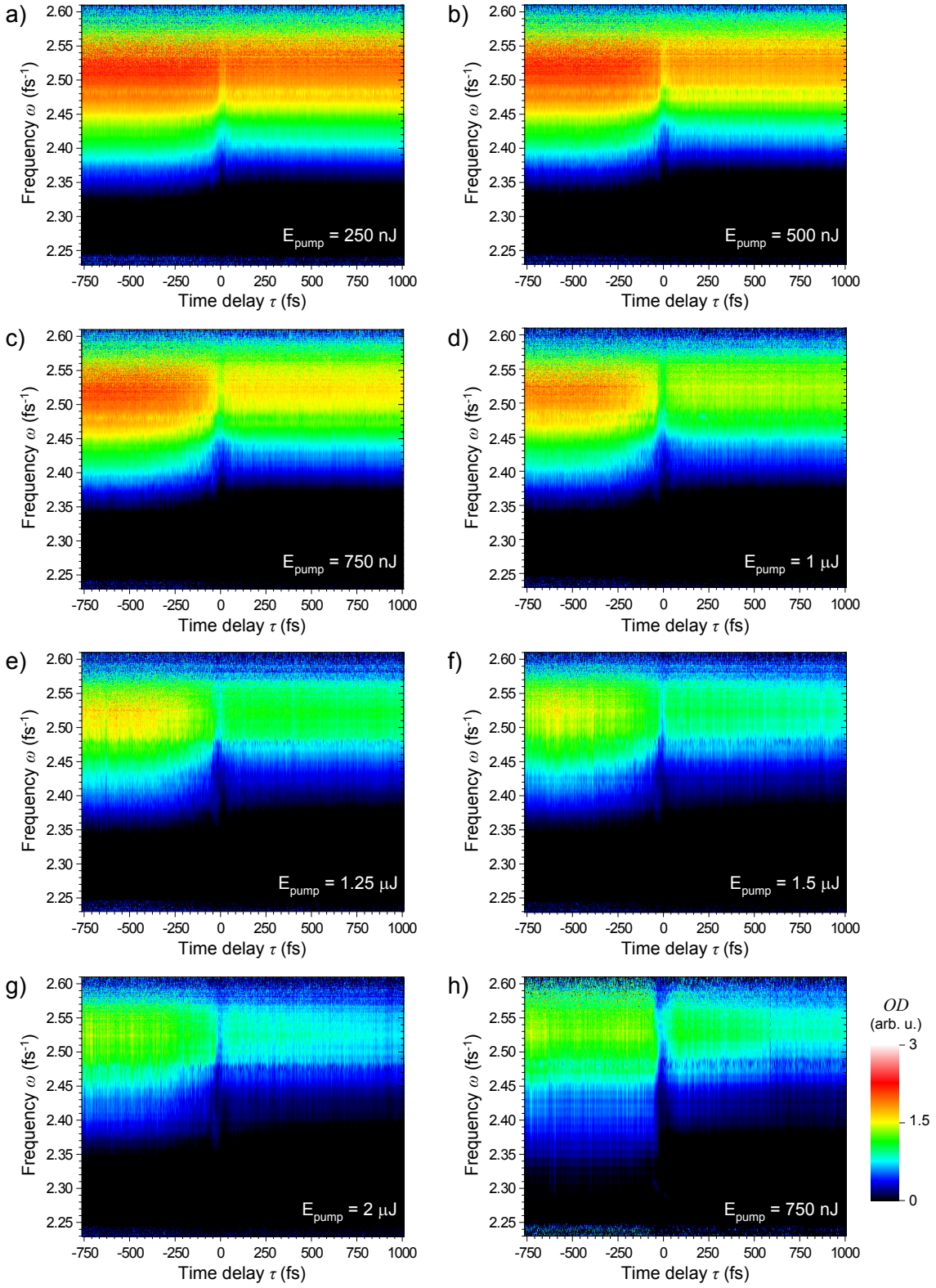

Figure 5.20: Transient-absorption measurements with statistically fluctuating laser pulses in a solution of IR144 in methanol. 2D representation of the measured probe spectrum as a function of the pump–probe time delay τ for different pump-pulse energies: (a) 250 nJ, (b) 500 nJ, (c) 750 nJ, (d) 1.0 μJ, (e) 1.25 μJ, (f) 1.5 μJ and (g) 2.0 μJ. (h) shows the measurement result for the case of coherent, transform-limited pulses and a pump-pulse energy of 750 nJ, for comparison with the other statistical-pulse datasets.

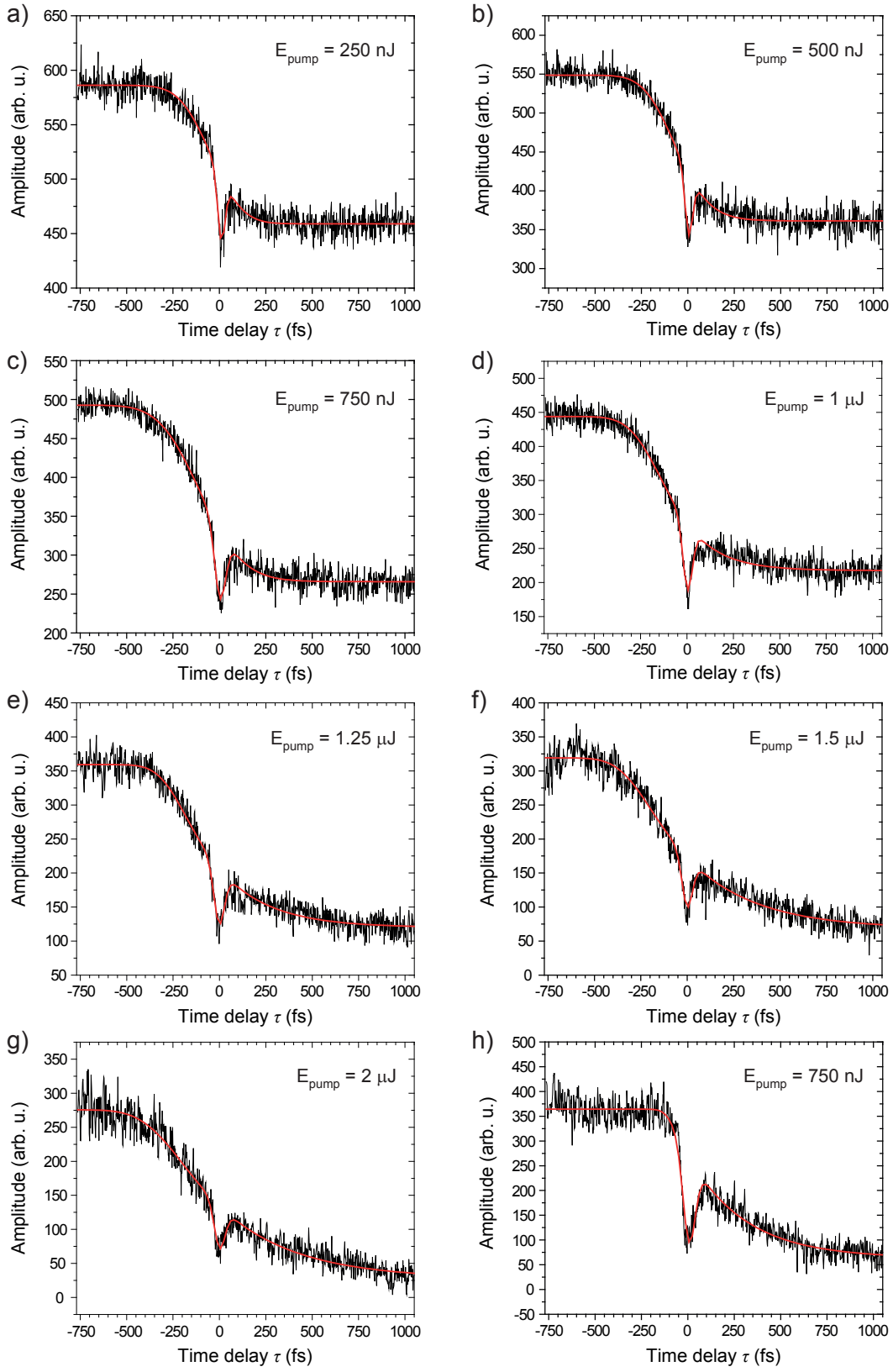

Figure 5.21: Integrated signals of the transient-absorption scans versus time delay for different pump-pulse energies: (a) 250 nJ, (b) 500 nJ, (c) 750 nJ, (d) 1.0 µJ, (e) 1.25 µJ, (f) 1.5 µJ, (g) 2.0 µJ and (h) 750 nJ, but bandwidth-limited pump and probe pulses. The fit curves derived from equation (5.13) are indicated in red.

Pump energy	A (arb. u.)	B (arb. u.)	t_0 (fs)	t_d (fs)	σ (fs)
250 nJ	459.0 ± 0.5	63.6 ± 0.4	-73.3 ± 26.4	27.5 ± 26.8	185.5 ± 9.9
500 nJ	361.3 ± 0.7	93.7 ± 0.5	-139.3 ± 15.0	84.6 ± 16.9	170.5 ± 13.7
750 nJ	266.0 ± 0.7	113.4 ± 0.6	-182.5 ± 18.6	88.8 ± 20.8	228.1 ± 14.5
1.0 µJ	217.6 ± 0.9	113.1 ± 0.7	-242.9 ± 7.2	176.6 ± 10.3	162.3 ± 11.6
1.25 µJ	120.0 ± 1.3	119.6 ± 0.8	-290.1 ± 6.0	267.6 ± 10.7	134.8 ± 12.8
1.5 µJ	68.4 ± 2.0	125.4 ± 1.2	-333.0 ± 7.7	360.8 ± 16.1	156.6 ± 17.2
2.0 µJ	27.6 ± 2.6	124.0 ± 1.5	-363.5 ± 10.1	403.7 ± 22.3	195.8 ± 22.1
TL, 750 nJ	63.4 ± 3.1	150.4 ± 1.6	-112.1 ± 12.9	303.2 ± 18.6	56.3 ± 26.0

Table 5.1: Fit parameters of the exponential decay. The values of the fit parameters describing the exponential decay (cf. equation (5.12)) are summarized as function of the pump-pulse energy. As fit error, the standard deviation is given. The result for transform-limited (TL) pulses at a pump-pulse energy of 750 nJ is listed as well.

Pump energy	D (arb. u.)	t_c (fs)	s (fs)	FWHM (fs)
250 nJ	-58.9 ± 2.9	9.9 ± 1.1	19.7 ± 1.2	46.4 ± 2.8
500 nJ	-78.4 ± 3.9	4.7 ± 1.1	20.2 ± 1.3	47.7 ± 3.0
750 nJ	-86.8 ± 3.2	3.0 ± 1.1	29.1 ± 1.3	68.6 ± 3.2
1.0 µJ	-96.9 ± 3.6	2.8 ± 1.0	25.1 ± 1.2	59.1 ± 2.7
1.25 µJ	-81.5 ± 3.5	-2.2 ± 1.4	28.2 ± 1.5	66.3 ± 3.5
1.5 µJ	-72.8 ± 3.9	-0.5 ± 1.7	27.8 ± 1.8	65.4 ± 4.3
2.0 µJ	-61.8 ± 4.0	1.0 ± 2.1	28.8 ± 2.3	67.9 ± 5.4
TL, 750 nJ	-173.6 ± 7.3	5.9 ± 1.2	32.4 ± 1.7	76.3 ± 4.0

Table 5.2: Fit parameters for mimicking the dip. The fit parameters characterizing the Gaussian envelope defined in equation (5.13) are summarized as a function of the pump-pulse energy. The standard deviation is given as fit error. The result for transform-limited (TL) pulses at a pump-pulse energy of 750 nJ is listed as well.

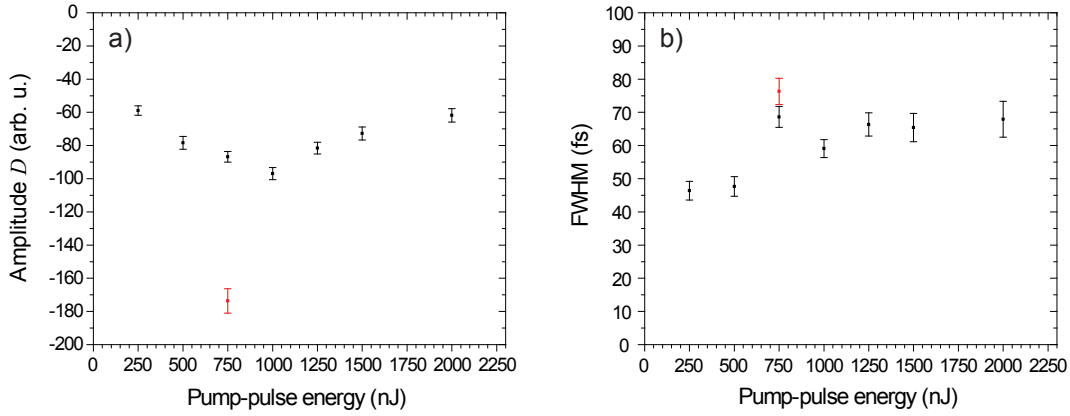

Figure 5.22: Fit parameters characterizing the dip at zero time delay. (a) Amplitude D and (b) full width at half maximum for the different pump-pulse energies. The red point represents the result for the case (h) in Fig. 5.21, i.e. for bandwidth-limited pulses.

decrease followed by an increase of the OD. As it is displayed in Fig. 5.22, the amplitude of the dip is roughly constant with increasing pump-pulse energy in the case of noisy pulses. For the transform-limited pulses, the absolute value of the amplitude is at least twice as large. Comparing the determined values of the FWHM in Tab. 5.2, it has to be noted that the FWHM becomes smaller for lower pump-pulse energies. It can be clearly recognized that the determined FWHM contains two contributions: (i) the bandwidth-limited pulse duration of about 32 fs (corresponding to a FWHM of approximately 45 fs of the autocorrelation) and (ii) the time scale of the induced dynamics. However, the latter contribution seems to play a minor role for lower pump-pulse energies. As the FWHM does not stay constant, we can rule out that only an autocorrelation is measured, but true molecule-specific dynamics is observed.
In the case of the bandwidth-limited pump and probe pulses, the transition around zero time delay from a constant to an exponentially decaying signal is most defined. In the case of partially coherent pulses, this transition is smoothed since the average pulse duration is much longer. This behavior can also be observed in Fig. 5.20. It is striking that the exponential decay becomes slower for increasing pump-pulse energy. Figure 5.23 shows the decay time constant t_d as a function of the pump-pulse energy. Typically, one would expect that the absorption signal returns to its initial level after some time and the rise of the signal becomes faster for increasing pump-pulse energy. The reason is that multiple excitations might occur for higher pulse intensities, leading to shorter lifetimes of the excited states due to effects like singlet-singlet annihilation [123, 124]. However, in our case the scan range is not large enough to observe the expected repopulation of the ground state. Furthermore, a decreasing decay time t_d of the absorption signal is expected with increasing pump-pulse energy since the ground state is assumed to be depleted faster at higher intensities. In contrast, the measured absorption signal decreases slower with increasing pump-pulse energy. This finding is surprising and is not understood at this point. For transform-limited pulses the estimated decay time t_d is by a factor of about 3 – 4 larger compared to the case of statistically fluctuating pulses at the same pulse energy and seems to correspond to the situation of noisy pulses at higher pulse energies. This agrees with the fact that a constant pulse energy, but at a shorter pulse length yields a higher

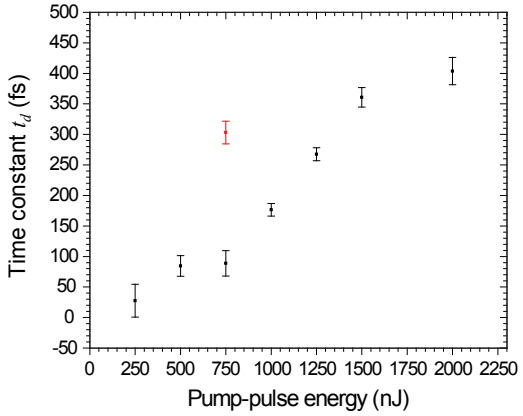

Figure 5.23: Fit parameter t_d describing the exponential decay as function of the different pump-pulse energies. The red point represents the case of transform-limited pulses (see Fig. 5.21(h)).

intensity. Thereby, an intensity which is comparable to the case of the bandwidth-limited pulses can only be achieved by increasing the pulse energy of the partially coherent pulses. From the measured *OD*s and the determined fit parameters, we can conclude that system-specific dynamics in the IR144 molecules is observed. Moreover, the dynamics changes in case of the partially coherent pulses since the time constant of the exponential decay and also the FWHM of the dip vary with increasing pump-pulse energy. Unfortunately, this dynamics is not yet understood and will be left for future work.

However, our aim is not to interpret and explain the measured time-delay traces in detail. For such a complex molecule like IR144, it is extremely difficult (if not impossible) to fully explain a transient-absorption measurement, especially without a detailed knowledge of the electronical and vibrational energy-level structure and possible transitions. For instance, fitting the dip at zero time delay with a Gaussian function is a strong simplification. A more suitable fit function would account for the fast decrease and increase of the *OD* trace which would consist of three exponential functions (without further discussing the possible combinations). The important message that has to be pointed out is: In our experiment, the dynamics is definitely revealed, although partially coherent pulses with about one order of magnitude larger average pulse duration are used. As in the case of the D_2 molecular dynamics (discussed in section 5.1), the partially coherent pulses enable the resolution of dynamics on time scales that are shorter than the average pulse duration. In analogy to the pump–probe experiment using FEL pulses, the time-resolved measurements performed in our laboratory demonstrate that the same benefit can be derived from the properties of statistically fluctuating pulses generated with a pulse shaper. We have shown that the concept of using noisy pulses is universal and can be applied to different spectroscopy techniques, e.g. transient-absorption measurements as chosen here. In the future, we can thus consider applications of partially coherent pulses in various spectroscopy implementations and gaseous or condensed states of matter. The choice of less complex molecules will then also allow us to understand and interpret the observed dynamics in more detail.

Chapter 6

Conclusion

In this work measuring and controlling phases in time-dependent quantum dynamics is the central theme, be it either fully coherent or statistically fluctuating phases. On the one hand fully coherent laser pulses are utilized in transient-absorption experiments to control the phase of the decaying dipole oscillation of the induced polarization. On the other hand statistically fluctuating (noisy) pulses, which are characterized by a partially coherent spectral phase, are considered intentionally in time-resolved spectroscopy with counterintuitive benefits as outcome.

Experimentally, the common basis of the studied phenomena are time-resolved pump–probe experiments, with special emphasis on transient-absorption measurements in the liquid phase. For this purpose, an extremely compact, stable and robust four-split mirror setup was built up providing full flexibility in the selection of the number of beams, their sizes and intensities. Up to four identical copies can be derived from the original incident laser beam so that an extension to two-dimensional spectroscopy is easily implemented. Moreover, the time delay between the sub-beams is introduced by the reflection off movable metal coated mirrors. This allows the adaptation of the setup to a wide range of wavelengths, not only in the visible or infrared regime. Provided that a grazing-incidence geometry is chosen for example, transient-absorption or even 2D-spectroscopy experiments with laser pulses in the ultraviolet or X-ray regime as delivered by Free-Electron Laser sources could be realized. For example, a 2D-spectroscopy measurement probing site-specifically core- and valence-electron transitions in aminophenols was theoreticaly proposed by Igor V. Schweigert and Shaul Mukamel [125].
The second main experimental tool in this thesis is the pulse shaper which also exhibits a high stability. We performed phase-only shaping to produce the partially coherent laser pulses. The pulse shaper was optimized for the modulation of the 30 fs laser pulses. However, it can be adapted to shorter pulses with a broader spectrum simply by replacing the pair of gratings by suitable ones.

In time-resolved experiments presented in chapter 4, we studied the absorption process in a small as well as a more complex system with coherent laser pulses. Initially, the laser-controlled modification of absorption lines was observed in transient-absorption measurements in gaseous helium [3, 4]. The excitation of the helium atoms by extreme ultraviolet (XUV) attosecond pulses leads to the population of singly excited and doubly excited,

autoionizing states. By changing the intensity of a time-delayed few-femtosecond visible/infrared laser pulse, the corresponding absorption profiles could be transformed from symmetric Lorentzian to asymmetric Fano line shapes and vice versa. We explained the observations made in the spectral domain by a time domain picture where the absorption lines are interpreted as exponentially decaying dipole responses, i.e. emitting dipoles, that interfere with the transmitted XUV light. The change of the absorption line shape could be understood as a phase shift of this dipole oscillation induced by the second, coupling laser pulse. A time-domain phase was introduced which could be mapped to the Fano parameter describing the asymmetry of the absorption profiles.
We then investigated whether the discovered phase control was a universal phenomenon that could be applied to more complex systems. Therefore, transient-absorption measurements in a complex dye molecule in the liquid phase were performed using few-femtosecond infrared laser pulses. Although such a large molecule exhibits a broad absorption band consisting of a large number of absorption lines with little spectral separation or even overlapping resonances, modifications in the absorption spectra with increasing intensity of the time-delayed coupling laser pulse were detected. A simulation based on the previous Fano-phase scheme was capable to describe the line-shape modifications by a coupling-laser induced phase shift of the dipole response as well, thus proving the generality of our formalism.

Chapter 5 was devoted to the question what the implications of partially coherent laser pulses are. In former pump–probe experiments studying the molecular wave-packet dynamics in deuterium using statistically fluctuating pulses provided by a Free-Electron Laser source [40], a temporal resolution on time scales shorter than the average pulse duration was observed contrary to all expectations. For the interpretation of the results, we developed a new concept [1] which attributes the enhanced temporal resolution to characteristic narrow features in the intensity autocorrelation functions of such statistically fluctuating laser pulses. The presence of these features whose width corresponds to the coherence time (determined by the spectral bandwidth of the pulses) ensures a resolution on these short time scales. We showed that our partial-coherence approach could be transferred to various kinds of pulse types like attosecond pulses where a time resolution in the few attosecond regime is within reach. We continued with the realization of statistically fluctuating laser pulses in our own laboratory by using the pulse shaper setup. These noisy pulses were then applied in transient-absorption measurements in the liquid phase demonstrating the same beneficial effect on the temporal resolution. We proved the universality of the concept of noisy pulses that a resolution on time scales shorter than the average pulse duration and close to the Fourier limit can be achieved. The properties of partially coherent pulses can be generalized to various time-dependent spectroscopy techniques and even different states of matter.

In case of ultrabroad spectra that cannot be compressed to their bandwidth limit, exploiting the properties of partially coherent laser pulses would offer to study dynamics of systems on extremely short time scales. For example, we could probably reach the sub-femtosecond regime by applying the pulse shaper to the few-femtosecond laser pulses obtained after the hollow-core fiber compression. This would also pave the way towards investigating the production of attosecond pulses with such noisy pulses. In general by shaping the laser pulses that generate the attosecond pulses, the properties of the high-

harmonic light could be optimized and tuned in a desired manner as already demonstrated by Philipp Raith for the case of a two-pixel pulse shaper [67].

All in all, the presented results open the door for numerous interesting and exciting experiments with applications in physics, but also chemistry, biology or even life sciences. For instance, the implementation of a segmented mirror in the attosecond-pulse beam path (in analogy to the setup presented in this thesis) would offer the potential for a large variety of experiments ranging from pump–probe to three-pulse or even 2D-spectroscopy measurements with attosecond resolution. Different laser pulse combinations, e.g. all-XUV or a combination of IR and XUV pulses, would be feasible. All-X-ray experiments applying Raman or two-dimensional spectroscopy were already proposed [125, 126] for example. In chemistry, charge migration in molecules, which is a topic attracting high interest for a few years [127–129], occurs on the order of attoseconds to a few femtoseconds. Time-resolved experiments using attosceond pulses and the spectroscopic techniques described here would allow access to this electron (or hole) motion. High temporal resolution is also essential to take snapshots of chemical reactions [130] or to investigate the process of charge transfer, e.g. as it was recently observed in a prototype system for organic photovoltaic cells [131], but on a much smaller and faster scale, on the level of individual atoms in molecules. In combination with shaped-pulse high-harmonic generation using the already existing control knobs, i.e. the spectral phase of the laser pulses and the phase of the system's dipole response, novel experimental schemes could be developed providing a deeper insight into, and control over, electron dynamics not only in atoms, but also molecules and condensed-phase/solid-state systems.

Appendix A

Experimental control of the SLM-S320

A.1 Calibration of the spatial light modulator

The calibration prior to each experiment is necessary to know which phase shift is induced when a specific voltage is applied and which spectral component is modulated by a given pixel. A voltage from 0 up to 4095 counts (corresponding to maximum 5 V in the low- and 8 V in the high-voltage mode) can be applied to each pixel. The calibration measurement is carried out as follows: Two crossed polarization filters are inserted, one before and one after the LCD. A spectrometer detects the laser light after the pulse shaper setup. The voltage is ramped up from 0 to 4095 counts for each pixel simultaneously. For each voltage step, a spectrum is detected. An exemplary scan is shown in Fig. A.1(c). The modulation of the intensity with increasing voltage is clearly visible. Then, a single pixel is blocked by setting the voltage to a value for which the intensity is minimized. At the same time, a voltage corresponding to maximum intensity is applied to all other pixels. A dip in the spectrum is created as displayed in Fig. A.1(a), fixing the position of the spectral range on the array of 320 pixels. The assignment of each pixel to a wavelength is done by creating a "comb" in the spectrum (cf. Fig. A.1(b)) where each tenth pixel (but containing the blocked pixel of Fig. A.1(a)) is blocked. Having the pixel-vs.-wavelength calibration at hand, the voltage scan (Fig. A.1(c)) can be converted into a map which attributes the induced relative phase shift to each pixel and a given voltage. The obtained phase map is depicted in Fig. A.1(d). A relative phase shift up to 4π is covered. In the measurement, the values of the phase pattern for every single pixel are looked up in the map and the corresponding voltage is applied to each pixel. If the phase exceeds the value of 4π, the phase is wrapped, i.e. the modulus of 4π is taken.

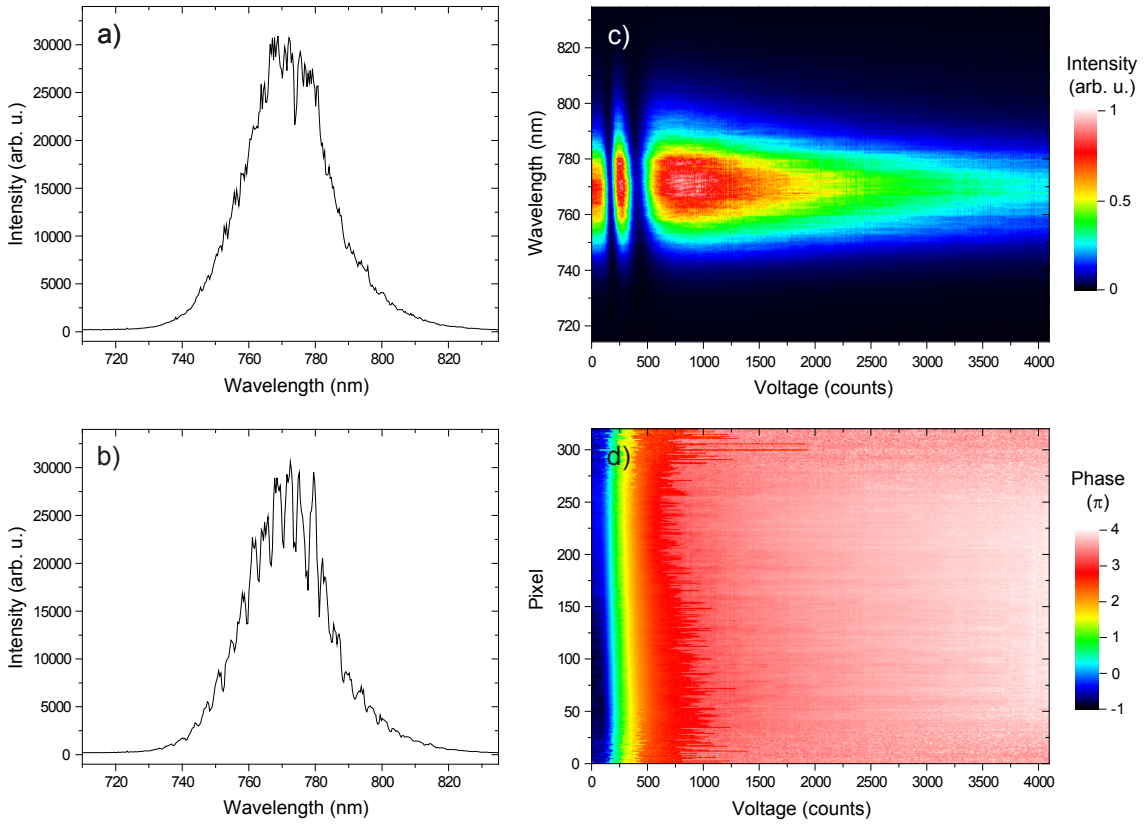

Figure A.1: Calibration of the liquid crystal spatial light modulator. (a) One pixel and (b) several pixels forming a comb are blocked. (c) The detected spectrum versus voltage showing the intensity modulation of each spectral component. (d) The finally obtained phase map depending on the pixel and the applied voltage.

A.2 SLM phase patterns - LabView program

As an example for all LabView programs developed for the control of the spatial light modulator (e.g. the programs needed for calibration or the pulse characterization method MIIPS), the main control program which enables to apply the desired phase pattern to the LCD is shown in Fig. A.2 (front panel) and Fig. A.3 (back panel).
The general structure of a SLM control program is as folllows: First of all, the computer has to connect to the SLM-320d and the spatial light modulator is initialized. Then, the desired control can be applied. If the program is stopped, the SLM is stopped and disconnected from the computer.
The entire control surface (front panel) is displayed in Fig. A.2. It can be split up into three main parts. The upper half contains all necessary information required for the operation of the SLM. These are the information obtained from the spectrometer (wavelength axis, laser spectrum) and from the calibration (the assignment of wavelength to pixel and phase to voltage). The lower left part, headed "SLM Control", shows any error that might occur in the course of the communication between computer and SLM. Furthermore, the temperature of the LCD can be interrogated. The voltage that will be applied to the LCD is shown and the chosen phase is activated on the display by pushing the button "Write pattern". The "STOP program" button finishes the program. The lower right part represents the simulation of the pulse shape and the expected intensity and interferometric autocorrelations for a chosen phase. Different functions can be selected as phase: a linear, sinusoidal or polynomial (up to third order) phase pattern can be chosen. Furthermore, a Heaviside function, a random phase varying between 0 and 2π or white noise can be applied. The simulation can be carried out before the phase pattern is written onto the SLM display. Thereby, it is possible to test the chosen phase pattern and to check the obtained pulse shape. If the desired phase is adjusted, the corresponding voltages are obtained from the calibration and the pattern can be activated on the LCD.
It has to be noted that the phase is defined as a function of the frequency. Therefore, all information given as a function of the wavelength is converted into frequency-dependent information in the beginning. In the simulation section, the frequency is used as well instead of the wavelength. Fig. A.3 shows the programmed control section on which the control surface is based.

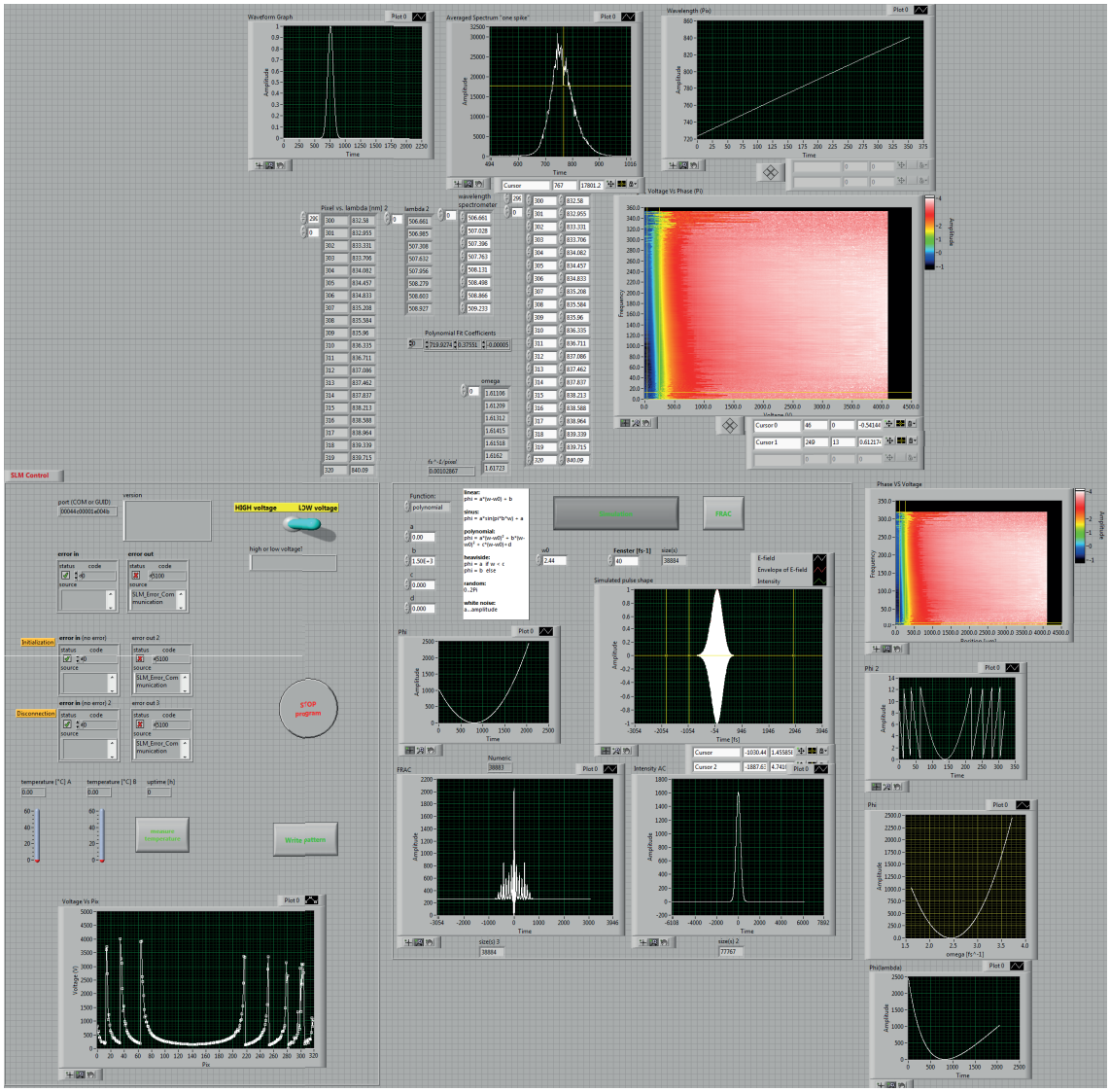

Figure A.2: Pattern control of the SLM, front panel. The control surface of the LabView program is structured into three parts. The upper half includes all information necessary for the operation of the spatial light modulator, i.e. the calibration (pixel-vs.-wavelength and phase-to-voltage assignment) and the spectrometer information (wavelength, spectrum). The lower half contains the main control, i.e. checking for errors, writing pattern on the LCD, stopping program etc., on the left side and the simulation section, i.e. selecting the phase pattern and calculating the expected pulse shape and autocorrelations, on the right side.

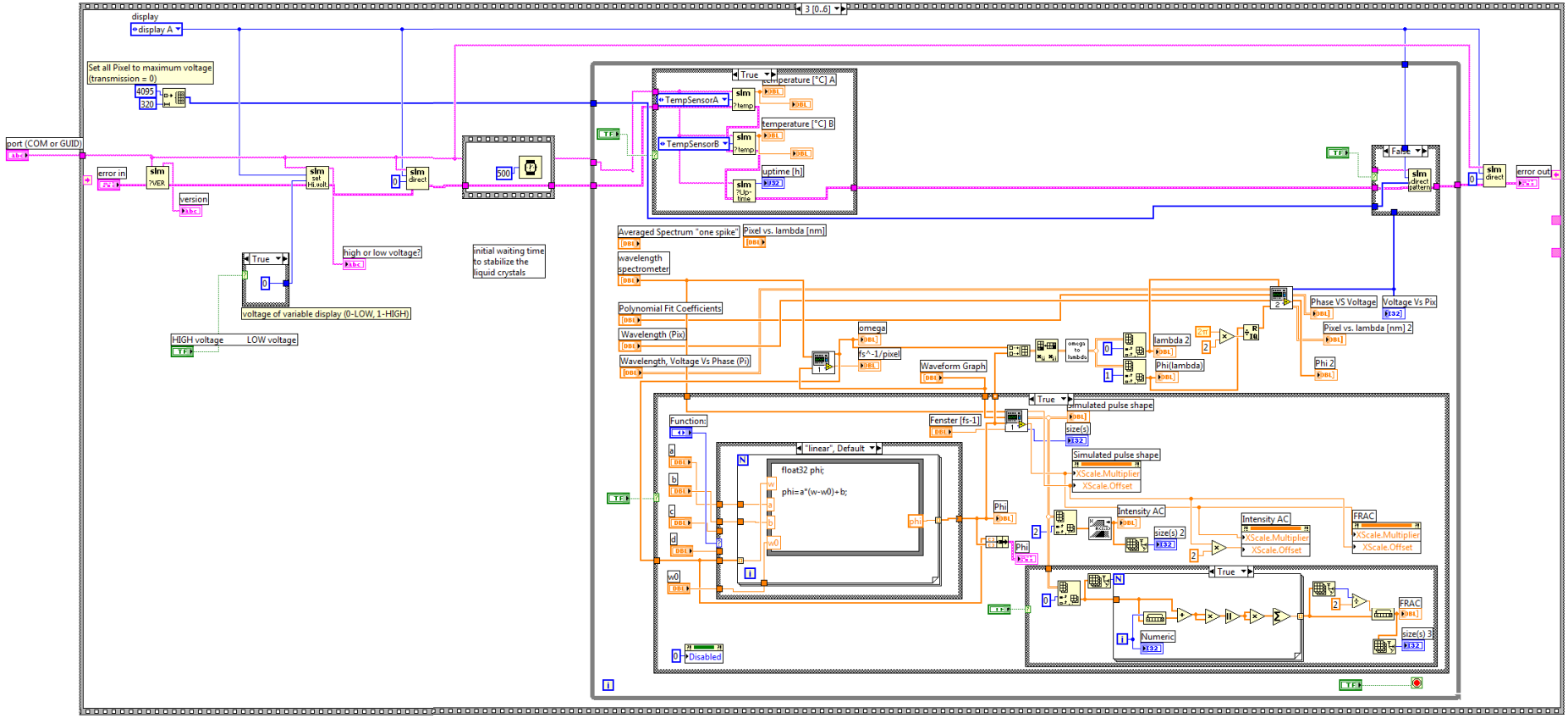

Figure A.3: Pattern control of the SLM, back panel. The phase control section as the main part of the LabView program is presented. Before and after this section, the connection to the computer, the initialization of the spatial light modulator and the disconnection from the computer, respectively, are carried out. A phase pattern can be chosen and the expected pulse shape and interferometric and intensity autocorrelations are calculated. If the desired phase is found, it is converted into the corresponding voltage by using the calibration information and the pattern can be applied to the SLM display.

Appendix B

Atomic units

In atomic and molecular physics it is very common to use atomic units (a.u.) instead of the International System of Units (SI) in the calculations. It is a system of natural units. The atomic units are based on the scales of the electron in the hydrogen atom. For example, in atomic units the length is described by the Bohr radius a_0, the mass by the electron mass m_e, the charge by the elementary charge e and the energy by the Hartree energy E_h. The other units can be derived from these quantities, e.g. the atomic unit of time is defined by $\hbar/E_h$ and of the electric field by $E_h/(ea_0)$. In atomic units the reduced Planck constant $\hbar$, the elementary charge e, the electron mass m_e and the Coulomb constant of the electric force $(4\pi\varepsilon_0)^{-1}$ are set to one: $\hbar = e = m_e = 1/(4\pi\varepsilon_0) = 1$. Thus, complex expressions like the Schrödinger equation are simplified. For example, the Hamilton operator describing the electron in the hydrogen atom is given in SI units by

$$\hat{H} = -\frac{\hbar^2}{2m_e}\nabla^2 - \frac{1}{4\pi\varepsilon_0}\frac{e^2}{r}, \tag{B.1}$$

whereas in atomic units it reads as

$$\hat{H} = -\frac{1}{2}\nabla^2 - \frac{1}{r}. \tag{B.2}$$

Atomic unit of	SI value
Length	$(0.529\,177\,210\,92 \pm 0.000\,000\,000\,17)$ Å
Energy	$(27.211\,385\,05 \pm 0.000\,000\,60)$ eV
Time	$(24.188\,843\,265\,02 \pm 0.000\,000\,000\,12) \cdot 10^{-18}$ s
Electric field strength	$(5.142\,206\,52 \pm 0.000\,000\,11) \cdot 10^{9}$ V/cm
Intensity	$(3.509\,445\,21 \pm 0.000\,000\,15) \cdot 10^{16}$ W/cm^2

Table B.1: Selected physical quantities in atomic units and their conversion into SI units. The data are taken from [132] that was updated in 2010.

Bibliography

[1] K. Meyer, C. Ott, P. Raith, A. Kaldun, Y. Jiang, A. Senftleben, M. Kurka, R. Moshammer, J. Ullrich, and T. Pfeifer.
Noisy Optical Pulses Enhance the Temporal Resolution of Pump-Probe Spectroscopy.
Phys. Rev. Lett. **108**, 098302 (2012).

[2] Y. Zhang, K. Meyer, C. Ott, and T. Pfeifer.
Passively phase-stable, monolithic, all-reflective two-dimensional electronic spectroscopy based on a four-quadrant mirror.
Opt. Lett. **38**, 356–358 (2013).

[3] C. Ott, A. Kaldun, P. Raith, K. Meyer, M. Laux, J. Evers, C. H. Keitel, C. H. Greene, and T. Pfeifer.
Lorentz Meets Fano in Spectral Line Shapes: A Universal Phase and Its Laser Control.
Science **340**, 716–720 (2013).

[4] C. Ott, A. Kaldun, P. Raith, K. Meyer, M. Laux, Y. Zhang, S. Hagstotz, T. Ding, R. Heck, and T. Pfeifer.
Quantum Interferometry and Correlated Two-Electron Wave-Packet Observation in Helium.
arXiv:1205.0519v1 [physics.atom-ph] (2012).

[5] K. Schnorr, A. Senftleben, G. Schmid, A. Rudenko, M. Kurka, K. Meyer, L. Foucar, M. Kübel, M. F. Kling, Y. H. Jiang, S. Düsterer, R. Treusch, C. D. Schröter, J. Ullrich, T. Pfeifer, and R. Moshammer.
Multiple ionization and fragmentation dynamics of molecular Iodine studied in IR-XUV pump-probe experiments.
submitted to Farad. Discuss. (2014).

[6] K. Schnorr, A. Senftleben, M. Kurka, A. Rudenko, G. Schmid, T. Pfeifer, K. Meyer, M. Kübel, M. F. Kling, Y. H. Jiang, R. Treusch, S. Düsterer, B. Siemer, M. Wöstmann, H. Zacharias, R. Mitzner, T. J. M. Zouros, J. Ullrich, C. D. Schröter, and R. Moshammer.
Electron Rearrangement Dynamics in Dissociating I_2^{n+} Molecules Accessed by Extreme Ultraviolet Pump-Probe Experiments.
Phys. Rev. Lett. **113**, 073001 (2014).

[7] A. Kaldun, C. Ott, A. Blättermann, M. Laux, K. Meyer, T. Ding, A. Fischer, and T. Pfeifer.
Extracting Phase and Amplitude Modifications of Laser-Coupled Fano Resonances.
Phys. Rev. Lett. **112**, 103001 (2014).

[8] Y. Mi, A. Kaldun, K. Meyer, and T. Pfeifer.
Time-domain pulse compression by interfering time-delay operations.
Phys. Rev. A **88**, 053824 (2013).

[9] P. Raith, C. Ott, K. Meyer, A. Kaldun, M. Laux, M. Ceci, C. P. Anderson, and T. Pfeifer.
Carrier-envelope phase- and spectral control of fractional high-harmonic combs.
J. Appl. Phys. **114**, 173102 (2013).

[10] K. Schnorr, A. Senftleben, M. Kurka, A. Rudenko, L. Foucar, G. Schmid, A. Broska, T. Pfeifer, K. Meyer, D. Anielski, R. Boll, D. Rolles, M. Kübel, M. F. Kling, Y. H. Jiang, S. Mondal, T. Tachibana, K. Ueda, T. Marchenko, M. Simon, G. Brenner, R. Treusch, S. Scheit, V. Averbukh, J. Ullrich, C. D. Schröter, and R. Moshammer.

Time-Resolved Measurement of Interatomic Coulombic Decay in Ne_2.
Phys. Rev. Lett. **111**, 093402 (2013).

[11] C. Ott, M. Schönwald, P. Raith, A. Kaldun, G. Sansone, M. Krüger, P. Hommelhoff, Y. Patil, Y. Zhang, K. Meyer, M. Laux, and T. Pfeifer.
Strong-field spectral interferometry using the carrier-envelope phase.
New J. Phys. **15**, 073031 (2013).

[12] P. Raith, C. Ott, C. P. Anderson, A. Kaldun, K. Meyer, M. Laux, Y. Zhang, and T. Pfeifer.
Fractional high-order harmonic combs and energy tuning by attosecond-precision split-spectrum pulse control.
Appl. Phys. Lett. **100**, 121104 (2012).

[13] S. Chu, L. Hollberg, J. E. Bjorkholm, A. Cable, and A. Ashkin.
Three-Dimensional Viscous Confinement and Cooling of Atoms by Resonance Radiation Pressure.
Phys. Rev. Lett. **55**, 48–51 (1985).

[14] S. Chu, J. E. Bjorkholm, A. Ashkin, and A. Cable.
Experimental Observation of Optically Trapped Atoms.
Phys. Rev. Lett. **57**, 314–317 (1986).

[15] M. H. Anderson, J. R. Ensher, M. R. Matthews, C. E. Wieman, and E. A. Cornell.
Observation of Bose-Einstein Condensation in a Dilute Atomic Vapor.
Science **269**, 198–201 (1995).

[16] K. B. Davis, M.-O. Mewes, M. R. Andrews, N. J. van Druten, D. S. Durfee, D. M. Kurn, and W. Ketterle.
Bose-Einstein Condensation in a Gas of Sodium Atoms.
Phys. Rev. Lett. **75**, 3969–3973 (1995).

[17] T. Udem, R. Holzwarth, and T. W. Hänsch.
Optical frequency metrology.
Nature **416**, 233–237 (2002).

[18] M. Hentschel, R. Kienberger, C. Spielmann, G. A. Reider, N. Milosevic, T. Brabec, P. Corkum, U. Heinzmann, M. Drescher, and F. Krausz.
Attosecond metrology.
Nature **414**, 509–513 (2001).

[19] T. Brixner, J. Stenger, H. M. Vaswani, M. Cho, R. E. Blankenship, and G. R. Fleming.
Two-dimensional spectroscopy of electronic couplings in photosynthesis.
Nature **434**, 625–628 (2005).

[20] G. S. Engel, T. R. Calhoun, E. L. Read, T.-K. Ahn, T. Mancal, Y.-C. Cheng, R. E. Blankenship, and G. R. Fleming.
Evidence for wavelike energy transfer through quantum coherence in photosynthetic systems.
Nature **446**, 782–786 (2007).

[21] U. Fano.
Sullo spettro di assorbimento dei gas nobili presso il limite dello spettro d'arco.
Nuovo Cim. **12**, 154–161 (1935).

[22] U. Fano.
Effects of Configuration Interaction on Intensities and Phase Shifts.
Phys. Rev. **124**, 1866–1878 (1961).

[23] R. P. Madden and K. Codling.
New autoionizing atomic energy levels in He, Ne and Ar.
Phys. Rev. Lett. **10**, 516–518 (1963).

[24] U. Fano and J. W. Cooper.
Spectral Distribution of Atomic Oscillator Strengths.
Rev. Mod. Phys. **40**, 441–507 (1968).

[25] J. M. Rost, K. Schulz, M. Domke, and G. Kaindl.
Resonance parameters of photo doubly excited helium.
J. Phys. B: At. Mol. Opt. Phys. **30**, 4663–4694 (1997).

[26] M. Kroner, A. O. Govorov, S. Remi, B. Biedermann, S. Seidl, A. Badolato, P. M. Petroff, W. Zhang, R. Barbour, B. D. Gerardot, R. J. Warburton, and K. Karrai.
The nonlinear Fano effect.
Nature **451**, 311–314 (2008).

[27] J. A. Fan, C. Wu, K. Bao, J. Bao, R. Bardhan, N. J. Halas, V. N. Manoharan, P. Nordlander, G. Shvets, and F. Capasso.
Self-Assembled Plasmonic Nanoparticle Clusters.
Science **328**, 1135–1138 (2010).

[28] A. R. Schmidt, M. H. Hamidian, P. Wahl, F. Meier, A. V. Balatsky, J. D. Garrett, T. J. Williams, G. M. Luke, and J. C. Davis.
Imgaing the Fano lattice to 'hidden order' transition in URu_2Si_2.
Nature **465**, 570–576 (2010).

[29] A. E. Miroshnichenko, S. Flach, and Y. S. Kivshar.
Fano resonances in nanoscale structures.
Rev. Mod. Phys. **82**, 2257–2298 (2010).

[30] J. M. Blatt and V. F. Weisskopf.
Theoretical Nuclear Physics.
Wiley, New York (1952).

[31] S. H. Linn, W. B. Tzeng, J. M. Brom, Jr., and C. Y. Ng.
Molecular beam photoionization study of $HgBr_2$ and HgI_2.
J. Chem. Phys. **78**, 50–61 (1983).

[32] K. Wiesenfeld and F. Moss.
Stochastic resonance and the benefits of noise: from ice ages to cray fish and SQUIDs.
Nature **373**, 33–36 (1995).

[33] K. P. Singh and J. M. Rost.
Optimal Stochastic Enhancement of Photoionization.
Phys. Rev. Lett **98**, 160201 (2007).

[34] H. A. Pike and M. Hercher.
Basis for Picosecond Structure in Mode-Locked Laser Pulses.
J. Appl. Phys. **41**, 4562–4565 (1970).

[35] B. Dayan, A. Pe'er, A. A. Friesem, and Y. Silberberg.
Two Photon Absorption and Coherent Control with Broadband Down-Converted Light.
Phys. Rev. Lett. **93**, 023005 (2004).

[36] O. Kinrot, I. S. Averbukh, and Y. Prior.
Measuring Coherence while Observing Noise.
Phys. Rev. Lett. **75**, 3822–3825 (1995).

[37] M. J. Stimson, D. J. Ulness, and A. C. Albrecht.
Frequency and time resolved coherent Stokes Raman scattering in CS_2 using incoherent light.
Chem. Phys. Lett. **263**, 185–190 (1996).

[38] M. J. Stimson, D. J. Ulness, and A. C. Albrecht.
Time-Resolved Coherent Raman Spectroscopy Controlled by Spectrally Tailored Noisy Light.
J. Raman Spectrosc. **28**, 579–587 (1997).

[39] X. G. Xu, S. O. Konorov, J. W. Hepburn, and V. Milner.
Noise autocorrelation spectroscopy with coherent Raman scattering.
Nature Phys. **4**, 125–129 (2008).

[40] Y. H. Jiang, A. Rudenko, J. F. Perez-Torres, O. Herrwerth, L. Foucar, M. Kurka, K. U. Kühnel, M. Toppin, E. Plesiat, F. Morales, F. Martinn, M. Lezius, M. F. Kling, T. Jahnke, R. Dörner, J. L. Sanz-Vicario, J. van Tilborg, A. Belkacem, M. Schulz, K. Ueda, T. J. M. Zouros, S. Düsterer, R. Treusch, C. D. Schröter, R. Moshammer, and J. Ullrich.
Investigating two-photon double ionization of D_2 by XUV-pump–XUV-probe experiments.
Phys. Rev. A **81**, 051402(R) (2010).

[41] R. Thomson, C. Leburn, and D. Reid (Eds.).
Ultrafast Nonlinear Optics.
Springer (2013).

[42] J.-C. Diels and W. Rudolph.
Ultrashort Laser Pulse Phenomena.
Second Edition. Academic Press (2006).

[43] W. Demtröder.
Laserspektroskopie.
5. Auflage. Springer, Berlin Heidelberg (2007).

[44] C. Rullière (Ed.).
Femtosecond Laser Pulses.
Second Edition. Springer (2005).

[45] R. W. Boyd.
Nonlinear Optics.
Second Edition. Academic Press (2003).

[46] B. E. A. Saleh and M. C. Teich.
Fundamentals of Photonics.
Second Edition. Wiley (2007).

[47] A. Monmayrant, S. Weber, and B. Chatel.
A newcomer's guide to ultrashort pulse shaping and characterization.
J. Phys. B: At. Mol. Opt. Phys. **43**, 103001 (2010).

[48] D. J. Kane and R. Trebino.
Single-shot measurement of the intensity and phase of an arbitrary ultrashort pulse by using frequency-resolved optical gating.
Opt. Lett. **18**, 823–825 (1993).

[49] C. Iaconis and I. A. Walmsley.
Spectral phase interferometry for direct electric-field reconstruction of ultrashort optical pulses.
Opt. Lett. **23**, 792–794 (1998).

[50] C. Cohen-Tannoudji, B. Diu, and F. Laloë.
Quantum Mechanics, volume I.
Wiley-Interscience (1977).

[51] J. J. Sakurai and J. Napolitano.
Modern Quantum Mechanics.
Second edition. Addison-Wesley (2011).

[52] A. H. Zewail.
Femtochemistry.
J. Phys. Chem. **97**, 12427–12446 (1993).

[53] B. M. Garraway and K.-A. Suominen.
Wave-packet dynamics: new physics and chemistry in femto-time.
Rep. Prog. Phys. **58**, 365–419 (1995).

[54] A. H. Zewail.
Femtochemistry: Atomic-Scale Dynamics of the Chemical Bond.
J. Phys. Chem. A **104**, 5660–5694 (2000).

[55] A. Javan, W. R. Bennett, and D. R. Herriott.
Population Inversion and Continuous Optical Maser Oscillation in a Gas Discharge Containing a He-Ne Mixture.
Phys. Rev. Lett. **6**, 106–110 (1961).

[56] J. M. J. Madey.
Stimulated Emission of Bremsstrahlung in a Periodic Magnetic Field.
J. Appl. Phys. **42**, 1906 –1913 (1971).

[57] L. R. Elias, W. M. Fairbank, J. M. J. Madey, H. A. Schwettman, and T. I. Smith.
Observation of Stimulated Emission of Radiation by Relativistic Electrons in a Spatially Periodic Transverse Magnetic Field.
Phys. Rev. Lett. **36**, 717–720 (1976).

[58] D. A. G. Deacon, L. R. Elias, J. M. J. Madey, G. J. Ramian, H. A. Schwettman, and T. I. Smith.
First Operation of a Free-Electron Laser.
Phys. Rev. Lett. **38**, 892–894 (1977).

[59] http://www.femtolasers.com/compact-PRO-CEP.109.0.html (August 2014).

[60] http://www.femtolasers.com/RAINBOW-TM.114.0.html (August 2014).

[61] D. Strickland and G. Mourou.
Compression of Amplified Chirped Optical Pulses.
Opt. Commun. **56**, 219–221 (1985).

[62] M. Nisoli, S. De Silvestri, and O. Svelto.
Generation of high energy 10 fs pulses by a new pulse compression technique.
Appl. Phys. Lett. **68**, 2793–2795 (1996).

[63] T. Pfeifer.
Adaptive control of coherent soft-x-rays.
PhD Thesis, Universität Würzburg (2004).

[64] http://www.femtolasers.com/KALEIDOSCOPE-TM.122.0.html (August 2014).

[65] http://www.femtolasers.com/FEMTOMETER-TM.120.0.html (August 2014).

[66] C. Ott.
Attosecond multidimensional interferometry of single and two correlated electrons in atoms.
PhD Thesis, Universität Heidelberg (2012).

[67] P. Raith.
Few-Cycle Multidimensional Laser Control of Attosecond Pulse Generation.
PhD Thesis, Universität Heidelberg (2012).

[68] B. D. Patterson and R. Abela.
Novel opportunities for time-resolved absorption spectroscopy at the X-ray free electron laser.
Phys. Chem. Chem. Phys. **12**, 5647–5652 (2010).

[69] http://photon-science.desy.de/facilities/flash/the_free_electron_laser/index_eng.html (August 2014).

[70] E. L. Saldin, E. A. Schneidmiller, and M. V. Yurkov.
The Physics of Free Electron Lasers.
Springer, Berlin Heidelberg (2000).

[71] E. L. Saldin, E. A. Schneidmiller, and M. V. Yurkov.
Statistical and coherence properties of radiation from x-ray free-electron lasers.
New J. Phys. **12**, 035010 (2010).

[72] B. W. J. McNeil and N. R. Thompson.
X-ray free-electron lasers.
Nature Photon. **4**, 814–821 (2010).

[73] R. Dörner, V. Mergel, O. Jagutzki, L. Spielberger, J. Ullrich, R. Moshammer, and H. Schmidt-Böcking.
Cold target recoil ion momentum spectroscopy: a 'momentum microscope' to view atomic collision dynamics.
Phys. Rep. **330**, 95–192 (2000).

[74] J. Ullrich, R. Moshammer, A. Dorn, R. Dörner, L. P. H. Schmidt, and H. Schmidt-Böcking.
Recoil-ion and electron momentum spectroscopy: reaction-microscopes.
Rep. Progr. Phys. **66**, 1463–1545 (2003).

[75] A. T. J. B. Eppink and D. H. Parker.
Velocity map imaging of ions and electrons using electrostatic lenses: Application in photoelectron and photofragment ion imaging of molecular oxygen.
Rev. Sci. Instrum. **68**, 3477–3484 (1997).

[76] D. Fischer.
Mehr-Teilchen-Dynamik in der Einfach- und Doppelionisation von Helium durch geladene Projektile.
PhD Thesis, Universität Heidelberg (2003).

[77] N. Camus.
Non-sequential double ionization of atoms with phase-controlled ultra-short laser pulses.
PhD Thesis, Universität Heidelberg (2013).

[78] T. Kobayashi, J. Du, W. Feng, and K. Yoshino.
Excited-State Molecular Vibration Observed for a Probe Pulse Preceding the Pump Pulse by Real-Time Optical Spectrsocopy.
Phys. Rev. Lett. **101**, 037402 (2008).

[79] http://www.oceanoptics.com/product/usb2000-custom/ (August 2014).

[80] http://www.oceanoptics.com/product/usb4000-custom/ (August 2014).

[81] http://www.oceanoptics.com/product/premium-grade-patch-cords/ (August 2014).

[82] Jenoptik Optical Systems.
SLM-S640 SLM-S320 Technical Documentation (May 2010).

[83] A. Präkelt, M. Wollenhaupt, A. Assion, C. Horn, C. Sarpe-Tudoran, M. Winter, and T. Baumert.
Compact, robust, and flexible setup for femtosecond pulse shaping.
Rev. Sci. Instrum. **74**, 4950–4953 (2003).

[84] O. E. Martinez.
3000 Times Grating Compressor with Positive Group Velocity Dispersion: Application to Fiber Compensation in 1.3-1.6 μm Region.
IEEE J. Quant. Electron. **QE-23**, 59–64 (1987).

[85] A. M. Weiner.
Ultrafast optical pulse shaping: A tutorial overview.
Opt. Commun. **284**, 3669–3692 (2011).

[86] B. von Vacano and M. Motzkus.
Time-resolved two color single-beam CARS employing supercontinuum and femtosecond pulse shaping.
Opt. Commun. **264**, 488–493 (2006).

[87] D. Meshulach and Y. Silberberg.
Coherent quantum control of two-photon transitions by a femtosecond laser pulse.
Nature **396**, 239–242 (1998).

[88] K. A. Walowicz, I. Pastirk, V. V. Lozovoy, and M. Dantus.
Multiphoton Intrapulse Interference. 1. Control of Multiphoton Processes in Condensed Phases.
J. Phys. Chem. A **106**, 9369–9373 (2002).

[89] V. V. Lozovoy, I. Pastirk, and M. Dantus.
Multiphoton intrapulse interference. IV. Ultrashort laser pulse spectral phase characterization and compensation.
Opt. Lett. **29**, 775–777 (2004).

[90] B. Xu, J. M, Gunn, J. M. D. Cruz, V. V. Lozovoy, and M. Dantus.
Quantitative investigation of the multiphoton intrapulse interference phase scan method for simultaneous phase measurement and compensation of femtosecond laser pulses.
J. Opt. Soc. Am. B **23**, 750–759 (2006).

[91] V. V. Lozovoy, B. Xu, Y. Coello, and M. Dantus.
Direct measurement of spectral phase for ultrashort laser pulses.
Opt. Express **16**, 592–597 (2008).

[92] Y. Coello, V. V. Lozovoy, T. C. Gunaratne, B. Xu, I. Borukhovich, C. Tseng, T. Weinacht, and M. Dantus.
Interference without an interferometer: a different approach to measuring, compressing, and shaping ultrashort laser pulses.
J. Opt. Soc. Am. B **25**, A140–A150 (2008).

[93] A. Ludwig.
Pulsvermessung duch Pulsformung im Femtosekundenbereich: Experiment und Modellierung.
BSc Thesis, Universität Heidelberg (2014).
Supervised by KM.

[94] Y. Coello, B. Xu, T. L. Miller, V. V. Lozovoy, and M. Dantus.
Group-velocity dispersion measurements of water, seawater, and ocular components using multiphoton intrapulse interference phase scan.
Appl. Opt. **46**, 8394–8401 (2007).

[95] P. J. Wrzesinski, D. Pestov, V. V. Lozovoy, J. R. Gord, M. Dantus, and S. Roy.
Group-velocity-dispersion measurements of atmospheric and combustion-related gases using an ultrabroadband-laser source.
Opt. Express **19**, 5163–5171 (2011).

[96] J. Fraunhofer.
Bestimmung des Brechungs- und des Farbenzerstreungs-Vermögens verschiedener Glasarten, in Bezug auf die Vervollkommnung achromatischer Fernröhre.
Ann. Phys. **56**, 264–313 (1817).

[97] G. Kirchhoff and R. Bunsen.
Chemische Analyse durch Spectralbeobachtungen.
Annalen der Physik und Chemie **110**, 161–189 (1860).

[98] A. Kaldun.
Fano Resonances in the Time Domain - understanding and controlling the absorption and emission of light.
PhD Thesis, Universität Heidelberg (2014).

[99] *Datasheet of IR144*.
http://www.photonicsolutions.co.uk/datasheets/exci/IR-144.pdf (August 2014).
Photonic Solutions.

[100] U. Brackmann.
Lambdachrome Laser Dyes.
http://www.chem.ucla.edu/~craigim/pdfmanuals/catalogs/Lamdachrome-laser-dyes.pdf (August 2014).
Third Edition (January 2000). Lambda Physik AG, Germany.

[101] T. Joo, Y. Jia, J.-Y. Yu, M. J. Lang, and G. R. Fleming.
Third-order nonlinear time domain probes of solvation dynamics.
J. Chem. Phys. **104**, 6089–6108 (1996).

[102] Y. Nagasawa, J.-Y. Yu, and G. R. Fleming.
Solute–solvent interaction dynamics studied by photon echo spectroscopies in polymer glasses.
J. Chem. Phys. **109**, 6175–6183 (1998).

[103] J. D. Hybl, A. A. Ferro, and D. M. Jonas.
Two-dimensional Fourier transform electronic spectroscopy.
J. Chem. Phys. **115**, 6606–6622 (2001).

[104] H. Zhang, S. Zhang, C. Lu, T. Jia, Z. Wang, and Z. Sun.
Single-photon fluorescence enhancement in IR144 by phase-modulated femtosecond pulses.
Chem. Phys. Lett. **503**, 176–179 (2011).

[105] D. B. Turner, P. C. Arpin, S. D. McClure, D. J. Ulness, and G. D. Scholes.
Coherent multidimensional optical spectra measured using incoherent light.
Nat. Commun. **4**, 2298 (2013).

[106] N. Müller.
Nichtlinear-optische Spektroskopie mit kontrollierten und statistischen Phasen.
BSc Thesis, Universität Heidelberg (2014).
Supervised by KM.

[107] C. Cohen-Tannoudji, B. Diu, and F. Laloë.
Quantum Mechanics, volume II.
Wiley-Interscience (1977).

[108] T. Fließbach.
Quantenmechanik - Lehrbuch zur Theoretischen Physik III.
4. Auflage. Elsevier, Spektrum Akademischer Verlag (2005).

[109] T. Hashimoto, H. Nakano, and K. Hirao.
Theoretical study of the valence $\pi \rightarrow \pi^*$ excited states of polyacenes: Benzene and naphthalene.
J. Chem. Phys. **104**, 6244–6258 (1996).

[110] I. N. Levine.
Physical Chemistry.
Fourth Edition. McGraw-Hill, Inc. (1995).

[111] J. Mewes.
private communications.
Group of Prof. Dr. Andreas Dreuw, Interdisciplinary Center for Scientific Computing, Heidelberg University, Germany.

[112] E. B. Wilson, Jr., J. C. Decius, and P. C. Cross.
Molecular Vibrations: The Theory of Infrared and Raman Vibrational Spectra.
Dover Publications, Inc., New York (1980).

[113] G. Herzberg.
Molecular Spectra and Molecular Structure. II. Infrared and Raman Spectra of Polyatomic Molecules.
Krieger Publishing Company (1991).

[114] A. Kukol (Ed.).
Methods in Molecular Biology, vol. 443, Molecular Modeling of Proteins.
Humana Press (2008).

[115] E. A. Carson, W. M. Diffey, K. R. Shelly, S. Lampa-Pastirk, K. L. Dillman, J. S. Schleicher, and W. F. Beck.
Dynamic-Absorption Spectral Contours: Vibrational Phase-Dependent Resolution of Low-Frequency Coherent Wave-Packet Motion of IR144 on the Ground-State and Excited-State $\pi \rightarrow \pi^*$ Surfaces.
J. Phys. Chem. A **108**, 1489–1500 (2004).

[116] Y. H. Jiang, T. Pfeifer, A. Rudenko, O. Herrwerth, L. Foucar, M. Kurka, K. U. Kühnel, M. Lezius, M. F. Kling, X. Liu, K. Ueda, S. Düsterer, R. Treusch, C. D. Schröter, R. Moshammer, and J. Ullrich.
Temporal coherence effects in multiple ionization of N_2 via XUV pump-probe autocorrelation.
Phys. Rev. A **82**, 041403(R) (2010).

[117] T. Pfeifer, Y. H. Jiang, S. Düsterer, R. Moshammer, and J. Ullrich.
Partial-coherence method to model experimental free-electron laser pulse statistics.
Opt. Lett. **35**, 3441–3443 (2010).

[118] J. A. Fleck, Jr., J. R. Morris, and M. D. Feit.
Time-Dependent Propagation of High Energy Laser Beams through the Atmosphere.
Appl. Phys. **10**, 129–160 (1976).

[119] M. D. Feit, J. A. Fleck, Jr., and A. Steiger.
Solution of the Schrödinger Equation by a Spectral Method.
J. Comput. Phys. **47**, 412–433 (1982).

[120] T. Pfeifer, D. Walter, G. Gerber, M. Y. Emelin, M. Y. Ryabikin, M. D. Chernobrovtseva, and A. M. Sergeev.
Transient Enhancement of High-Harmonic Generation in Expanding Molecules.
Phys. Rev. A **70**, 013805 (2004).

[121] S. Chelkowski, P. B. Corkum, and A. D. Bandrauk.
Femtosecond Coulomb Explosion Imaging of Vibrational Wave Functions.
Phys. Rev. Lett. **82**, 3416–3419 (1999).

[122] P. Tzallas, E. Skantzakis, L. A. A. Nikolopoulos, G. D. Tsakiris, and D. Charalambidis.
Extreme-ultraviolet pump–probe studies of one-femtosecond-scale electron dynamics.
Nature Phys. **7**, 781–784 (2011).

[123] F. C. de Schryver, T. Vosch, M. Cotlet, M. van der Auweraer, K. Müllen, and J. Hofkens.
Energy Dissipation in Multichromophoric Single Dendrimers.
Acc. Chem. Res. **38**, 514–522 (2005).

[124] T. Buckup.
private communications.
"Akademischer Rat" in the group of Prof. Dr. Marcus Motzkus, Institute of Physical Chemistry, Heidelberg University, Germany.

[125] I. V. Schweigert and S. Mukamel.
Coherent Ultrafast Core-Hole Correlation Spectroscopy: X-Ray Analogues of Multidimensional NMR.
Phys. Rev. Lett. **99**, 163001 (2007).

[126] I. V. Schweigert and S. Mukamel.
Probing valence electronic wave-packet dynamics by all x-ray stimulated Raman spectroscopy: A simulation study.
Phys. Rev. A **76**, 012504 (2007).

[127] F. Remacle and R. D. Levine.
An electronic time scale in chemistry.
Proc. Nat. Acad. Sci. USA **103**, 6793–6798 (2006).

[128] L. Belshaw, F. Calegari, M. J. Duffy, A. Trabattoni, L. Poletto, M. Nisoli, and J. B. Greenwood.
Observation of Ultrafast Charge Migration in an Amino Acid.
J. Phys. Chem. Lett. **3**, 3751–3754 (2012).

[129] B. Mignolet, R. D. Levine, and F. Remacle.
Charge migration in the bifunctional PENNA cation induced and probed by ultrafast ionization: a dynamical study.
J. Phys. B: At. Mol. Opt. Phys. **47**, 124011 (2014).

[130] M. Dell'Angela, T. Anniyev, M. Beye, R. Coffee, A. Föhlisch, J. Gladh, T. Katayama, S. Kaya, O. Krupin, J. LaRue, A. Møgelhøj, D. Nordlund, J. K. Nørskov, H. Öberg, H. Ogasawara, H. Öström, L. G. M. Pettersson, W. F. Schlotter, J. A. Sellberg, F. Sorgenfrei, J. J. Turner, M. Wolf, W. Wurth, and A. Nilsson.
Real-Time Observation of Surface Bond Breaking with an X-ray Laser.
Science **339**, 1302–1305 (2013).

[131] S. M. Falke, C. A. Rozzi, D. Brida, M. Maiuri, M. Amato, E. Sommer, A. De Sio, A. Rubio, G. Cerullo, E. Molinari, and C. Lienau.
Coherent ultrafast charge transfer in an organic photovoltaic blend.
Science **344**, 1001–1005 (2014).

[132] *NIST Standard Reference Database*.
http://physics.nist.gov/cuu/Constants/ (August 2014).

Danksagung

Zum Schluss möchte ich all denen, die mich während der letzten Jahre begleiteten und unterstützten, Danke sagen.

Zuerst gilt mein besonderer Dank Thomas Pfeifer. Ich danke dir für die Aufnahme in deine Arbeitsgruppe und dass du mir die Arbeit mit diesem spannenden Thema ermöglicht hast. Du hast dir für Diskussionen, Fragen und Probleme immer Zeit genommen. Während meiner Promotion habe ich durch all deine Ideen, hilfreichen Hinweise und Erklärungen viel gelernt. Vielen Dank auch für deine erstklassige Betreuung und das Vertrauen, das du mir entgegen gebracht hast!

Auch möchte ich mich bei Professor Andreas Wolf bedanken, der sich als Gutachter für meine Doktorarbeit zur Verfügung gestellt hat.

Mein besonderer Dank geht an alle "Interattos" bzw. "X-Musicians" für die wunderbare Zeit. Die Zusammenarbeit mit euch bereitete sehr viel Spaß. Neben den vielen physikalischen Diskussionen gab es immer auch etwas zu lachen. Christian Ott, Andreas Kaldun, Philipp Raith, Martin Laux, Thomas Ding, Alexander Blättermann, Yonghao Mi und Veit Stooß möchte ich für die zahlreichen, hilfreichen Gespräche, Tipps, die Unterstützung im Labor, das Korrekturlesen dieser Arbeit und vieles mehr danken. Auch möchte ich mich bei Zuoye Liu, der mir unermüdlich im Labor zur Seite gestanden und bei den Experimenten immer geholfen hat, aus ganzem Herzen bedanken. Ohne ihn wäre diese Arbeit nicht zu Stande gekommen.

Ich danke meinen drei Bachelorstudenten Rima Schüssler, Andreas Ludwig und Niklas Müller, die ich während meiner Promotion betreuen durfte. Ihr alle habt mich sehr unterstützt und mit euren Arbeiten zum Gelingen dieser Dissertation beigetragen. Es hat viel Spaß gemacht, mit euch zusammen zu arbeiten!

Ebenso möchte ich allen ehemaligen und neuen Gruppenmitgliedern, die zur tollen Arbeitsatmosphäre in unserer Gruppe beigetragen haben, Danke sagen.

Vielen Dank an die gesamte Abteilung Pfeifer (ehemals Ullrich) für eine schöne Zeit, nicht nur während der Arbeit, sondern auch in der Freizeit mit verschiedensten Aktivitäten.

Mein Dank geht ebenfalls an Jan Mewes aus der Arbeitsgruppe von Professor Dreuw, IWR Heidelberg, der die Berechnungen für das Farbstoffmolekül durchführte und sich für die Beantwortung aller meiner Fragen viel Zeit nahm.

Außerdem möchte ich mich bei Bernd Knape für die technische Untersützung im Labor bedanken.

Ich danke der Zentralen Feinwerkmechanik unter der Leitung von Herrn Spranz, die alle benötigten Komponenten für die experimentellen Aufbauten angefertigten. Besonders danken möchte ich an dieser Stelle Uwe Zeiske, der kurzfristige und dringende Dinge immer sofort übernahm.
Der Elektronikwerkstatt danke ich für die schnelle Hilfe und Erledigung verschiedenster Aufträge.
Vielen Dank an die Netzwerkgruppe, unter anderem mit Kevin Zink und Stefanie Kolb, die bei Software- und Hardwareproblemen immer zur Stelle waren. Allen ein herzliches Dankeschön!

Ganz besonders möchte ich mich bei meinen Freunden und meiner Familie bedanken für die Geduld und das Verständnis, das sie mir entgegen brachten, wenn ich wieder einmal völlig gestresst war und für nichts Zeit hatte. Auch danke ich aus ganzem Herzen meinen Eltern, die immer in allen Lebenslagen für mich da waren, mir halfen und mich auf vielerlei Art und Weise unterstützten. Ohne sie hätte ich all dies nicht erreicht.

Ich möchte allen, die ich namentlich nun nicht erwähnt habe, die aber zum Gelingen dieser Arbeit beigetragen haben - in welcher Art auch immer -, sagen: DANKE!